# Combined Application of Density Functional Theory and Molecular Mechanics Sampling Techniques to study Chemical Systems, from Intramolecular Rearrangements to Polymerization Reactions

A THESIS SUBMITTED TO THE FACULTY OF UNIVERSITY OF MINNESOTA
BY

**Sina Chiniforoush**

**IN PARTIAL FULFILLMENT OF THE REQUIREMENTS FOR THE DEGREE OF DOCTOR OF PHILOSOPHY**

**Christopher J. Cramer (advisor), Sapna Sarupria (Co-advisor)**

**May 2023**

# Acknowledgements

I would first like to thank my advisors, professors Chirstopher J. Cramer and Sapna Sarupria. I'd like to thank Prof. Cramer for providing an amazing environment that allowed me to explore my interests, and being supportive of me and my work throughout my graduate studies, and supporting my difficult times. Prof. Cramer's feedback allowed me to be a better communicator of my research. I'd like to thank Prof. Sarupria for her support in the later years of my studies, and allowing me to have an opportunity to expand my research experience, as well as providing me with much-needed advice on how I can organize my time better as a researcher.

Two of the chapters included in this thesis are from collaborations with experimental groups. I'd like to thank Prof. William B. Tolman for insightful feedback throughout our collaborations. I would also like to thank Dr. Anna Luke and Dr. Yanay Popowski for their feedback and encouragement. I'd also like to thank Dr. Amani Lee and Prof. Pomerantz and Prof. Haynes for their support and feedback.

I would also like to thank Dr. Mukunda Mandal, for his guidance and mentorship.

I would also like to thank Porhouy Minh and Varun Gopal, for their support inside and outside the lab.

I would also like to thank all other members of the Cramer, Gagliardi, and SAMPEL groups, past and present, for their support, including Dr. Aaron B. League, Dr. Büşra Dereli, Dr. Manuel A. Ortuño, Dr. Ravithree Senanayake, Dr. Saied Md Pratik, Dr. Jingyun Ye, and Dr. Riddhish Pandhakar from the Cramer group, Dr. Jenny G. Vitillo, Dr. Hung Pham, Dr. Carlo Alberto Gaggioli, Dr. Prachi Sharma, Dr. Debmalya Ray, And Dr. Matthew Hermes from the Gagliardi group, and Steven Hall, Dr. Neetu Singh Yadav, Dr. Ernesto Cortes-Morales, Steven Hall, Jonathan Zajac, Youchi Zhang, Praveen Muralikrishnan, and Naomi Tramp.

I would also like to thank Katelyn Youmans, whose support, understanding and compassion helped me through the most difficult times of my PhD years.

I would also like to thank all the friends I've made outside the academic environment, whose support I value greatly, including Jacob, Richie, Kassidy, Courtney, Willow, Molly, Ansel, Eva, and many others. And I'd like to thank my partner, Dalton, for being a great source of support, love, and encouragement.

And lastly, I owe an immense debt of gratitude towards my family, especially my mother, without whose support I would not be here, nor would I be who I am.

# Dedication

This thesis is dedicated to all women of Iran.

May you find victory in your struggle for freedom.

# Abstract

Modern techniques in computational chemistry have allowed for the investigation of a diverse array of problems in chemistry and material sciences. However, one of the main challenges in the use of these techniques is the trade-off between computational cost and chemical accuracy. Methods like density-functional theory (DFT) are often accurate, but at the expense of higher computational resources. Methods like molecular mechanics (MM) are less computationally expensive, but fail to describe important features of chemical systems.

While the study of chemical systems of relatively small size can often be carried out using methods like DFT, some of these systems have a high number of conformational degrees of freedom despite their relatively small size, and it's often not possible to accurately describe important characteristics of these systems without capturing these all possible conformers. In this case, using MM-based sampling methods followed by DFT computations can allow for a relatively accurate description of these systems.

This work contains three studies. In chapter 2, the mechanistic details of Newman-Kwart rearrangement under oxidative conditions is explored using DFT, and using theoretical predictions, modifications to the Newman-Kwart substrate are proposed to increase reactivity. In chapter 3, a combination of MM sampling methods and DFT are used to evaluate the temperature sensitivity of $^{19}F$ chemical shifts in a library of organofluorine compounds screened for temperature sensing, and computations were used to successfully predict the chemical shift temperature sensitivity of these compounds, and finally used to guide the synthesis of more temperature sensitive compounds. In chapter 4, the same combination of DFT and MM techniques were used to describe two Aluminum-based ring-opening transesterification polymerization (ROTEP) catalysts, and a variety of the features of these catalysts, including the origin of their stereoselectivity, the mechanism of the inversion of catalyst chirality, and the relative stereoselectivity of the catalysts in the initiation stage, and the mechanism of stereoselectivity in the propagation stage, were described.

# Preface

Parts of this thesis are adapted from previously published work by me and other co-authors.

Chapter 2 is reproduced from the work published in reference 26 with permission from the American Chemical Society.

Chapter 3 is reproduced from the work published in reference 27 with permission from the American Chemical Society. Experimental details included in this chapter derive from the work of co-authors.

Chapter 4 is in part reproduced from the work published in reference 28 with permission from the American Chemical Society. Edits are made in order to make this chapter more cohesive, as it also includes previously unpublished work related to the work in reference 28. Experimental details included in this chapter also derive from the work of co-authors.

# Table of Content

# List of Tables

# List of Figures

center nitrogen (positions α and β). The p-value is < 0.0001 for significant terms. Greek characters indicate the assignment of the fluorine group.

**Figure 3.2.** Temperature response of decafluorobiphenyl and comparison to perfluorotributylamine (PFTBA). (A) $^{19}F$ NMR spectra of decafluorobiphenyl as temperature increases. The assignments for fluorine groups are colored to match their assignment on the spectrum; a (blue) = 2,2′,6,6′-F, b (red) = 3,3′,5,5′-F, c (black) = 4,4′-F. (B) Computational and (C) experimental comparison of thermal response ($\Delta\Delta\delta(T)$) between decafluorobiphenyl and perfluorotributylamine. The graph compares the quantified response of PFTBA vs decafluorobiphenyl based on the most and least responsive fluorine group pairs.

**Figure 3.3.** Computational screening method of functional groups to develop novel fluorinated sensors. (A) Theoretical response of two different fluorine resonances ($\Delta\delta_a$ and $\Delta\delta_b$) as a function of temperature in a linear model. At a given temperature, the difference between $\Delta\delta_a$ and $\Delta\delta_b$ is equal to the $\Delta\Delta\delta$. (B) Theoretical graph of how $\Delta\Delta\delta(T)$ is based on the absolute difference between the slopes of the two functional groups ($\Delta\delta_a$ and $\Delta\delta_b$) as a function of temperature ($\Delta\Delta\delta(T) = m_d$). (C) Scale and boundary of experimental fluorine group responsiveness. The ideal case is to identify two functional groups in the more common regions of responsiveness (e.g., $\pm 7 \times 10^{-3}$ ppm $°C^{-1}$) with opposing directions in response to temperature. The absolute magnitude of difference between those two responsive groups is the overall responsiveness of the temperature probe and should be ≥ 1.5 times the PRF signal. The values under each molecule are from experimental measurements. Color coded numbers are different functional groups on the same molecule. Each fluorine group on PFTBA (right side) has an individual response from 18 to 27 × $10^{-3}$ ppm $°C^{-1}$.

**Figure 3.4.** Structure and temperature response of **6**. (A) Synthesis and structure of **6**. (B) $^{19}F$ NMR spectrum of **6** in $CDCl_3$. Assignments were derived from analogous structures in literature. (C) $^{19}F$ spectra of most temperature responsive chemical shifts (ppm). (D) Temperature response curve of **6** with $\Delta\Delta\delta(T) = 19.5 \times 10^{-3} \pm 0.2 \times 10^{-3}$ ppm $°C^{-1}$ (n = 3, mean ± SEM). Compound **6** has a ~ 2-fold increase in responsiveness compared to the PRF. (E) Movement of individual resonances over 20 °C; several of the shifts are in the

optimal region (± 5 to ± 10 × $10^{-3}$ ppm °$C^{-1}$) indicating most of the resonance combinations are above 10 × $10^{-3}$ ppm °C. The most responsive combinations are indicated as green triangles (down for negative movement, and up for positive movement). Error bars are negligible from 3 replicate measurements.

**Figure 4.9.** Representations of the X-ray crystal structures of the ring-opened products (a) $L^2$Al(oLAOBn) and (b) $L^7$Al(oLAOBn), resulting from the reactions of $L^2$AlOBn and $L^7$AlOBn, respectively, with 1 equiv of *rac*-LA. Only a single enantiomer for each structure is shown (Δ-L(*S*,*S*); the other Λ-D(*R*,*R*) enantiomer is also present in the unit cell), with all atoms presented as 50% ellipsoids and hydrogen atoms omitted for clarity. Selected bond distances (Å) and angles (deg): (a) Al1–O1, 1.804(2); Al1–N1, 1.932(3); Al1–N2, 2.058(5); Al1–N3, 2.054(1); Al1–N4, 1.945(0); N3–Al1–N1, 160.070(6); N3–Al1–O1, 99.876(5); N3–Al1–O2, 88.536(1); N3–Al1–N2, 79.984(0); N3–Al1–N4, 80.830(1); N2–Al1–N4, 100.140(0); O2–Al1–O1, 81.204(6); N2–Al1–O2, 84.416(7); N4–Al1–O1, 94.002(8); N4–Al1–O2, 167.451(7); N1–Al1–N4, 102.280(5), N1–Al1–N2, 80.091(8); N1–Al1–O2, 89.986(1); N1–Al1–O1, 99.531(4); (b) Al1–O1, 1.807(3); Al1–N1, 1.9475(18); Al1–N2, 2.0647(16); Al1–N3, 2.0779(18); Al1–N4, 1.9344(17); N3–Al–N1, 171.24(7); N3–Al1–O1, 90.80(8); N3–Al1–O2, 89.33(13); N3–Al1–N2, 82.69(6); N3–Al1–N4, 89.49(7); N2–Al1–N4, 103.71(7); O2–Al1–O1, 79.47(11); N2–Al1–O2, 81.07(9); N4–Al1–O1, 95.56(9); N4–Al1–O2, 174.88(12); N1–Al1–N4, 94.99(7); N1–Al1–N2, 88.93(7); N1–Al1–O2, 86.84(14); N1–Al1–O1, 96.24(9).

**Figure 4.10.** Illustration of possible interconversions of stereoisomers $L^7$Al(oLAOBn). The red arrows indicate processes involving intermolecular exchange of LA enantiomers, blue arrows correspond to racemization at Al (e.g., via carbonyl decoordination, isomerization, and recoordination), and black arrows correspond to both.

**Figure 4.11.** Illustration of the calculated initiation pathway for a selected catalyst (Δ-$L^7$AlOMe), substrate (D(*R*,*R*)-LA), and approach trajectory.

**Figure 4.12.** TS2 structures for all pathways with the Δ-$L^7$AlOMe catalyst. The structural analogy independent of lactide along the si vs the re pathways is highlighted by circling the methoxy groups.

**Figure 4.13.** Structures of TS2 along si face reaction pathways for the Δ-$L^7$AlOMe (top) and Δ-$L^2$AlOMe (bottom) catalysts

**Figure 4.14.** The N(1)-Al-O(1) and N(2)-Al-O(1) angles shown for TS2 (L-si pathway) in the $L^7$AlOMe catalyst as an example.

# Chapter 1

**Synopsis**

This chapter covers the fundamental concepts behind the computational methods employed to study the systems investigated in this thesis, which includes density functional theory (DFT) and molecular mechanics (MM), followed by a brief overview of how these methods were employed in these studies.

## 1.1. Computational Chemistry and its applications

One of the main goals of chemical research is predicting the outcomes of chemical reactions and processes, and properties of materials. These predictions can then be used to guide the design of processes used to produce products and materials with applications in various fields. Such accurate predictions of the properties of materials and compounds, as well as the processes they undergo often requires a detailed understanding of these systems at an atomistic level.

Various experimental methods are employed in the characterization of chemicals and materials. There's a rich history of chemists deducing chemical structures through a combination of chemical tests and the separation and characterization of the products of these reactions by measuring the bulk properties of these products, such as Kekulé's deduction of the chemical structure of benzene. Modern characterization techniques such as X-ray crystallography, mass-spectrometry and the wide array of spectroscopic techniques are of based on a detailed understanding of the interactions between the particles in molecular compounds and materials and their internal structure, and in turn, they give direct insight into these structures, as well as the processes they go through. Through the separation of reactive intermediates and real-time use of these characterization techniques, it's also possible to gain insight into reactive events and kinetics.

While these methods are indispensable for the study and design of chemical processes and materials, they can often be costly both in terms of time and resources, making the exploration of different possibilities challenging. This is especially relevant to applications like catalysis or drug design, where there can be a large range of variations in reaction conditions, and the structures of catalysts and substrates. Moreover, the constraints of the experimental setup might limit the study to simpler model systems or conditions that might not be representative of the more complex systems they are supposed to represent, and despite the advancements in the development of these

techniques, certain atomistic details of reactive events cannot be investigated by these methods. This includes events that occur at timescales that fall outside the scope of experimental measurements, and detailed characterization of features such as molecular geometry, which is often only possible in limited cases, such as X-ray crystallography or Scanning-Tunneling microscopy, which are mostly used in solid-state systems.

Computational chemistry has the potential to address these problems in a fast and inexpensive manner. Certain experimental limitations that hinder the ability of researchers to explore the space of different chemical structures and conditions do not exist in computations, and systems can be studies at timescales and states that are often not possible in experiments. While computational methods have their own constraints and limitations, and can be costly in their own right, by combining experimental and computational methods, it's possible to tackle problems using multiple approaches.

The following sections include a brief overview of computational methods, with a focus on methods used in this work, and an overview of how these methods were employed in various systems of interest to study different problems.

## 1.2 Overview of Computational Methods

There are a variety of computational methods used to study different systems. The choice of methods is often a trade-off between accuracy and computational cost, and is largely determined by the size of the system, as computations on systems of larger size are more costly.

*Molecular mechanics* (MM) methods are based on an approximate classical parametrization of the inter-atomic interactions of a molecular system as a function of its relevant coordinates, such as bond lengths, bond angles and dihedral angles. Since classical mechanics cannot coherently describe the interactions between the particles molecules are composed of, the dependency of the energy on the coordinates is parametrized such that it reproduces either experimental measurements of interest, or the results of more accurate ab-initio computations. Since the computational cost of MM methods scales very favorably with the system size, they are often useful for the

description of larger systems[1]. MM methods are used to investigate problems such as protein folding, solvent-solute interactions, and to deduce bulk thermodynamic properties of various systems of interest. Note that none of these examples include chemical reactions. Because MM force fields are based on classical mechanics, they cannot describe the formation and breaking of chemical bonds accurately, and their utility is for the most part limited to the description of non-bonded interactions, although efforts do exist to use MM to describe reactive systems [2,3], though effort exist to construct MM methods that can model chemical reactions. For Similar reasons, MM methods cannot describe excited state systems. The reliance of MM methods on parametrization also means that their utility can often be limited to the systems used to construct the force fields.[4]

In order to surpass this limitation, ab-initio quantum-mechanical (QM) theories can be employed to treat such problems and describe systems. One of the foundational QM methods is the Hartree-Fock (HF) method, which approximates the solution to the Schrodinger equation for molecular systems by averaging the inter-electronic repulsions. While immensely useful, HF method cannot capture many-body interactions and the correlated motion of electrons, making its utility limited.

To address this problem, so called post-HF and wave function (WF) theories were developed. These methods use the HF solution as a starting point and systematically improve upon it using the principles of QM[5]. These methods, however, are exceptionally costly except for the smallest systems. The computational cost scales factorially with respect to the number of electrons in the system in the case of methods like full configuration interaction (FCI) [6]. While the application of these systems is limited to the smallest systems, they are still useful, not only for the study of these systems, but also the development of other less costly computational methods, both for as a way of evaluating their performance, and use their results to optimize the parameters used in the construction of these methods.

Nevertheless, there's still a need for methods that can treat chemical systems of interest without a significant cost. Density Functional Theory (DFT) methods can deliver on this

promise. [6,7], DFT computations have been used to treat a wide variety of systems, and DFT methods are the most popular QM methods used in computational chemistry today [8,9]. It's noteworthy, however, that DFT methods still suffer from some problems, especially in their treatment of highly correlated and multi-reference systems[10]. Despite its limitations, the favorable computational cost of DFT methods compared to the existing alternatives makes them attractive for studying chemical systems.

### 1.2.1 Overview of the Principles Quantum Mechanics

The mathematical treatment of physical systems in quantum mechanics can be described by the Dirac-von Neumann axioms of the mathematical formulation of quantum mechanics, explained as follows[11].

1. The state of any given system in quantum mechanics is described by a vector $|\Psi\rangle$ in a Hilbert space.
2. The observables are described by operators acting on these vectors. For any given observable $A$ operator $\hat{A}$, the expectation value is computed by the inner product $\langle\Psi|\hat{A}|\Psi\rangle$

For most chemical applications, we are interested in systems in stationary state, which are eigenvectors of the Hamiltonian operator. As such, the eigenvector and its corresponding eigenvalue (the energy of the system) can be found using the eigenvalue equation 1.1 (known as the Schrodinger equation[12]), where T and V are the kinetic energy and potential energy operators, and $\Psi$ is the eigenvector of the Hamiltonian operator, $\hat{H}$. All equations in this chapter are written in atomic units.

$$\hat{H}|\Psi\rangle = \left(\hat{T} + \hat{V}\right)|\Psi\rangle = E|\Psi\rangle \tag{1.1}$$

If the eigenvector $|\Psi\rangle$ is expanded in terms of the eigenvectors of the position operator $|\boldsymbol{x}\rangle, |\boldsymbol{x}'\rangle$, the Schrodinger equation can be expanded as shown in equations 1.2, where $\delta(\boldsymbol{x}' - \boldsymbol{x})$ is the Kronecker delta function.

$$\int \hat{H}|\boldsymbol{x}'\rangle\langle\boldsymbol{x}'|\Psi\rangle d\boldsymbol{r}' = E\int |\boldsymbol{x}'\rangle\langle\boldsymbol{x}'|\Psi\rangle d\boldsymbol{x}' \tag{1.2.1}$$

$$\int \langle \boldsymbol{x}|\hat{H}|\boldsymbol{x}'\rangle\langle \boldsymbol{x}'|\Psi\rangle d\boldsymbol{x}' = E\int \langle \boldsymbol{x}|\boldsymbol{x}'\rangle\langle \boldsymbol{x}'|\Psi\rangle d\boldsymbol{x}' \tag{1.2.2}$$

$$\int \langle \boldsymbol{x}|\hat{H}|\boldsymbol{x}'\rangle\langle \boldsymbol{x}'|\Psi\rangle d\boldsymbol{x}' = E\int \delta(\boldsymbol{x}'-\boldsymbol{x})\langle \boldsymbol{x}'|\Psi\rangle d\boldsymbol{x}' = E\langle \boldsymbol{x}|\Psi\rangle \tag{1.2.3}$$

All the terms in equation terms in equation 1.2.3 are all scalar values that are functions of the positions, $\boldsymbol{x}$. The product $\langle \boldsymbol{x}|\Psi\rangle$ is often denoted by $\Psi(\boldsymbol{x})$, and called the *wavefunction*, and the integral on the left-hand side is a functional operation on $\Psi(\boldsymbol{x})$. In quantum chemistry, the Schrodinger equation is typically expressed in terms of the wavefunction (see equation 1.3), as the specific dependence of the wavefunction on the coordinates of the particles a system is composed of is very useful.

$$\hat{H}\Psi(\boldsymbol{x}) = E\,\Psi(\boldsymbol{x}) \tag{1.3}$$

### 1.2.2 Hartree-Fock Method

The systems of interest in chemistry are composed of electrons and positively charged atomic nuclei. Ignoring the internal structures of the nuclei, the Hamiltonian operator for such systems is as described in equation 1.2. Where $\nabla^2$ is the Laplacian operator for kinetic energy, and the sums A and B are over all of nuclei, whereas i and j are sums over all electrons, Z terms represent the nuclear charges, and r values represent the distances between particles.

$$\hat{H} = -\frac{1}{2}\sum_A \nabla_A^2 + \frac{1}{2}\sum_{A,B}\frac{Z_B Z_A}{r_{AB}} - \sum_{A,i}\frac{Z_A}{r_{Ai}} - \frac{1}{2}\sum_i \nabla_i^2 + \frac{1}{2}\sum_{i,j}\frac{1}{r_{ij}} \tag{1.4}$$

In most molecular systems and under most conditions, the motion of the electrons and nuclei are decoupled from one another, in part due to the large difference in the masses of the mass of the electrons and the nuclei, so the nuclei can be assumed to be stationary with respect to the electrons. This is known as the adiabatic or Born-Oppenheimer approximation[13]. This means that we can write separate eigenvalue equations for the electronic and nuclear part of the Hamiltonian, and the wavefunction is can be expressed as a product of nuclear and electronic wavefunctions. The electronic Hamiltonian is shown in equation 1.5.

$$\hat{H}_{el} = -\frac{1}{2}\sum_{i}\left(\nabla_i^2 - \sum_{A}\frac{Z_A}{r_{Ai}} + \frac{1}{2}\sum_{j}\frac{1}{r_{ij}}\right) \tag{1.5}$$

Equation 1.5 is an example of a many-body problem, and it cannot be solved analytically for the overwhelming majority of chemical systems if there are more than two particles. Moreover, unlike in the case of Nuclei, the motion of different electrons cannot be decoupled. Moreover, Pauli's exclusion principle[14] dictates that the wavefunction must be antisymmetric with respect to the exchange of electrons, as shown in equation 1.6, and as such it cannot be described as a product of one-electron wavefunctions.

$$\Psi(\boldsymbol{x_1}, \boldsymbol{x_2}, \dots, \boldsymbol{x_i}, \dots, \boldsymbol{x_j}, \dots, \boldsymbol{x_N}) = -\Psi(\boldsymbol{x_1}, \boldsymbol{x_2}, \dots, \boldsymbol{x_j}, \dots, \boldsymbol{x_i}, \dots, \boldsymbol{x_N}) \tag{1.6}$$

It is possible, however, to construct a wavefunction as a linear combination of one-particle wavefunctions such that it obeys the Pauli's exclusion principle. Such a linear combination is called the Slater determinant[15], described by equation 1.7, where $\phi_i(x_j)$ terms correspond to 1-electron wavefunction i which is a function of the coordinates of electron j, and the $|\boldsymbol{\alpha}\rangle$ and $|\boldsymbol{\beta}\rangle$ terms are the spin component of the wavefunction. The 1-electron wavefunctions $\phi_i$ are typically chosen to be orthonormal with one another.

$$\langle \mathbf{x}|\Phi_{\mathrm{SD}}\rangle = \Phi_{\mathrm{SD}}(\mathbf{x}) = \frac{1}{\sqrt{N!}}\begin{vmatrix} \phi_1(\boldsymbol{x_1})|\boldsymbol{\alpha}\rangle & \phi_1(\boldsymbol{x_1})|\boldsymbol{\beta}\rangle & \phi_2(\boldsymbol{x_1})|\boldsymbol{\alpha}\rangle & \dots & \phi_N(\boldsymbol{x_1})|\boldsymbol{\beta}\rangle \\ \phi_1(\boldsymbol{x_2})|\boldsymbol{\alpha}\rangle & \phi_1(\boldsymbol{x_2})|\boldsymbol{\beta}\rangle & \phi_2(\boldsymbol{x_2})|\boldsymbol{\alpha}\rangle & \dots & \phi_N(\boldsymbol{x_2})|\boldsymbol{\beta}\rangle \\ \vdots & \vdots & \vdots & \ddots & \vdots \\ \phi_1(\boldsymbol{x_N})|\boldsymbol{\alpha}\rangle & \phi_1(\boldsymbol{x_N})|\boldsymbol{\beta}\rangle & \phi_2(\boldsymbol{x_N})|\boldsymbol{\beta}\rangle & \dots & \phi_N(\boldsymbol{x_N})|\boldsymbol{\beta}\rangle \end{vmatrix} \tag{1.7}$$

While the wavefunction cannot be found exactly for most molecular systems, it's still possible to capture a significant proportion of the repulsive interaction between the electrons by assuming each electron interacts with a static charge distribution produced by other electrons. With this approximation, it's possible to describe the wavefunction as a slater determinant of one-electron wavefunctions. This approximation is known as the *Hartree-Fock (HF)* theory[5].

Note that this *physical description*, (which is independent electrons interacting with the electrostatic field generated by the charge distribution of other electrons) and the *mathematical description* (the wavefunction taking the form of a Slater determinant), can be shown to be equivalent, because computing the expectation value of the Hamiltonian (equation 1.8) in a system whose wavefunction takes the form of a Slater determinant yields an expression for the energy that describes such a system.

$$\langle \Phi_{\mathrm{SD}} | \hat{H}_{el} | \Phi_{\mathrm{SD}} \rangle = -\frac{1}{2}\sum_{i}\left( \langle \Phi_{\mathrm{SD}} | \nabla_i^2 | \Phi_{\mathrm{SD}} \rangle - \sum_{A} \left\langle \Phi_{\mathrm{SD}} \left| \frac{Z_A}{r_{Ai}} \right| \Phi_{\mathrm{SD}} \right\rangle + \frac{1}{2}\sum_{j>i} \left\langle \Phi_{\mathrm{SD}} \left| \frac{1}{r_{ij}} \right| \Phi_{\mathrm{SD}} \right\rangle \right) \quad (1.8)$$

Replacing the term $|\Phi_{\mathrm{SD}}\rangle$ in equation 1.8 by the slater determinant described in equation 1.7, and exploiting the orthonormality of the 1-electron wavefunctions, the expectation value of the Hamiltonian Operator can be found in terms of the one-electron wavefunctions as shown in equation 1.9, where $\hat{h}_i$ represents 1-electron operators, and $\hat{\mathrm{P}}_{12}$ is the exchange operator, swapping $\boldsymbol{x_1}$ and $\boldsymbol{x_2}$.

$$\langle \Phi_{\mathrm{SD}} | \hat{H}_{el} | \Phi_{\mathrm{SD}} \rangle = -\frac{1}{2}\sum_{i} \langle \Phi_{\mathrm{SD}} | \hat{h}_i | \Phi_{\mathrm{SD}} \rangle + \frac{1}{2}\sum_{i}\sum_{j>i} \left\langle \Phi_{\mathrm{SD}} \left| \frac{1}{r_{ij}} \right| \Phi_{\mathrm{SD}} \right\rangle$$

$$\langle \Phi_{\mathrm{SD}} | \hat{H}_{el} | \Phi_{\mathrm{SD}} \rangle = -\frac{1}{2}\sum_{i} \langle \Phi_{\mathrm{SD}} | \hat{h}_i | \Phi_{\mathrm{SD}} \rangle + \frac{1}{2}\sum_{i}\sum_{j>i} \int \phi_i(\boldsymbol{x_1})\phi_j(\boldsymbol{x_2}) \frac{1}{r_{12}} (1 - \hat{\mathcal{P}}_{12}) \phi_i{}^*(\boldsymbol{x_1})\phi_j{}^*(\boldsymbol{x_2}) d\boldsymbol{x_1} d\boldsymbol{x_2} \quad (1.9)$$

The 2-electron integral terms are often separated into two terms, the Coulomb (equation 1.10) and Exchange (equation 1.11) integrals.

$$J_{ij} = \int \phi_i(\boldsymbol{x_1})\phi_j(\boldsymbol{x_2}) \frac{1}{r_{12}} \phi_i{}^*(\boldsymbol{x_1})\phi_j{}^*(\boldsymbol{x_2}) d\boldsymbol{x_1} d\boldsymbol{x_2} \quad (1.10)$$

$$K_{ij} = \int \phi_i(\boldsymbol{x_1})\phi_j(\boldsymbol{x_2}) \frac{1}{r_{12}} \phi_i{}^*(\boldsymbol{x_2})\phi_j{}^*(\boldsymbol{x_1}) d\boldsymbol{x_1} d\boldsymbol{x_2} \quad (1.11)$$

Note that this expectation value for the energy does not represent the Hartree-Fock energy of the system, because we have not assumed anything about the 1-electron

wavefunctions other than them being orthonormal. Since the charge distribution is itself a function of the 1-electron wavefunctions, one needs to find a set of 1-electron wavefunctions $\phi_i$ that produces an electrostatic potential that, upon solving the eigenvalue equations, would yield the 1-electron wavefunctions themselves, i.e. a *self-consistent field* (SCF). In the next section, an algorithm for arriving at the self-consistent field is described.

### 1.2.3 Self-consistent Field Method

According to the Variational principle in quantum mechanics, the expectation value of the Hamiltonian operator for a wavefunction other than the eigenfunction of the Hamiltonian is always higher than the eigenvalue of the Hamiltonian. Thus, by finding the expectation value of the Hamiltonian operator for a set of trial wavefunctions with variable parameters, and then finding the minimum value of the expectation value with respect to those parameters, it's possible to find an approximate value for the energy of the system, and approximate wavefunctions describing the system. Minimizing the expectation value for the Hamiltonian operator yields the Eigenvalue equation 1.12, known as the Fock equation, where $\hat{f}$ is known as the Fock operator.

$$\hat{f}|\phi_i\rangle = \epsilon_i|\phi_i\rangle$$

$$\hat{f} = -\frac{1}{2}\nabla^2 - \sum_A \frac{Z_A}{|\boldsymbol{r} - \boldsymbol{r_A}|} + \sum_j \int d\boldsymbol{x_2}\phi_i^*(\boldsymbol{x_2})\frac{1}{r_{12}}(1 - \hat{\mathcal{P}}_{12})\phi_j(\boldsymbol{x_2}) \qquad (1.12)$$

It's possible to express the 1-electron wavefunctions as a linear combination of a known set of wavefunctions $\psi_j$, also known as the basis functions, as shown in equation 1.13.

$$\phi_i = \sum_j C_{ij}\psi_j \qquad (1.13)$$

Substituting the wavefunctions $\phi_i$ in equation 1.12 in terms of the basis functions $\psi_j$ yields equation 1.14.

$$\hat{f}|\phi_i\rangle = \epsilon_i|\phi_i\rangle$$

$$\sum_k C_{ik}\,\hat{f}|\psi_k\rangle = \epsilon_i \sum_k C_{ik}\,|\psi_k\rangle$$

$$\sum_k C_{ik}\,\langle\psi_m|\hat{f}|\psi_k\rangle = \epsilon_i \sum_k C_{ik}\,\langle\psi_m|\psi_k\rangle \tag{1.14}$$

Equation 1.14 is often written in its matrix form, where the inner products $\langle\psi_m|\hat{f}|\psi_k\rangle$ and $\langle\psi_m|\psi_k\rangle$ are written as matrix elements $F_{mk}$ and $S_{mk}$ respectively, referred to as the Fock Matrix, and the coefficients $C_{ik}$ are the elements of the coefficient matrix. Equation 1.15 shows this abbreviated matrix form.

$$\boldsymbol{FC = SC\epsilon} \tag{1.15}$$

In the SCF method, one starts with an initial coefficient matrix C. The Fock matrix F is a function of the coefficient matrix, because the Fock operator depends on the 1-electron wavefunctions $\phi_i$ (see equation 1.12) and by extension the coefficient matrix (equation 1.13), and it can be constructed for a given coefficient matrix. The eigenvalue equation 1.15 can then be solved, and a new coefficient matrix is found, which can be used to construct a new Fock matrix. This process is repeated until the desired conversion criteria (for the total energy or the coefficient matrix) is met.

### 1.2.4 Density Functional Theory

The HF method assumes that the electrons only interact with a field of static charge density produced by other electrons and the nuclei. This approximation, while useful, neglects to account for the correlated motion of the electrons. There are a variety of post-HF methods that seek to improve upon the wavefunction, often using the HF approach as the starting point. However, wavefunction-based methods are often prohibitively expensive for all except the smallest systems of interest.

Density Functional Theory (DFT) is an alternative approach which attempts to maintain the computational simplicity of the SCF approach. This can be achieved by shifting the focus from the wavefunction to the *electron density*, $\rho(\boldsymbol{r})$. The fundamental idea behind DFT is that the electron density in a system under the influence of an external potential is uniquely determined by that field (In this context, an "external potential" is used to refer

to the potential generated by anything *external to the electrons* that the system is composed of. The phrase "external potential" is often used to refer to the field that is generated by the environment external to the entire system of interest, including nuclei, and that's not what's being referred to here). Conversely, for systems with a non-degenerate ground state, the potential can be constructed uniquely using the electron density. This means that there is a one-to-one relationship between the electron density and the external potential, and thus the Hamiltonian, and by extension, the energy. Since density is itself a function of the spatial coordinates, the energy is said to be a *functional* of density (i.e., function of a function), hence the name *Density Functional Theory* (DFT).

In 1964, Hohenberg and Kohn developed the Hohenberg-Kohn theorems[16]. The first theorem proved the aforementioned relationship between the electron density and the external potential. The second theorem states that (assuming the exact form of the functional is known), the electron density that yields the lowest value of energy is the ground state electron density, and conversely, if an electron density yields the lowest value of energy, it is the true ground state electron density.

A general expression for the energy functional, expressed in terms the kinetic energy as well as the electrostatic energy caused by the interaction of electrons with one another and the external field (caused by the nuclei) can be found in equation 1.16, where $V_{ne}$ is the nuclear-electronic electrostatic potential energy, $V_{ee}$ is the interelectronic potential energy, and $T$ is the kinetic energy.

$$E[\rho(r)] = V_{ne}[\rho(r)] + V_{ee}[\rho(r)] + T[\rho(r)] \tag{1.16}$$

The value of the nuclear-electronic potential energy is as described in equation 1.17, where the $\boldsymbol{A}$ indices refer to the nuclei.

The electrostatic repulsion of a charge distribution in classical mechanics is as shown in equation 1.18.

$$V_{ne}[\rho(r)] = -\sum_{A} \int \frac{\rho(\boldsymbol{r})d\boldsymbol{r}}{|\boldsymbol{R_A} - \boldsymbol{r}|} \tag{1.17}$$

However, this expression contains a self-interaction error, which is apparent if this integral is evaluated for a one-electron system. Moreover, this expression also doesn't account for the exchange energy (found in HF theory by the exchange integral, see equation 1.10). Therefore, the inter-electronic repulsion term is often expressed as shown in equation 1.18, where $V_{xc}[\rho(r)]$ is called the *exchange-correlation functional*, and contains a correction on the classical interelectronic repulsion potential energy.

$$V_{ee}[\rho(r)] = \frac{1}{2}\int \frac{\rho(\boldsymbol{r}')\rho(\boldsymbol{r})d\boldsymbol{r}d\boldsymbol{r}'}{|\boldsymbol{r}-\boldsymbol{r}'|} + V_{xc}[\rho(r)] \tag{1.18}$$

The exact form of the exchange-correlation functional, as well as the kinetic energy term, are unknown. Nevertheless, these insights still allowed for the construction of accurate computational methods with only a fraction of the cost of wavefunction-based methods.

### 1.2.5 Kohn-Sham SCF Method

Another step in the advancement of DFT came with the development of Kohn-Sham (KH) theory[7]. One of the major advantages of HF theory is that describing the electrons as independent allows for the development of the SCF methodology. Kohn-Sham theory further develops DFT by expressing the energy using a *fictitious system of non-interacting electrons* as a starting point. This allows for the construction of the density using the one-electron wavefunctions of the non-interacting electrons, and allows for the computation of the kinetic by applying the kinetic energy operator on these one-electron wavefunctions, as shown in equation 1.19, where $T_{ni}$ is the kinetic energy for the non-interacting system, and $\chi_i$ are the wavefunctions of the electron in that system.

$$T_{ni}[\rho(r)] = -\frac{1}{2}\sum_i \langle\chi_i|\nabla^2|\chi_i\rangle \tag{1.19}$$

Equation 1.18 can then be re-written in terms of this non-interacting system, as shown in equation 1.20, where $V_{ee}^c[\rho(r)]$ is the classical inter-electronic repulsion term, and the terms $\Delta V_{ee}[\rho(r)]$ and $\Delta T[\rho(r)]$ capture the correction to the repulsion and kinetic energy terms, respectively.

$$E[\rho(r)] = T_{ni}[\rho(r)] + V_{ne}[\rho(r)] + V_{ee}^c[\rho(r)] + \Delta V_{ee}[\rho(r)] + \Delta T[\rho(r)]$$

$$E[\rho(r)] = T_{ni}[\rho(r)] + V_{ne}[\rho(r)] + V_{ee}^{c}[\rho(r)] + V_{xc}[\rho(r)] \tag{1.20}$$

As seen in equation 1.20, the kinetic energy and potential energy correction terms are usually condensed into one term, which is written as $V_{xc}[\rho(r)]$. Note that this new decomposition of the electronic energy functional means that this expression for the exchange-correlation functional is different from the one found in equation 1.17, as it also contains the correction to the kinetic energy.

As written, all of the terms in equation 1.20, except for $V_{xc}$, can be expressed in terms of the wavefunctions of the electrons in the non-interacting system, $\chi_i$. By constructing a one-electron exchange-correlation potential $v_{xc}$, such that the sum of the expectation values for this potential add up to the total exchange-correlation energy as shown in equation 1.21, all terms can be expressed in terms of the one-electron wavefunctions.

$$\begin{aligned} V_{xc}[\rho(r)] &= \sum_i \langle \chi_i | v_{xc} | \chi_i \rangle \\ E[\rho(r)] == &-\frac{1}{2}\sum_i \langle \chi_i | \nabla^2 | \chi_i \rangle - \left\langle \chi_i \middle| \textstyle\sum_A \frac{Z_A}{|\boldsymbol{R_A} - \boldsymbol{r}|} \middle| \chi_i \right\rangle \\ &+ \frac{1}{2}\int \left\langle \chi_i \middle| \frac{\rho(\boldsymbol{r}')d\boldsymbol{r}'}{|\boldsymbol{r} - \boldsymbol{r}'|} \middle| \chi_i \right\rangle + \langle \chi_i | v_{xc} | \chi_i \rangle \end{aligned} \tag{1.21}$$

It's thus possible to construct one-electron Fock operators, analogous to equation 1.12. This is called the Kohn-Sham one-electron operator, shown in equation 1.22.

$$\hat{h}_i^{ks} = -\frac{\nabla^2}{2} - \sum_A \frac{Z_A}{|\boldsymbol{R_A} - \boldsymbol{r}|} + \frac{1}{2}\int \frac{\rho(\boldsymbol{r}')d\boldsymbol{r}'}{|\boldsymbol{r} - \boldsymbol{r}'|} + v_{xc} \tag{1.22}$$

The density itself can also be found from the one-electron wavefunctions, as shown in equation 1.23.

$$\rho(r) = \sum_i \langle \chi_i | \chi_i \rangle \tag{1.23}$$

Given this construction, one can develop an SCF method, and find the energy and density for the system.

### 1.2.6 Exchange-Correlation Functionals

So far, we are no closer to developing a practical method to compute the electron density, energy, or other properties of a system using DFT. Because the form of the exact exchange-correlation potential is not known, Kohn-Sham theory, on its own, cannot provide a way for us to solve for the electron density and energy of a system. Moreover, unlike in the case of wavefunction methods, there is no systematic way to improve upon any approximate functional. In the absence of such a systematic method, there are several different approaches for arriving at an approximate form for $V_{xc}$, depending on what kind of problem the specific DFT formulation aims to solve. Typically, exchange-correlation functionals are constructed with many parameters that can be optimized for these specific goals. The exchange and correlation functionals are also often constructed separately.[6,17]

One approach (common in solid state physics) is to design the exchange-correlation potential such that it behaves correctly in certain physical conditions, as certain limiting behaviors of the exact functional are known.[17–19] Another approach is to optimize the exchange-correlation functional such that it reproduces certain results, either experimental measurements, or the value of the exchange or correlation energy derived from more costly wavefunction-based quantum-mechanical computations. These approaches are of course not mutually exclusive, and there are other important factors that are often taken into consideration.

While there's no systematic way to improve upon density functionals, it's possible to discuss the existing functionals in terms of their increasing complexity through the inclusion of additional terms in the functional form, to account for more of the semi-local and non-local contributions to the exchange-correlation energy. This is typically described through a DFT "Jacob's ladder"[18], as shown in figure 1.1.

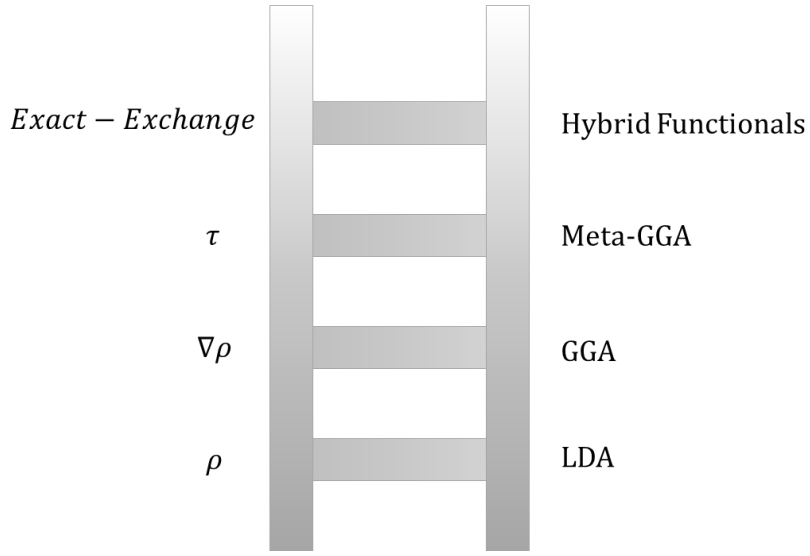


**Figure 1.1.** The DFT "Jacob's Ladder".[18] The classes of functionals are listed on the right. The terms included in the functionals are included on the left. (Figure adapted from reference 18)

It's also important to note that for spin-polarized systems, the explicit inclusion of the electron densities for electrons of different spins, $\rho_\alpha(\boldsymbol{r})$ and $\rho_\beta(\boldsymbol{r})$ (collectively referred to as $\rho_\sigma(\boldsymbol{r})$) and the spin density, as defined in equation 1.24.

$$\zeta(\boldsymbol{r}) = \frac{\rho_\alpha(\boldsymbol{r}) - \rho_\beta(\boldsymbol{r})}{\rho(\boldsymbol{r})} \tag{1.24}$$

In functionals constructed based on the *Local Density Approximation* (LDA), the exchange-correlation *energy density* in each location depends only on the value of the electron density in that location, as shown in equation 1.25, where $f\big(\rho(\boldsymbol{r})\big)$ represents the local exchange-correlation energy density.

$$V_{xc}[\rho(r)] = \int f\big(\rho_\sigma(\boldsymbol{r})\big)d\boldsymbol{r} \tag{1.25}$$

The expression for the LDA exchange-correlation energy was derived for a "uniform electron gas", and it works reasonably well for solid state systems where such a uniformity assumption works. For spin-polarized systems, the spin density is included explicitly, and thus the LDA is modified to include the spin density, also known as local spin density approximation (LSDA).[17]

Due to its local nature, however, the LDA approach fails in highly correlated systems with long-range or non-local electron correlation effects, or where the density is non-uniform, such as molecular systems.

To address this limitation, Generalized-Gradient Approximation (GGA) functionals[20] include terms that are a function of the gradient of the electron density as well as the density itself. Equation 1.26 shows the general form of such functionals.

$$V_{xc}[\rho(r)] = \int f\left(\rho_\sigma(\boldsymbol{r}), \nabla\rho_\sigma(\boldsymbol{r})\right)d\boldsymbol{r} \tag{1.26}$$

The next natural step is to improve upon include higher-order derivatives of the electron density, such as the Laplacian, in the exchange-correlation energy density. However, the kinetic energy density term in Kohn-Sham theory satisfies more physical constraints on the exchange-correlation functionals. Meta-GGA functionals employ kinetic energy density, tau, in the exchange-correlation energy density, as shown in equation 1.27

$$V_{xc}[\rho(r)] = \int f(\rho_\sigma(\boldsymbol{r}), \nabla\rho_\sigma(\boldsymbol{r}), \tau_\sigma)d\boldsymbol{r} \tag{1.27}$$

While the functionals presented so far account for local and near-local interactions, certain components of the exchange-correlation functional, specifically the exchange functional, necessarily need to have a long-range or non-local component to adequately describe molecular systems. In the HF method, the exchange energy is computed exactly using the exchange operator.

Suppose through a fictitious (non-physical) process, a system of non-interacting electrons is adiabatically varied through the continuous introduction of the inter-electronic interactions.

The Hellmann-Feynman theorem[21,22] states that for a quantum system where the Hamiltonian is a function of a parameter, the derivative of the energy with respect to the parameter is found via equation 1.28, where $\lambda$ is the parameter, and psi is the an eigenfunction of the Hamiltonian.

$$\frac{dE}{d\lambda} = \left\langle \psi^{\lambda} \middle| \frac{d\hat{H}(\lambda)}{d\lambda} \middle| \psi^{\lambda} \right\rangle \tag{1.28}$$

If we construct the Hamiltonian as a function of the parameter $\lambda$ such that at $\lambda = 0$, the Hamiltonian describes the non-interacting system and at $\lambda = 1$ it describes the real system (or a correlated DFT approximation), equation can be rewritten as shown in equation 1.29.

$$\int_{E_x^{HF}}^{E_{xc}} dE = \int_0^1 \left\langle \psi^{\lambda} \middle| \frac{d\hat{H}(\lambda)}{d\lambda} \middle| \psi^{\lambda} \right\rangle d\lambda$$

$$E_{xc} = E_x^{HF} + \int_0^1 \left\langle \psi^{\lambda} \middle| \frac{d\hat{H}(\lambda)}{d\lambda} \middle| \psi^{\lambda} \right\rangle d\lambda \tag{1.29}$$

Due to the way the Hamiltonian is constructed, the lower bound for the value of the integral term in equation is zero, and the upper bound is $E_{xc} - E_x^{HF}$. As such, one can express the value of the exchange-correlation functional as shown in equation 1.30

$$E_{xc} = E_x^{HF} + a(E_x^{DFT} - E_x^{HF}) \tag{1.30}$$

Variations of equation are used in what's known as the hybrid DFT functionals, with varying degrees of incorporation of the HF exchange energy.[6,17]

### 1.3. Conformational Sampling Methods

One of the main challenges in studying larger molecular systems is the large space of conformations resulting from the many conformational degrees of freedom in such systems. These degrees of freedom introduce complications in describing these systems, as finding the global minimum structure on the potential energy surface (PES) is less trivial with the presence of many low-lying configurations. Moreover, conformers that are not the global minimum still contribute to the kinetics and thermodynamics of chemical systems, as well as their bulk properties.

While DFT computations are relatively fast and accurate, they are not well-suited for exploring the potential energy surface, as they are still too computationally costly. As such, it's often useful to combine DFT computations with more inexpensive, albeit less

accurate, computational methods for these larger systems. For this purpose, MM methods in combination with sampling methods can be used to acquire a set of reasonable starting structures for DFT optimizations.

*The Monte Carlo Molecular Mechanics* (MCMM) method employs a combination of molecular mechanics calculations and Monte Carlo simulation techniques to generate a set of low-energy conformers for systems of interest.[23]

In Monte-Carlo (MC) sampling, the coordinates are varied in each step, and the moves in each step are accepted (i.e., the conformer is stored as a new conformer) if their energy is lower than the conformer in the previous step. Crucially, however, if the energy is higher, it's not necessarily rejected, instead, the rejection probability is computed according to the metropolis criterion, shown in equation 1.31.

$$P = \min\left(1, \exp\left(-\frac{(E_2 - E_2)}{k_B T}\right)\right) \tag{1.31}$$

This means that there's a chance that the new step is accepted with a Boltzmann-weighed probability. This allows the algorithm to explore higher energy conformations and avoid getting trapped in local energy minima.

*Low-mode* (LM) conformational sampling[24] is another methods used to sample the conformations on the PES. LM methods utilize the fact that the low-mode vibrational modes of a molecule are often responsible for the interconversion between the conformers close in energy to the local minimum. By perturbing the system along these coordinates until a saddle point is reached, and following the gradient to the other side of the saddle point, these conformers can be found.

These two sampling methods explore different areas of the PES. The MC sampling allows for the exploration of regions of the PES outside the local minimum, whereas LM methods can be used to explore the region around the local minimum. Together, these two methods can be combined to gain an even distribution of conformers across the PES.[25]

## 1.4. An Overview of this Thesis

The following chapters, three studies will be introduced wherein the methods described in this chapter, and a combination of them, were utilized to gain insight into a wide range of chemical systems.

The first chapter[26] explores a study of the Newman-Kwarts rearrangement under oxidative conditions. DFT computations were used to gain insight into the mechanism of the rearrangement both in the oxidized and neutral state, as well as the electronic structure of the intermediates and the transition states. The results of the DFT computations agrees with the experiments, and described the trends in the reactivity of various O-Aryl thiocarbamate substrates under these different conditions, as well as the exceptions to these trends. Using the understanding of the reaction mechanism, modifications of the thiocarbamate group were proposed that would increase the reactivity of the substrates, and computations on these modified substrates confirmed the effectiveness of the modifications.

The second chapter[27] includes a joint experimental-computational study with the Pomerantz group wherein the temperature dependency of the F-NMR chemical shift values of different Fluorine atoms in various organofluorine compounds are investigated, to probe their potential application for in-vivo temperature measurements. Since the change in the chemical shifts of the Fluorine atoms in these compounds as a function of temperature is a direct result of the shift in the distribution of the conformers, MCMM conformer searches were carried out on all of the compounds, and the conformers found through the MCMM searches were then used as initial structures for DFT optimization, to find the chemical shift values. While this method didn't always predict the *direction* of the experimental chemical shift change as a function of temperature, in part due to the limitations of the sampling, by evaluating the Boltzmann-weighed dispersion of the values of the chemical shifts, it was possible to make qualitative predictions of the order of the *magnitude* of the temperature sensitivity for each compound. Similar computations for a list of candidate compounds to assess their temperature sensitivity, and the compound analogous to the one predicted to be most sensitive was synthesized, and was

shown to have a temperature sensitivity higher than any of the compounds investigated prior to this study.

The final chapter[28] focuses on two related studies. The first study, conducted in collaboration with the Tolman group, is an investigation into the initiation mechanism of the ring-opening transesterification polymerization (ROTEP) of *rac*-Lactide by two Aluminum-Indolide catalysts, and the origin of their stereoselectivity. DFT computations were utilized to find the activation free energy for the various ring-opening reactive pathways of both L and D-Lactide. Theory correctly predicted the relative reactivity of these catalysts based on the enantioselectivity of the initiation mechanism. Other features of these catalysts, such as the origin of their fluxionality and the mechanism of their chirality inversion were also studied.

The second study is a continuation of the first study, with the focus shifted from initiation to the propagation mechanism. Due to the larger size and higher flexibility of the system, the same combination of MCMM conformational sampling and DFT optimizations as in the F-NMR study were utilized. After an exhaustive search of all mechanistic pathways, it was found that the rate determining step in the propagation reaction was different from the initiation mechanism, and the direction of the enantioselectivity was found to be reversed for the propagation.

# Chapter 2

**Synopsis**

Details of the electronic and geometric structures of stationary points along the reaction coordinate of the Newman Kwart rearrangement, which transforms an *O*-arylthiocarbamate into an *S*-arylcarbamothioate, are examined using quantum-chemical methods for a large number of compounds considering both the thermal reactions of uncharged substrates as well as the corresponding reactions of radical-cation substrates generated under photoredox conditions. The uncharged mechanism, which has intrinsically high 298 K free energies of activation (in excess of 30 kcal $mol^{-1}$), has the character of nucleophilic aromatic substitution and is thus accelerated by electron-withdrawing substituents on the aromatic ring. The radical-cationic mechanism, by contrast, has 298 K free energies of activation that are typically below 20 kcal $mol^{-1}$ and is accelerated by electron *donating* substituents on the aromatic ring, which stabilize the hole character that is transferred to this fragment from the thiocarbamate fragment as the reaction proceeds. Opportunities to further accelerate the radical-cation reaction are revealed by computational assessment of alternative amino groups for the thiocarbamate functionality.

## 2.1 Introduction

Aromatic mercaptans comprise a class of organosulfur compounds relevant to the pharmaceutical, agrochemical, and other industries.[29–33] Of the synthetic pathways that generate aromatic mercaptans,[34–38] one of the most robust and widely used is the Newman−Kwart rearrangement (NKR),[38] which transforms aryloxy functionality to arylsulfido through the rearrangement of an intermediate thiocarbamate, as shown in Figure 1 for the case of Ar = Ph. The NKR can thus be thought of as an intramolecular nucleophilic aromatic substitution occurring at the ipso carbon with the product being an *S*-aryl carbamothioate.

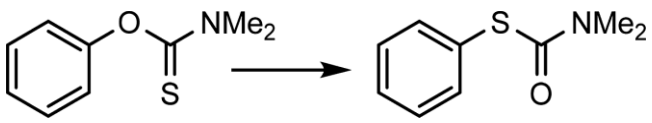


**Figure 2.1.** Newman−Kwart rearrangement.

In addition to aromatic systems, benzylic[39] and allylic[40] examples of the NKR have also been reported, and theoretical studies suggest that the scope of this rearrangement should extend to other conjugated systems, too.[41] The analogous rearrangement with selenium in place of sulfur has also been observed.[42]

Under typical reaction conditions, the NKR is run at temperatures ranging from 200 to 300 °C. Such high temperatures limit the utility of the reaction with substrates having other sensitive functionality or prone to other thermal rearrangements or racemization. Palladium catalysis has been shown in certain instances to reduce required temperatures to about 100 °C.[38] Pursuing alternative approaches, in 2015, Perkowski et al.[43] reported

using photoredox catalysis to accomplish the reaction under mild conditions, and in 2018, Pedersen et al. reported similar success with ceric ammonium nitrate (CAN) as a sacrificial oxidant.[44] Interestingly, these conditions foster rearrangements of some substrates not observed to react (productively) under thermal NKR conditions. Perkowski et al.[43] proposed that both photoredox and radical chain reaction mechanisms could be operative (Figure 2.2).[45] With respect to the radical chain mechanism, Pedersen et al.[44] observed 14% conversion of *O*-*p*- methoxyphenyl-*N*,*N*-dimethylthiocarbamate in the presence of 0.1 equiv of CAN under an $N_2$ atmosphere after 24 h at room temperature but attributed the excess conversion to possible leakage of oxygen into the reaction vessel, suggesting that if a radical-chain process proceeds, it is at best slow.

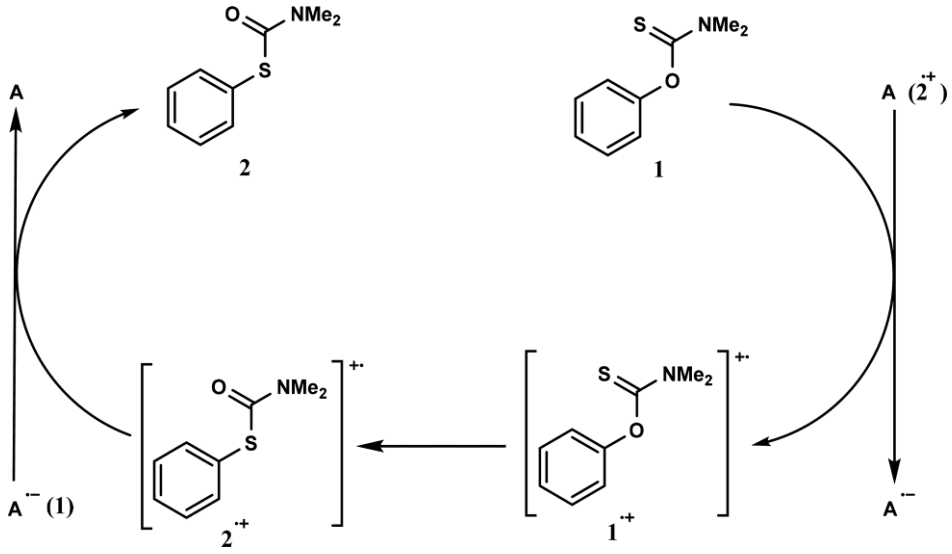


**Figure 2.2.** Proposed mechanism(s) for radical-cation Newman−Kwart rearrangement. Initial oxidation of thiocarbamate 1 by an oxidizing agent A (which may be any oxidant, including intermediate $2^{\bullet+}$) leads to radical cation thiocarbamate $1^{\bullet+}$, which rearranges to radical cation $2^{\bullet+}$. Intermediate $2^{\bullet+}$ may oxidize $A^{\bullet-}$ (which in the case of a radical chain mechanism would be thiocarbamate 1), thereby generating product carbamothioate 2.

To better understand factors affecting the mechanism of the NKR under photoredox conditions, we here report quantum- chemical calculations for a wide range of substrates including most of those reported by Perkowski et al. and Pedersen et al. Through analysis of trends as a function of aromatic substitution, we elucidate relationships between relative redox potentials of NKR reactants and products and free energies of activation for rearrangement of radical-cation intermediates. We moreover predict that modification of the amine component of the thiocarbamate group to make it less electron-donating should accelerate the NKR under these conditions and, thereby, further extend the scope of the reaction to otherwise less reactive substrates.

## 2.2 Computational Methods

The geometries of all stationary points were optimized at the density functional level of theory employing the M06-2X functional[46] and the 6-31+G(d) basis set (for those compounds having multiple conformational possibilities, care was taken to identify the lowest energy educt and TS-structure geometries).[47] Harmonic vibrational frequencies were computed to confirm the nature of optimized structures and to enable the computation of 298 K molecular partition functions following the conventional ideal-gas, rigid-rotator, harmonic-oscillator approximation,[6] except that all frequencies below 50 $cm^{-1}$ were replaced by values of 50 $cm^{-1}$ for this latter purpose (the quasi-harmonic oscillator approximation[48]). Thermochemical quantities (enthalpy, entropy, and Gibbs free energy) were obtained by summing partition-function contributions with single-point energies computed at the M06-2X level with the def2-TZVP basis set.[49,50] For all optimizations, frequency calculations, and single-point energy calculations, acetonitrile solvation effects were included using the SMD[51] continuum model for that solvent. Charge distributions were assessed through the computation of CM5 partial atomic charges[52] and Hirshfeld spin densities.[53]

The choice of the M06-2X model was motivated in part by its extensively benchmarked good performance for main-group thermo- chemistry.[54–57] Moreover, our interest in this work is primarily to explore and understand variations in reactivity associated with

substitution of paradigmatic substrates, so identification of the "best" functional with respect to prediction of absolute free energies of reaction or activation is of limited importance for our purposes. Nevertheless, to better assess the likely accuracy of our computed absolute energies, for selected compounds we undertook complete- basis-set-extrapolated calculations at the DLPNO/CCSD(T) level of theory,[58,59] as described more fully in the Supporting Information. The electronic structure software suites Gaussian 09[60] and ORCA[58] were employed for all calculations.

### 2.3 Results and Discussion

As there is no reason to imagine electron transfer to be the rate-limiting step in the radical-cation NKR reaction, we are primarily interested in the rearrangement step itself as well as the relative oxidation potentials of substrate and product as a function of substitution and aromatic ring. In each instance, the relevant four species are reactant thiocarbamate 1, intermediate thiocarbamate radical cation $1^{\bullet+}$, intermediate carbamothioate radical cation $2^{\bullet+}$, and product carbamothioate 2, as shown in Figure 2.2 for the specific case of converting phenol to thiophenol via the intermediate functionalized species. For 38 distinct cases, including most of the substrates studied by Perkowski et al.[43] and Pedersen et al., [44]as well as a few others chosen for specific reasons discussed further below, the geometries of these 4 key species (1, $1^{\bullet+}$, 2, and $2^{\bullet+}$) were optimized, and their geometries, electronic structures, and free energies were analyzed to identify trends relevant to reactivity. In order to understand how reactions of the radical cations differ from those of their uncharged analogues, we computed transition-state (TS) structures on both the neutral and one-electron-oxidized potential energy surfaces. The complete list of substrates is included in the Supporting Information, but we will focus primarily on trends rather than the precise reactivity of any given substrate below.

#### 2.3.1 Energetics

With a large data set to consider, the relative efficiency of density functional theory (DFT) makes it the most convenient quantum-chemical model to use. As noted in the Computational Methods, extensive benchmarking of the M06-2X functional has

suggested that it should be a robust choice for a study of organic structure and reactivity like that undertaken here, particularly as we are primarily interested in trends across substrates as opposed to absolute reactivities. Nevertheless, to provide some estimate of the quantitative accuracy of the M06-2X model, we first compared it to complete-basis-set-extrapolated calculations at the DLPNO− CCSD(T) level of theory for the gas-phase rearrangements of substrates derived from phenol, *p*-chlorophenol, and *p*- methoxyphenol (Table 2.1). In addition, Pedersen et al.[44] have provided G4MP2 data for these three compounds (for geometries optimized at the B3LYP/6-31G(2df,p) level), and these are included for comparison as well.

**Table 2.1.** Computed Gas-Phase Electronic Energies (kcal $mol^{-1}$) of Reaction ($\Delta E_R$) and Activation ($\Delta E^{\ddagger}$) for the Newman− Kwart Rearrangement of Selected Uncharged and Oxidized *p*-Substituted Thiophenols at the M06-2X, G4MP2, and DPLNO− CCSD(T) Levels of Theory [a]

| | | | DLPNO−CCSD(T)[b] | | | | |
|---|---|---|---|---|---|---|---|
| | *p*-substituent | | def2-SVP | def2-TZVP | CBS | G4MP2[c] | M06-2X/def2-TZVP[d] |
| −$OCH_3$ | uncharged | $\Delta E_R$ | −11.4 | −12.0 | −12.2 | −12.5 | −10.6 (−9.5) |
| | | $\Delta E^{\ddagger}$ | 49.2 | 47.7 | 43.8 | 42.1 | 46.0 (46.9) |
| | oxidized | $\Delta E_R$ | −6.0 | −8.0 | −8.4 | −14.4 | −7.4 (−9.3) |
| | | $\Delta E^{\ddagger}$ | 12.9 | 10.0 | 9.4 | 8.8 | 12.9 (13.3) |
| −H | uncharged | $\Delta E_R$ | −10.4 | −11.0 | −11.2 | −11.1 | −9.4 (−8.2) |
| | | $\Delta E^{\ddagger}$ | 47.6 | 45.5 | 41.7 | 39.9 | 43.7 (43.8) |
| | oxidized | $\Delta E_R$ | 4.5 | 1.6 | −0.9 | 1.6 | 0.5 (−2.0) |
| | | $\Delta E^{\ddagger}$ | 19.4 | 15.6 | 13.0 | 13.5 | 16.6 (17.8) |
| −Cl | uncharged | $\Delta E_R$ | −10.8 | −11.4 | −11.6 | −12.2 | −9.9 (−8.5) |
| | | $\Delta E^{\ddagger}$ | 47.2 | 45.1 | 41.5 | 38.8 | 43.4 (42.9) |
| | oxidized | $\Delta E_R$ | 2.0 | −0.7 | −3.4 | −4.1 | −2.5 (−2.7) |
| | | $\Delta E^{\ddagger}$ | 16.7 | 13.1 | 10.3 | 12.8 | 13.4 (16.7) |

[a]All geometries optimized at the M06-2X level of theory unless otherwise indicated. [b]Reported for SVP and TZVP basis sets and extrapolated to the CBS limit (bold type). [c]B3LYP/6-31G(2df,p) geometries; data from reference 11b. [d]Energies in parentheses add solvation free energies in MeCN to gas-phase values.

Comparing the extrapolated CBS DLPNO−CCSD(T) values to M06-2X, we find that M06-2X predicts energies of reaction and activation that are in every case more positive (or, equivalently, less negative) than those computed at the CBS DLPNO-CCSD(T) level, with the average difference over the 12 values being about 2.1 kcal $mol^{-1}$. The G4MP2 values show variations of similar magnitude compared to CBS DLPNO− CCSD(T), albeit without any systematic trend in those variations (mean unsigned deviation of 1.7 kcal $mol^{-1}$). While there is no a priori guarantee that the wave function levels of theory are more accurate than the density functional level, overall we interpret this trend to suggest that M06-2X systematically underestimates the stability of an aryl C−S bond relative to an aryl C−O bond, or of a C=O bond relative to a C=S bond, or both. However, as this is a systematic error, there is much better agreement between levels when assessing the perturbing effects of substituents, and for comparing the relative energetics of neutral vs oxidized reactions, and we thus proceed with M06-2X to continue our analysis over the full data set. We also note that when comparing MeCN to the gas phase, the effect of solvation on the Newman−Kwart reaction, whether for a neutral or radical cation, is found to be quite small (values in last two columns of Table 2.1). We continue including solvation effects (and thermal contributions to total free energies) for the sake of completeness, but note that all of our interpretations below are fundamentally related to simple variations in electronic structure, uncomplicated by solvation or thermal contributions.

Activation free energies ($\Delta G^{\ddagger}$) computed for the uncharged reactant set were in the range of 35−50 kcal $mol^{-1}$. Such relatively high values are consistent with the high temperatures required for the rearrangement of these substrates and agree with selected values reported in previous computational studies.[41] Interestingly, we did not observe a particularly strong Bell−Evans−Polanyi linear free energy relationship between the free

energies of activation and the free energies of reaction ($\Delta G_R$) for the neutral substrates ($R^2$ = 0.02, see Supporting Information), suggesting that substituents do not similarly perturb the electronic structure of the TS structure and the product when compared to the reactant.

Considering the set of one-electron-oxidized reactants, computed $\Delta G^{\ddagger}$ values were much lower, ranging from roughly 11 to 21 kcal·mol$^{-1}$, consistent with the much lower reaction temperatures reported by Perkowski et al.[43] and Pedersen et al.[44] under photocatalytic and sacrificial oxidant conditions, respectively. In this instance, a strong Bell−Evans−Polanyi linear free energy relationship *was* observed when comparing $\Delta G^{\ddagger}$ to $\Delta G_R$ (Figure 2.3), a point which will be discussed in more detail below.

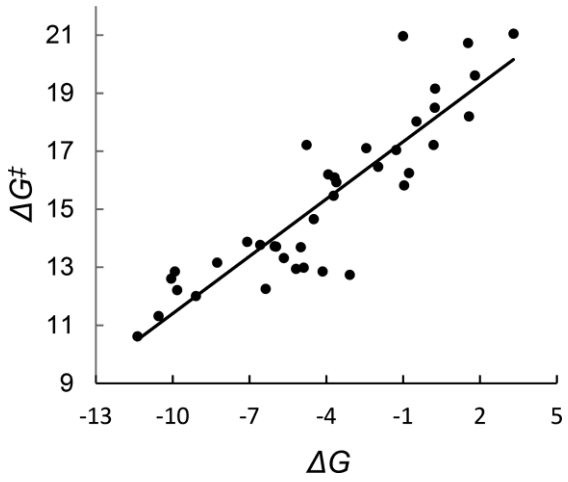


**Figure 2.3.** Activation vs reaction free energy (kcal·mol$^{-1}$) for Newman−Kwart rearrangement of radical-cation substrates. The best fit line is shown and has $R^2$ = 0.790.

Another linear free energy relationship that emerges relates $\Delta G_R$ for the radical-cation NKR to the free energy of electron transfer for the reaction 2 + 1 → 1 + 2. As shown in

Figure 2.4, it is apparent that stabilization of carbamothioate product $2^{\bullet+}$ relative to thiocarbamate reactant $1^{\bullet+}$, which implies a more exergonic radical-cation NKR, also makes $2^{\bullet+}$ a relatively poor oxidant, so that in the limit of the most exergonic radical-cation reactions, the propagation of a radical-chain pathway by direct electron transfer becomes endergonic, albeit by less than 2 kcal $mol^{-1}$ in the most extreme cases.

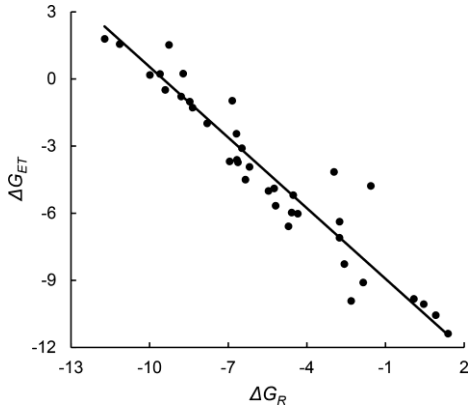


**Figure 2.4.** Radical cation reaction vs electron transfer free energy (kcal $mol^{-1}$). The best fit line is shown and has $R^2 = 0.905$.

Of course, the reaction may be engineered to proceed under conditions where the nature of the oxidant obviates any need for a chain mechanism. Geometric Variations. Upon oxidation of the substrates, the geometries of the radical cations $1^{\bullet+}$ change such that key bonds have lengths closer to those in the NKR TS structure than is the case for neutral antecedents 1. Thus, the C(1)−O and C(2)=S bond lengths increase (see Figure 2.5 for atom numbering), while the C(2)−N and C(2)−O bond lengths, and the C(1)−S interatomic distance, all decrease (see Figure 2.6 for the specific case of *p*-methoxy-substituted substrate).

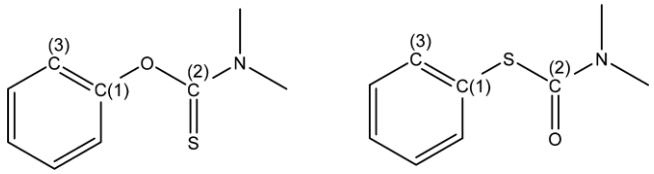


**Figure 2.5.** Carbon atom numbering scheme for 1 and $1^{\bullet+}$ (left) and 2 and $2^{\bullet+}$ (right).

For the bond lengths involving C(2), the changes are consistent with expectations for what is formally a six-electron, oxazathiatrimethylenemethane functional group, with the highest energy orbital of that group being dominated by C=S $\pi$ character. Loss of the electron decreases the C=S bond order, while the C−N and C−O bond orders increase through Figure 2.7). That same resonance somewhat decreases the bond order of the phenolic C(1)−O bond, while the observed approach of S to the ipso C(1) is driven simply from favorable electrostatic interactions of the positively charged thiocarbamate group to the aromatic $\pi$ cloud.

When comparing $2^{+\bullet}$ to 2, by contrast, the C(1)−S bond length shrinks while that for C(2)−S increases. The C(2)−N bond length also shortens, reflecting the special stability of the $[(CH_3)_2N{=}C{=}O]^+$ cation, which has been previously noted by Prabhakar and co-workers[61] from mass spectrometric studies of NKR reactions under electron-impact ionization conditions in the gas phase.

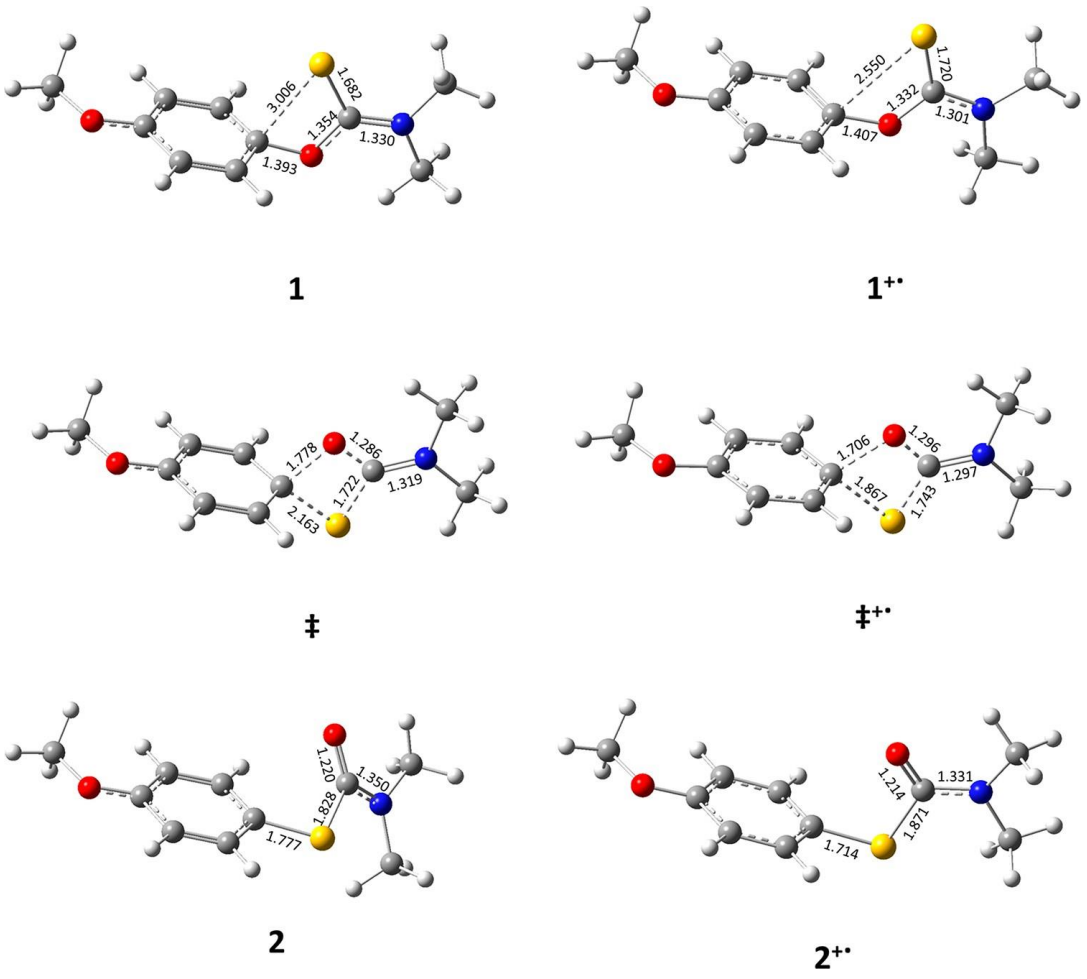


**Figure 2.6.** Optimized geometries for stationary points along the uncharged (left) and oxidized (right) NKR rearrangement reaction coordinates of *O*-*p*-methoxyphenyl-*N*,*N*-dimethylthiocarbamate, proceeding from reactant (top), through TS structure (middle), to product (bottom). Key bond distances are indicated (Å).

Electrostatic effects also have a large influence on the TS structures, with the forming and breaking bonds to the *ipso* carbon of the aromatic ring substantially shorter in the radical-cation case than the uncharged case (Figure 2.6). Those larger bond orders to the *ipso* carbon result in somewhat smaller bond orders to C(2), as reflected in C(2)−O and C(2)−S bond lengths about 0.02 Å longer in the radical-cation case than the uncharged case. Considering all of these structural details together, it is apparent that the geometry of the TS structure in the radical-cation case is earlier (i.e., more closely related to the

geometry of the reactant) than is true for the uncharged case, which is consistent with a lower activation energy.

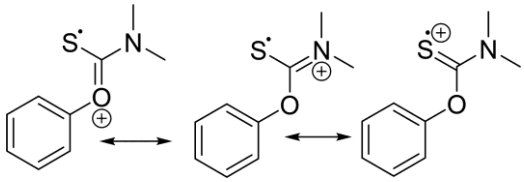

**Figure 2.7.** Resonance structures for the oxidized thiocarbamate group.

Exploring the relationship between TS structure geometries and activation free energies in a bit more detail, we see indeed that, in the neutral case, earlier TS structures, i.e., those having shorter C(2)−S bonds and longer C(2)−O bonds, for example, are associated with lower free energies of activation, and there is a good, linear-free-energy relationship for these and related bond length variations (Figure 2.8). However, no correlations with reactant (or product) geometries were identified.

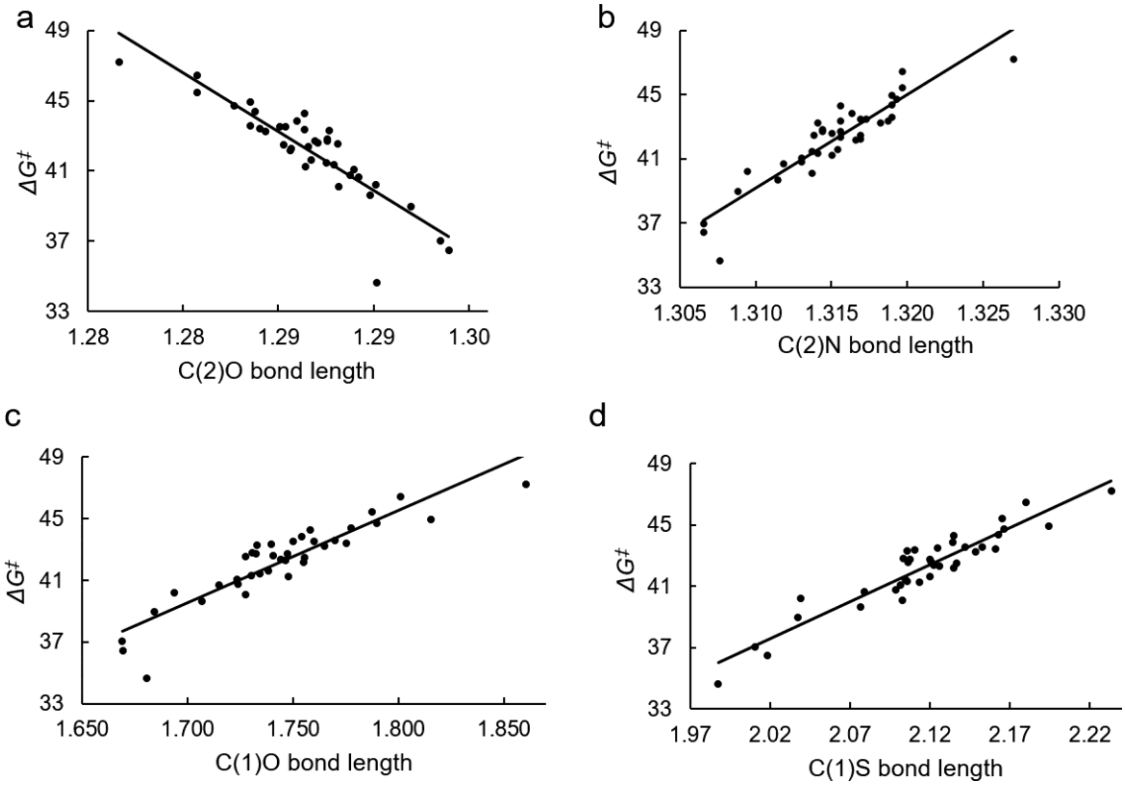


**Figure 2.8.** Uncharged NKR activation free energies (kcal $mol^{-1}$) vs bond distances (Å) in the TS structures for C(2)−O (A), C(2)−N (B), C(1)− O (C), and C(1)−S (D), with best fit lines

shown for all cases ($R^2$ values of 0.783, 0.840, 0.820, and 0.885 for A, B, C, and D, respectively).

By contrast, the closer correspondence between TS structures and reactants in the case of the oxidized NKR substrates leads to reasonably good linear relationships relating the free energies of activation to shorter C(2)=S and longer C(2)−O bonds in the substrates (Figure 2.9).

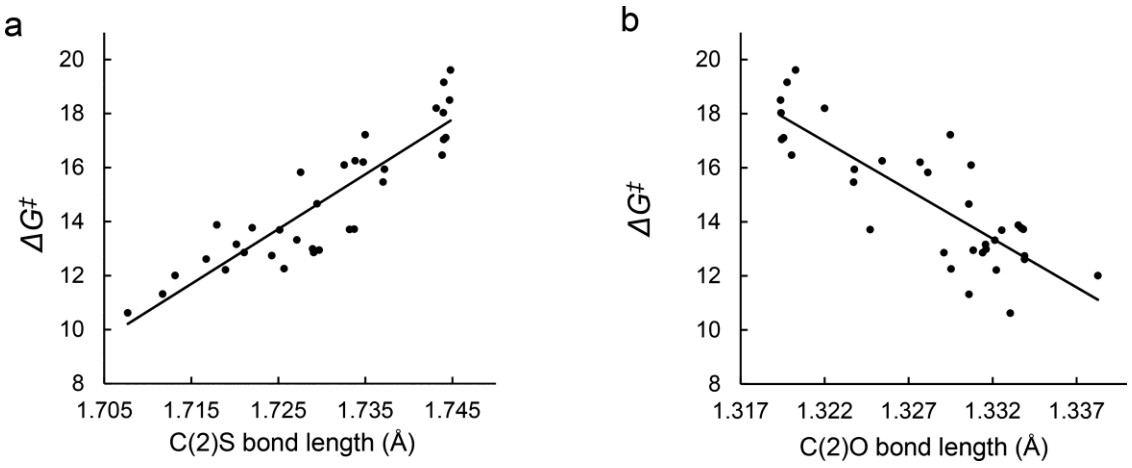


**Figure 2.9.** Radical cation NKR activation free energies (kcal $mol^{-1}$) vs bond distances (Å) in the educt structures for C(2)□S (A) and C(2)−O (B), with best fit lines shown for both cases ($R^2$ values of 0.798 and 0.685 for A and B, respectively).

This variation in structure and reactivity as a function of substitution pattern is associated with the manner in which individual substituents influence the overall charge and spin distribution in the rearranging fragments, and we explore this issue below. Prior to that, however, we first assess some key geometries to consider an interesting puzzle reported by Perkowski et al.[11] In particular, these authors noted that *O*-2-(naphthyl)-*N*,*N*-dimethylthiocarbamate and *O*-3-methoxyphenyl-*N*,*N*-dime- thylthiocarbamate were unreactive as radical cations, even though they rearrange readily under thermal conditions when uncharged. This result is consistent with the computed activation free energy for these compounds vs their regioisomers. For *O*-3-methoxyphenyl-*N*,*N*-dimethylthiocarba mate, *O*-4-methoxyphenyl-*N*,*N*-dimethylthiocarbamate, *O*-2- (naphthyl)-*N*,*N*-

dimethylthiocarbamate, and *O*-1-(naphthyl)- *N*,*N*-dimethylthiocarbamate, the computed activation free energies are 21.0, 13.2, 13.7, and 12.7 kcal·mol$^{-1}$ respectively. A closer look at the at the geometries of these substrates (Figure 2.10) reveals that the different charge distributions of these regioisomers results in the sulfur atom interacting with an adjacent carbon, as opposed to the ipso carbon, which latter structure is along the rearrangement reaction coordinate. In the case of the methoxy-substituted isomers, the difference in activation energies is substantial and enough to explain the reactivity of one isomer and not the other. For the naphthyl isomers, however, the difference is relatively small albeit in the proper direction and it is likely that other factors not identified here affect the differential reactivity (e.g., the electron-transfer step to the oxidant, although it is not obvious why there might be a substantial difference for the two isomers and we do not attempt to model that process here).

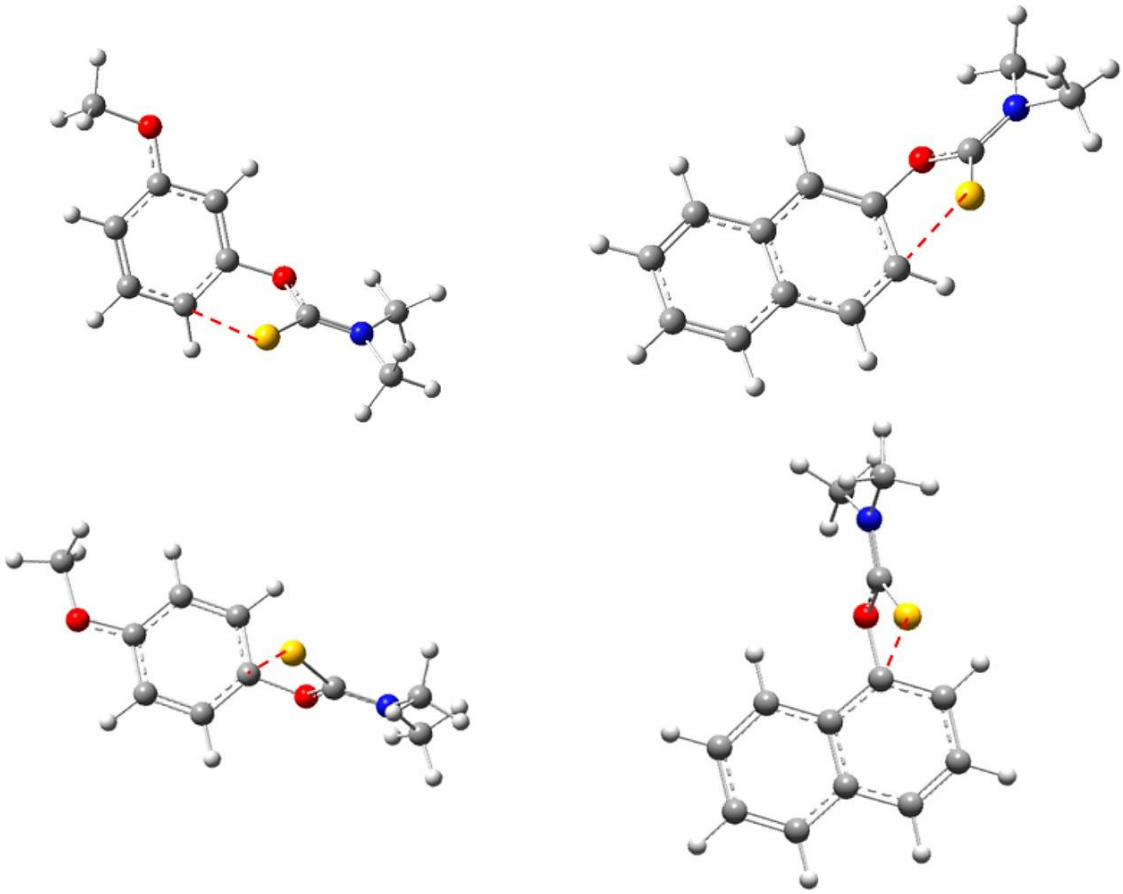

**Figure 2.10.** Optimized geometries of $1^{\bullet+}$ for *O*-3-methoxyphenyl-*N*,*N*-dimethylthiocarbamate (upper left), *O*-4-methoxyphenyl-*N*,*N*- dimethylthiocarbamate (lower left), *O*-2-naphthyl-*N*,*N*-dimethylthiocarbamate (upper right), and *O*-1-naphthyl-*N*,*N*-dimethylthiocarbamate (lower right), highlighting the degree to which polarization of negative charge in the $\pi$ cloud of the aromatic system can influence interaction with the S atom of the oxidized thiocarbamate group.

### 2.3.2 Charge and Spin Distribution

In the case of the uncharged NKR substrates, we observe a high correlation between computed activation free energies and charge separation in the corresponding TS structures. In particular, we find that increased charge separation leads to lower free energies of activation, with the separation in question being a buildup of positive charge on the thiocarbamate fragment and corresponding negative charge on the aromatic ring fragment (Figure 2.11).

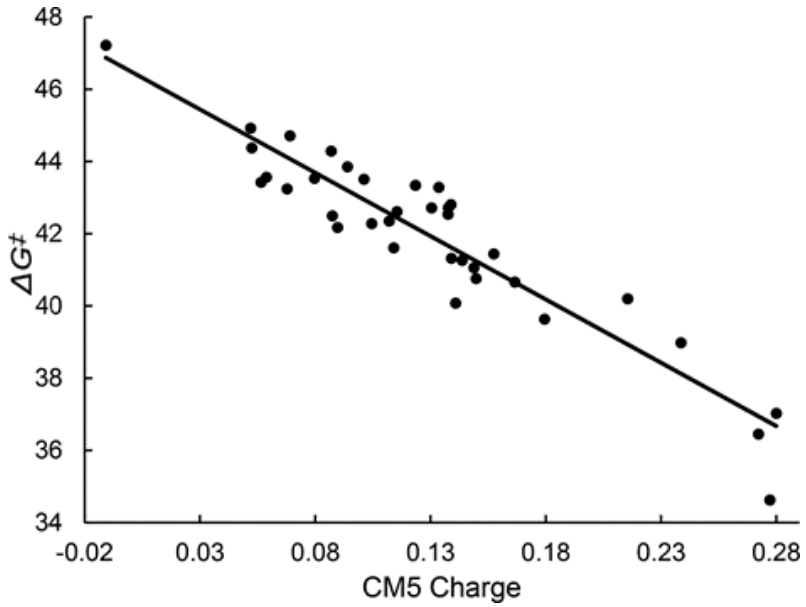


**Figure 2.11.** Uncharged NKR activation free energies (kcal $mol^{-1}$) vs thiocarbamate group charge (CM5, a.u.); the best fit line is shown and has $R^2 = 0.876$.

As the thiocarbamate fragment is "constant" for the various substrates, the conclusion is that *O*-aryl moieties substituted with groups that stabilize negative charge buildup on the aromatic fragment and by charge balance, then, positive charge on the thiocarbamate accelerate the reaction. This suggests that the uncharged NKR may be viewed as analogous to an intramolecular $S_NAr$ reaction, as nucleophilic aromatic substitution is also accelerated by electron-with- drawing substituents on the aromatic ring.[31] As was the case with geometric descriptors, however, no significant correlation was observed between activation free energies and fragment charge distributions in the uncharged reactants or products.

Considering the radical-cation NKR, in most instances we compute that positive charge is largest on the thiocarbamate fragment in the reactant (consistent with analogous results reported by Pedersen et al.[11b] for a set of 5 substrates also considered here), smallest on the carbamothioate fragment in the product, and lies between these two values for this group in corresponding TS structures. This reflects that over the course of the reaction, the charge begins concentrated on the sulfur atom in the reactant, but is then transferred into the aromatic ring along the reaction coordinate as the S atom comes into conjugation with the aryl moiety. Fascinatingly, however, the charge on the thiocarbamate fragment in the radical-cation TS structures is very nearly constant, between about 0.42 and 0.52 au, across all substrates.

By contrast, the variation in educts ranges from 0.33 to 0.72 and in products from 0.24 to 0.54. This lower sensitivity of the TS structure to aryl substitution patterns is not surprising, given the weaker bonding, and thus resonance, between the aryl fragment and the thiocarbamate fragment at the transition state. As a result, however, those substrates that begin with the *smallest* charge on the thiocarbamate necessarily have overall charge distributions most similar to those found in the corresponding TS structures and thus have the lowest activation free energies (Figure 2.12).

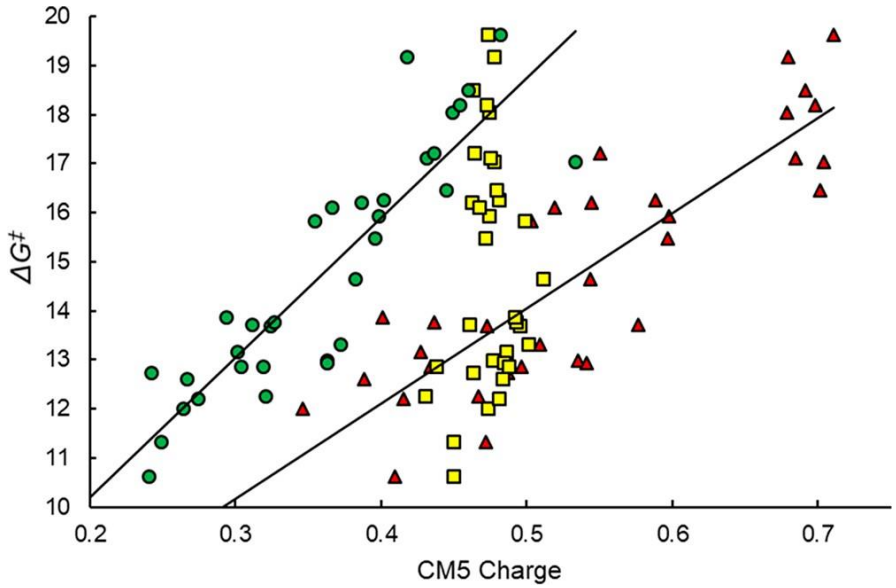


**Figure 2.12.** Radical cation NKR activation free energies (kcal $mol^{-1}$) vs charge on thiocarbamate fragment in $1^{\bullet+}$ (red), $2^{\bullet+}$ (green), and corresponding TS structure (yellow); best fit lines for the first two cases are shown with $R^2$ values of 0.736 and 0.789, respectively.

For the radical-cation NKR, a correlation of reactivity with spin density distribution is also observed (Figure 2.13).

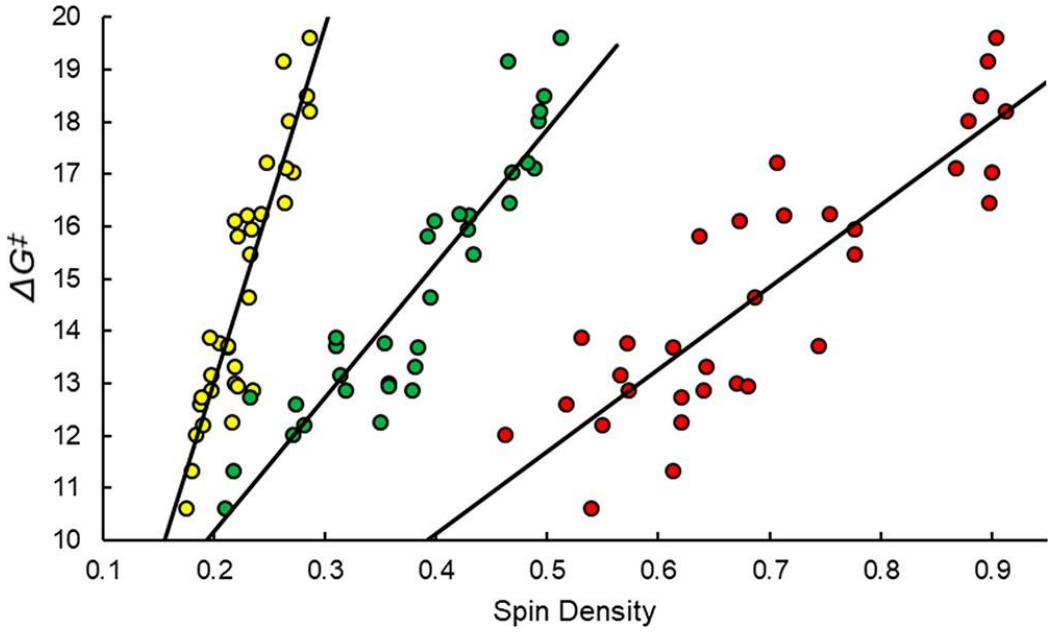

**Figure 2.13.** Radical cation NKR activation free energies (kcal $mol^{-1}$) vs spin on thiocarbamate fragment in $1^{\bullet+}$ (red), $2^{\bullet+}$ (green), and corresponding TS structure (yellow); best fit lines for these three sets are shown with $R^2$ values of 0.755, 0.830, and 0.844, respectively.

Of course, if the spin polarization were to be perfectly correlated with the charge polarization, i.e., no polarization of "paired" electron density between fragments were to take place, this would be a tautology. Interestingly, however, while the spin and charge distributions are quantitatively similar for $1^{\bullet+}$ and $2^{\bullet+}$, there is a much smaller localization of spin on the thiocarbamate fragment in the TS structures than there is of positive charge, so indeed some polarization of paired density *does* occur in these structures. Nevertheless, the same trend is observed, namely, spin, like charge, is transferred from the thiocarbamate fragment to the aromatic fragment along the reaction coordinate, and those substrates that begin with the least spin on the thiocarbamate, and thus have the least to transfer, are computed to have lower activation free energies. Emerging from this analysis is the conclusion that aryl substituents that favor *positive* charge (as well as spin) on the aromatic ring will accelerate the radical-cation NKR, which is precisely the opposite of the situation for the uncharged NKR, as originally empirically observed by Perkowski et al.,[11a] and further extended by Pedersen et al.[11b] under non-photocatalytic oxidative conditions, with both groups emphasizing that this reversal of substituent effect for the radical cations usefully extends the scope of the NKR.

The discussion to this point can be well captured in the reaction coordinate diagram of Figure 2.14.

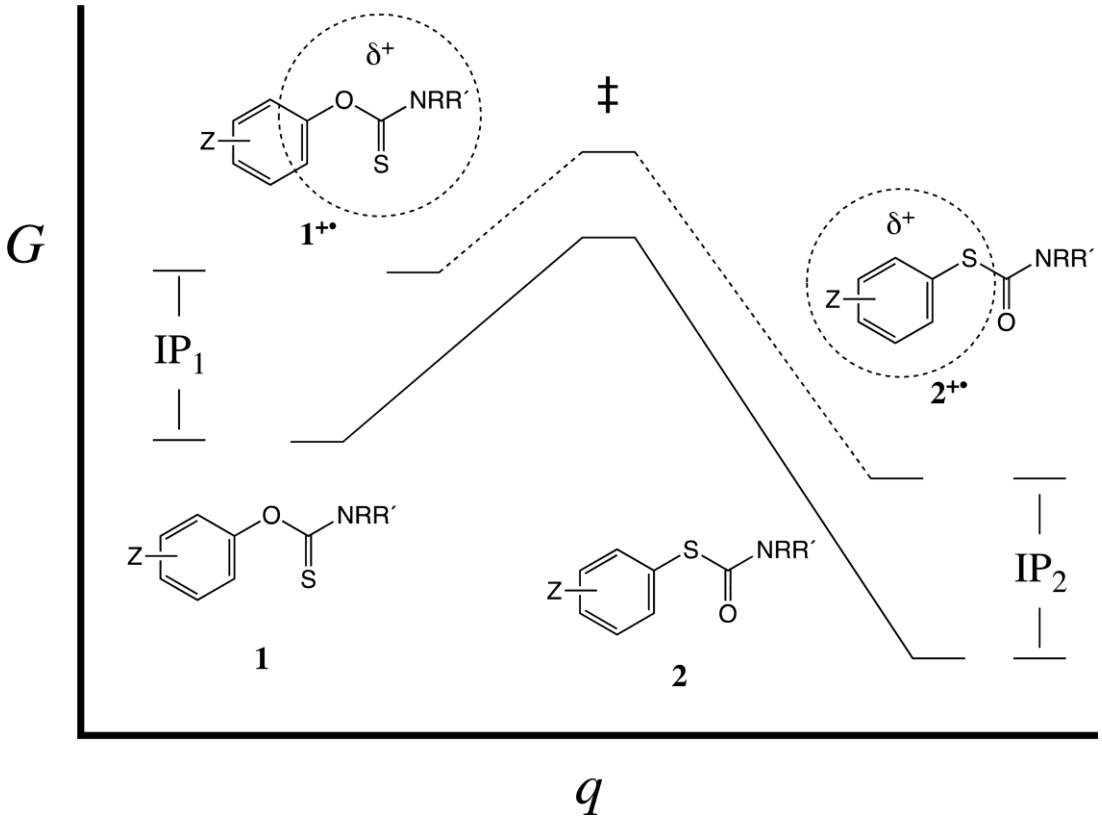


**Figure 2.14.** Qualitative reaction coordinate (*q*, arbitrary units, TS structures defining zero) diagram for uncharged and radical-cation NKRs. Regions of primary positive charge localization in radical-cation educts and products are surrounded by dashed circles.

Ionization of 1 to $1^{\bullet+}$, which requires energy $IP_1$, leads to a reactant with positive charge primarily concentrated in the thiocarbamate and, thus, only weakly influenced by aromatic substituents Z. Ionization also moves the reactant closer to the TS structure along the reaction coordinate *q* than is true for the uncharged case. The TS structure itself, with its partially made and broken bonds, is more easily ionized than reactants or products, which accelerates the radical-cation reaction relative to the uncharged reaction. Finally, in the product carbamothioate $2^{\bullet+}$, the positive charge is primarily concentrated on the thioaryl system, and thus significantly influenced by the nature of substituting groups Z. While strong electron-donating groups should therefore accelerate the reaction, as their influence is felt to a larger extent in the TS structure than in the educt, if they are

*so* strong as to render $IP_2$ less than $IP_1$, then the reaction will only proceed in the presence of external oxidants having greater oxidizing power than $2^{\bullet+}$.

### 2.3.3 Optimization of the Thiocarbamate

Armed with the above analysis, one may ask whether it is possible to make further changes to the radical-cation NKR protocol in order to accelerate the reaction of substrates that do *not* have substituents that stabilize transfer of positive charge and spin to the aromatic ring. The remaining option is to *de*stabilize the accumulation of positive charge on the thiocarbamate, and this may in principle be accomplished by changing the amine component to something less $\pi$-electron donating than dimethylamine. Such diminution may be accomplished in either (or both) of two ways, (i) by increasing the steric bulk of the amine substituents so that the nitrogen lone pair must rotate out of conjugation with the remainder of the $\pi$ system in order to accommodate them or (ii) by substituting the amino nitrogen with functionality that is electron withdrawing. Such engineering is particularly attractive insofar as the thiocarbamate is merely a prosthetic group with respect to the net transformation of phenols to thiophenols.

**Scheme 2.1**

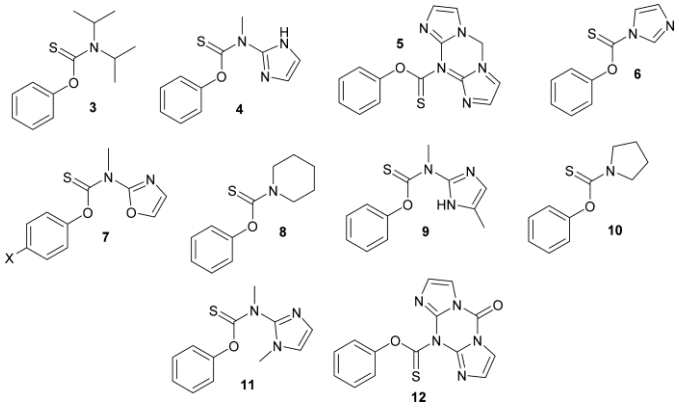


As shown in Table 2.2, the optimal amino group is derived from *N*-methyl-*N*-(2-imidazolyl)amine, with the activation free energy for $4^{\bullet+}$ predicted to be 14.0 kcal $mol^{-1}$. In addition to destabilizing the educt, the proton of the imidazole ring stabilizes the TS structure somewhat through a hydrogen bond to the developing carbonyl oxygen. The use

of *N*-methyl-*N*-[2-(4-methylimidazolyl)]amine, $9^{\bullet+}$, similarly leads to a low activation free energy of 15.0 kcal mol$^{-1}$.

**Table 2.2.** M06-2X/def2-TZVP-Computed Electron Transfer and Activation Free Energies (298 K, kcal mol$^{-1}$) for the Newman−Kwart Rearrangement of Alternative Thiocarbamate Radical Cations in Scheme 2.1

| | $3^{\bullet+}$ | $4^{\bullet+}$ | $5^{\bullet+}$ | $6^{\bullet+}$ | $7^{\bullet+}$ | $8^{\bullet+}$ | $9^{\bullet+}$ | $10^{\bullet+}$ | $11^{\bullet+}$ | $12^{\bullet+}$ |
|---|---|---|---|---|---|---|---|---|---|---|
| $\Delta G_{ET}$ | −8.7 | −6.2 | 2.1 | 5.8 | −6.4[a] | −6.1 | −6.9 | −5.4 | −5.6 | −10.3 |
| $\Delta G^{‡}$ | 19.2 | 14.0 | 19.9 | 14.9 | 14.9[a] | 16.9 | 15.0 | 18.3 | 15.8 | 17.9 |

[a]X = H

However, this group is probably not a good synthetic choice, as the availability of an acidic proton may lead to ionization of the radical cation and open up unproductive reaction paths.

Another case having a low activation free energy, 14.9 kcal mol$^{-1}$, is thiocarbamidazolate $6^{\bullet+}$. However, in the case of $6^{\bullet+}$, the electron transfer from the uncharged substrate to the radical cation of the product $\Delta G_{ET}$ is predicted to be endergonic by 5.8 kcal mol$^{-1}$, suggesting a reaction that will fail to proceed under chain reaction conditions (although use of an external oxidant would obviate this concern). An endergonic radical chain is also predicted for $5^{\bullet+}$, albeit of smaller magnitude. In addition, for substrates $3^{\bullet+}$, $10^{\bullet+}$, and $12^{\bullet+}$, the predicted activation free energies are either very close to or slightly in excess of that for $1^{\bullet+}$, making them likely poor alternatives as well.

Of the remaining alternatives, *N*-methyl-*N*-(2-oxazolyl)- amine, $7^{\bullet+}$, shows the most promise, with predicted $\Delta G_R$ and $\Delta G^{‡}$ values of −6.4 and 14.9 kcal mol$^{-1}$, respectively. At298 K, one would expect from transition-state theory that $7^{\bullet+}$ would undergo unimolecular rearrangement about 100-fold faster than $1^{\bullet+}$. To test the generality of the 2-oxazolyl substituent, we also examined the corresponding rearrangements for $7^{\bullet+}$ vs $1^{\bullet+}$ for the cases of X = F (13.0 and 16.5 kcal mol$^{-1}$, respectively) and X = OMe (12.6 and 13.2 kcal mol$^{-1}$, respectively), so the acceleration diminishes with increasing intrinsic reactivity, but $7^{\bullet+}$ still remains more reactive. To test the situation further, we examined the analogous 3- methoxyphenyl analogues of $7^{\bullet+}$ and $1^{\bullet+}$, recalling that the *meta* electron

donating group slows the reaction by stabilizing an unreactive reactant conformation (vide supra). Again, $7^{\bullet+}$ is predicted to be more reactive than $1^{\bullet+}$, with $\Delta G^{\ddagger}$ values computed to be 18.5 and 21.0 kcal $mol^{-1}$, respectively.

## 2.4 Conclusions

The mechanisms of Newman−Kwart rearrangements under thermal conditions and under conditions that lead to the generation of radical-cation substrates were characterized by quantum-chemical methods. In the case of the uncharged thermal process, the transformation may be viewed as an intramolecular $S_NAr$ which is accelerated in the usual way for such reactions by electron-withdrawing substituents, although even the lowest activation free energies remain on the order of 35 kcal $mol^{-1}$. The radical-cation rearrangements, by contrast, proceed with substantial transfer of hole character both charge and spin from the thiocarbamate fragment to the aryl fragment along the reaction coordinate. As such, the radical- cation reactions are accelerated by electron *donating* substituents, and the driving force associated with the charge transfer lowers the activation free energies substantially for the radical-cation Newman−Kwart reaction compared to the uncharged thermal variant. In the most favorable radical- cation cases, however, the radical-cation product may be so stable that it is endergonic to oxidize another molecule of substrate in order to continue a radical chain, which will be unproductive in the absence of other sufficiently strong oxidants. Various geometric parameters in related transition- state structures show linear relationships with activation free energies for both the neutral and radical-cation reactions, but it is only for the latter case that analogous relationships are observed for geometric parameters in the educts, reflecting the “early” character of the transition state in the radical-cation case. To further accelerate the rearrangement in the radical-cation
reaction, modifications of the amine portion of the thiocarbamate group show promise, and theory predicts that replacing *N*,*N*-dimethylamino with *N*-methyl-*N*-2-oxazolylamino should lead to rate increases of up to 100-fold for less reactive substrates.[62]

### 2.5 DLPNO-CCSD(T) Computations:

The DLPNO-CCSD(T) complete basis set (CBS) energies were estimated using a 2-point extrapolation[1,2], as described below.

The total CBS energy can be expressed in the following way:

$$E^{CBS} = E_{HF}^{CBS} + E_{corr\ (DLPNO-CCSD)}^{CBS} \quad (2.1)$$

Where the first term is the CBS Hartree-Fock (HF) energy, described as:

$$E_{HF}^{CBS} = \frac{E_{HF}^{X} e^{-\alpha\sqrt{Y}} - E_{HF}^{Y} e^{-\alpha\sqrt{X}}}{e^{-\alpha\sqrt{Y}} - e^{-\alpha\sqrt{X}}} \quad (2.2)$$

And the second term is the CBS correlation energy at the CCSD(T) level, expressed as:

$$E_{corr\ (DLPNO-CCSD)}^{CBS} = \frac{E_{corr}^{X} X^{\beta} - E_{corr}^{Y} Y^{\beta}}{X^{\beta} - Y^{\beta}} \quad (2.3)$$

X and Y are the cardinal numbers for de2-SVP and def2-TZVP basis sets, respectively. The values of α and β are 10.39 and 2.40, respectively. Since the β parameter is optimized for CCSD and not CCSD(T), the triple corrections were added separately, from the def2-TZVP calculations. The total energy, then, is found by adding the triple corrections to $E^{CBS}$:

$$E^{tot} = E^{CBS} + T \quad (2.4)$$

The relevant energetic values are found in tables S1 and S2 in reference 26. The energies were calculated at the optimized geometries at the M06-2X/6-31G+(d) level of theory, using the SMD solvation model. However, the energies reported in tables S1 and S2 (see reference 26), including the DFT values, do not have solvation effects taken into accounts.

# Chapter 3

**Synopsis**

Temperature can affect many biological and chemical processes within a body. During *in vivo* measurements, varied temperature can impact the accurate quantitation of additional abiotic factors such as oxygen. During magnetic resonance imaging (MRI) measurements, temperature of the sample can be increased with the absorption of radiofrequency energy, which needs to be well-regulated for thermal therapies and long exposures. To address this potentially confounding effect, temperature can be probed intentionally using reporter molecules to determine the temperature *in vivo*. This work describes a combined experimental and computational approach for the design of fluorinated molecular temperature sensors with the potential to improve accuracy and sensitivity of $^{19}$F MRI-based temperature monitoring. These fluorinated sensors are being developed to overcome the temperature sensitivity and tissue limitations of the proton resonance frequency (10 x $10^{-3}$ ppm °$C^{-1}$), a standard parameter used for temperature mapping in MRI. Here we develop (perfluoro-[1,1'-biphenyl]-4,4'-diyl)bis((heptadecafluorodecyl)sulfane), which has a nearly 2-fold increase in temperature responsiveness, compared to the proton resonance frequency and the $^{19}$F MRI temperature sensor perfluorotributylamine, when tested under identical NMR conditions. While $^{19}$F MRI is in the early stages of translation into clinical practice, development of alternative sensors with improved diagnostics will help advance development and incorporation of fluorine magnetic resonance techniques for clinical use.

## 3.1 Introduction

Temperature sensing in clinical applications can provide information about altered homeostasis and progression of disease.[63,64] The body consistently regulates biochemical processes where body temperatures can fluctuate daily within 1-5 °C.[65,66] Therefore, the ability to accurately monitor variations in deep-tissue temperature could help evaluate the progression of disease or the efficacy of heat-based therapy.[67,68] However, external temperature sensors obtain an average temperature at the local surface of the orifice of

interest, making the sensors unsuitable for quantitative, noninvasive monitoring of deep-tissue internal temperatures.

In medicine, magnetic resonance (MR) thermometry is one of the most advanced systems for noninvasive body temperature measurements. Techniques have been developed to monitor internal temperature, for example, in cases involving strokes.[69] Temperature can be quantitated by measuring the changes in nuclear magnetic resonance (NMR) chemical shifts, growth of resonances due to chemical exchange, and nuclear spin relaxation rates.[70–75] Temperature analysis via changes in chemical shift are well- validated and highly adopted NMR-based techniques.[76–78] In MRI, temperature mapping can use the proton resonance frequency (PRF).[70,79] The PRF is a techniques where the resonance frequencies of protons ($^{1}H$) from water, are measured by applying a gradient-echo-based pulse sequence (dephasing and rephasing signals) and measuring the phase shift as a function of temperature to determine the phase coefficient. The difference in phase shifts can be made into a 2D temperature map to determine relative changes in temperature. Recently, Gorny et al. were able to implement real-time PRF-based thermometry to accurately monitor microwave ablation treatments of hepatic tumors.[80]

adipose nearly undetectable.[81] Additionally, the PRF is dependent on the magnetic field and is highly susceptible to magnetic inhomogeneity, where a magnetic field drift of 0.02 ppm $h^{-1}$ would generate an error of ± 2 °C, during a 1 h measurement.[73]

As complementary and alternative methods to 1H MRI, fluorine-based NMR and MRI are gaining traction for preclinical and clinical diagnostic studies. The fluorine-19 (19F) isotope is 100% naturally abundant and has a gyromagnetic ratio similar to 1H, meaning the frequencies to tune between proton and fluorine should be fairly close. Most importantly for 19F MRI, there is no observable endogenous fluorine in the background of 19F MRI scans. Therefore, the localization of fluorinated probes is well-defined and can be overlaid with 1H MRI to correlate with anatomical space. Currently, the state-of-art perfluorocarbon (PFC)-based thermometry sensor is perfluorotributylamine (PFTBA) with a maximal thermal responsiveness of 9.8 x 10 3 ppm $°C^{-1}$, which limits its desirability, compared to PRF temperature mapping, despite its ability to directly

determine absolute temperature. Thus, there is a need for a more, highly responsive, MR-based temperature probe to improve temperature accuracy measurements. With this goal in mind, we describe the rational design of a fluorine-based molecular temperature sensor with a nearly 2-fold improvement in temperature responsiveness as assessed by 19F NMR, compared to the PRF temperature mapping technique.

## 3.2 Experimental Methods

*19F NMR Variable Temperature Measurements*. Compounds were dissolved in CDCl3 and measured on a Bruker Avance III 500 equipped with a 5 mm BBFO smartprobe. Fluorine spectra were obtained at 471 MHz with dummy scans = 0, acquisition time = 2 s, delay time = 8.1 s, pre-scan delay = 100 μs, the number of scans ≥ 8. Temperature was increased by passing heated N2 gas over the spinning sample which was monitored by an internal instrument temperature probe; temperature was allowed to stabilize for ≥ 5 min. At each temperature, the sample underwent shimming to correct for magnetic inhomogeneities. PFTBA measurements were made by either measuring neat PFTBA in an NMR tube with a flame-sealed capillary tube filled with D2O, suspending PFTBA-filled mesoporous silica nanoparticles in H2O:D2O (9:1 v/v),20 or by sonicating neat PFTBA in CDCl3 for 10-15 minutes, then vortexing the sample prior to insertion into the instrument.

*Computation of Temperature Sensors.* To find energetically favorable conformers at a given temperature, Monte Carlo searches were first carried out using the OPLS3 force field.[82] All identified minima were then re-optimized at the M06-L[83] density functional theory (DFT) level using the 6-31+G(d,p)[47] basis set. Harmonic vibrational frequencies were computed at this level to verify the nature of all stationary points and for use in molecular vibrational partition functions using the quasi-harmonic-oscillator approximation[48] (where all frequencies below 50 $cm^{-1}$ are replaced by values of 50 $cm^{-1}$). Single point DFT calculations at the M06-2X/6-311+G(d,p) level of theory were carried out for all optimized structures to obtain improved electronic energies to which thermal contributions to free energy were added from the M06-L/6-31+G(d,p) step.[46] To obtain

the computationally predicted NMR spectra, single point DFT calculations on the minima were carried out at the B3LYP/6-311+G(d,p) level of theory,[19,84] and the gauge-independent atomic orbital method (GIAO) was used to obtain the chemical shifts.[85]

DFT calculations were accomplished with the Gaussian 16 suite of electronic structure programs,[86] and force-field Monte Carlo searches were accomplished with MacroModel.[87]

## 3.3 Results and Discussion

### 3.3.1 PFTBA Temperature Sensing is Enhanced in Chloroform.

The current state-of-art $^{19}F$ NMR temperature sensor, PFTBA, is a commercially available compound with three fluorinated alkyl tails. Temperature measurements with PFTBA work by comparing the relative change in chemical shifts between two non-equivalent fluorine groups (e.g., $CF_3$ and $\gamma$-$CF_2$) on the fluorinated alkyl tail, where the NMR frequency difference between two fluorinated groups can be plotted as a function of temperature (i.e., $\Delta\Delta\delta(T)$) to determine responsiveness (Figure S1a-c in reference 27). PFTBA was analyzed as a model sensor to benchmark temperature measurements in different solvents and chemical environments we expected to use for our new sensors (Figure 3.). PFTBA was measured as either a neat liquid, within an aqueous environment encapsulated by previously reported mesoporous silica nanoparticles (PERFUMNs),[88] or in $CDCl_3$. In the case of the neat PFTBA, the $\alpha$-$CF_2$ and $\beta$-$CF_2$ had the lowest thermal response of ~ 1 x $10^{-3}$ ppm $°C^{-1}$, while the $\gamma$-$CF_2$ and $CF_3$ were the most responsive combination with a thermal response of ~ 9 x $10^{-3}$ ppm $°C^{-1}$, which is consistent with literature.[89]

While there was no significant difference in thermal response between neat PFTBA and PFTBA-filled nanoparticles, the temperature response was significantly different for PFTBA in $CDCl_3$. Only the pairings that contained $\gamma$-$CF_2$ and $CF_3$ were different, demonstrating that the solvent effect is only significant to the most solvent exposed fluorine groups. Interestingly, the thermal response was diminished with $\gamma$-$CF_2$ pairings and enhanced with $CF_3$ parings, indicating opposing behavior between the fluorine

groups. Thermal enhancement only raised responsiveness by 2-3 x $10^{-3}$ ppm $°C^{-1}$ per combination. In the case of the γ-CF2:CF3 pair, ΔΔδ(T) increased from 9.5 x $10^{-3}$ ppm $°C^{-1}$ to 11 x $10^{-3}$ ppm $°C^{-1}$. Based on these findings, we sought to design and test fluorinated compounds with at least two or more magnetically distinct fluorine groups. Despite the small increase in responsiveness in CDCl3, this solvent was chosen for further analysis due to the ability to dissolve a large range of fluorinated small molecules.

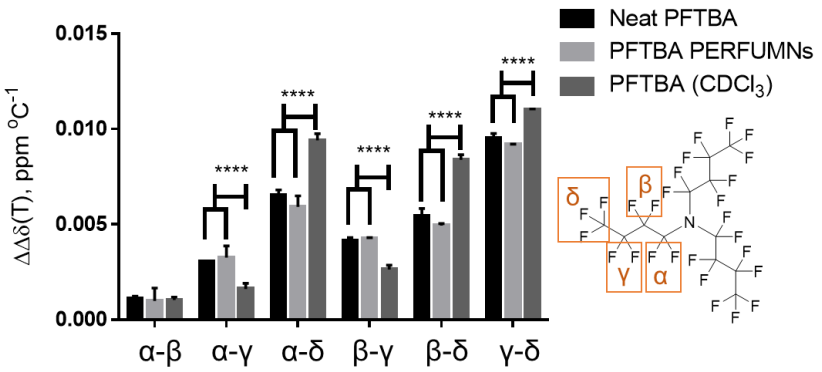


**Figure 3.1.** Comparison of perfluorotributylamine (PFTBA) NMR thermal response as neat PFTBA, encapsulated as PERFUMNs in water, and in $CDCl_3$. The PFTBA structure is included on the right. Neat PFTBA has a thermal response similar to PFTBA PERFUMNs dispersed in water. Neat PFTBA dispersed in $CDCl_3$ has significantly higher thermal response for the most sensitive pair of fluorine groups (positions γ and δ), indicating a solvent effect. There is no significant difference for the $CF_2$ groups near the center nitrogen (positions α and β). The p-value is < 0.0001 for significant terms. Greek characters indicate the assignment of the fluorine group.[90]

### 3.3.2 Computation Predicts Relative Temperature Sensing Performance between PFTBA and Commercial Fluorinated Compound

In an effort to have a more directed rationale for the synthesis of novel compounds, we computationally determined the thermal response of several fluorinated compounds. The theoretical chemical shifts from computational analysis are based on the energetic contributions of conformers at a given temperature. These conformations are influenced

by physiochemical phenomena such as: steric strain, torsional strain, electrostatic interactions, and conjugation.[91,92]

For appreciable temperature responses, two conditions must be met: first, the chemical shift of certain fluorine atoms must differ significantly across different conformers. Secondly, the energy difference between conformers with differing chemical shifts must be such that their populations vary substantially in the temperature range being measured.

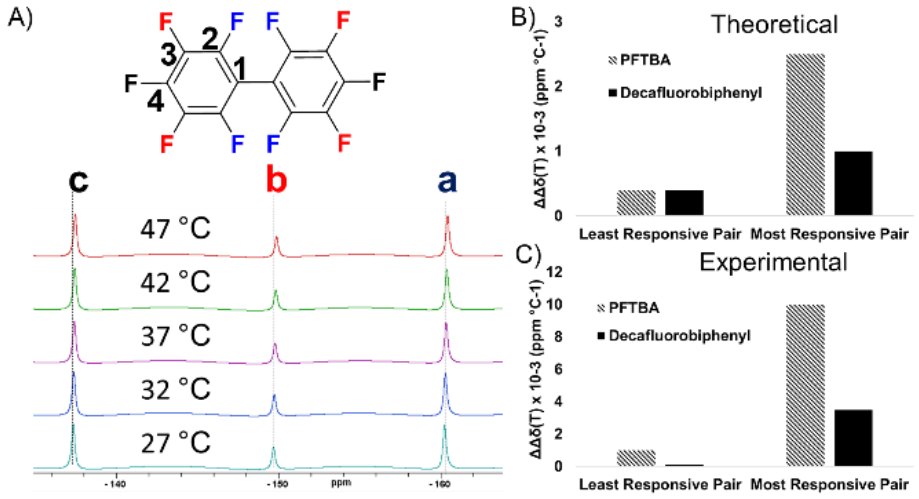


**Figure 3.2.** Temperature response of decafluorobiphenyl and comparison to perfluorotributylamine (PFTBA). (A) $^{19}$F NMR spectra of decafluorobiphenyl as temperature increases. The assignments for fluorine groups are colored to match their assignment on the spectrum; a (blue) = 2,2′,6,6′-F, b (red) = 3,3′,5,5′-F, c (black) = 4,4′-F. [93](B) Computational and (C) experimental comparison of thermal response (ΔΔδ(T)) between decafluorobiphenyl and perfluorotributylamine. The graph compares the quantified response of PFTBA vs decafluorobiphenyl based on the most and least responsive fluorine group pairs.

Decafluorobiphenyl was chosen as a test compound to compare to PFTBA since decafluorobiphenyl has three distinct fluorine groups (Figure 3.2a) directly attached to the biphenyl rings, which would limit the motion and number of conformations affecting the individual fluorine atoms, compared to a fluorinated alkyl tail.[94,95] The chemical shifts for PFTBA and decafluorobiphenyl were determined over a temperature range of 20 °C (Table S1 and S2 in reference 27). Notably, the absolute value of the chemical shifts and

temperature responsiveness were different from experimental values, where the best temperature responsiveness for PFTBA was 2.5 x $10^{-3}$ ppm °$C^{-1}$. The discrepancy in theoretical calculations is likely from differences in environmental and physicochemical conditions yet to be optimized (e.g. solvent, long range interactions, state phases) and limitations from uncertainty in conformer energies, but comparisons between molecules are still useful.

Despite an underestimation in theoretical responsiveness, compared to experimental, decafluorobiphenyl shows a much lower response to temperature compared to PFTBA, with PFTBA performing 2.5-fold (computational) and 2.9-fold (experimental) better than decafluorobiphenyl (Figure 3.2 b-c). The difference in responsiveness between decafluorobiphenyl and PFTBA suggest that fluorine on a more dynamic alkyl tail would be more responsive than fluorine groups appended on a ring. In consideration of the discrepancies, the relative trends in responsiveness for a library of compounds could still give information about where to focus for experimental synthesis. In consideration of the ~4-fold underestimation of PFTBA between theoretical and experimental values, we hypothesized that compounds with theoretical $\Delta\Delta\delta(T)$ greater than 3 x $10^{-3}$ ppm °$C^{-1}$ would potentially overcome the 10 x $10^{-3}$ ppm °$C^{-1}$ PRF threshold.

### 3.3.3 Computation Suggests Best Enhancement from Fluorinated Alkyl Tail Anchored onto a Conformationally Rigid Structure

A library of theoretical compounds were tested with computational analysis over a temperature range of 20 °C and ordered based on their maximal responsiveness (Table 3.1). Compounds were initially selected based on their potential dynamic susceptibility to temperature, for example: the interconversion between restricted isomers on amide- and urea-based compounds, which causes conformational changes to be highly dependent on temperature.[96,97] We also hypothesized that an acetamide-based compound would lead to suitable temperature responsiveness if one fluorinated group was restricted and the other fluorinated group had a temperature-dependent conformational change.

Despite our predictions, most of the amide- and urea-containing compounds had poor temperature responsiveness (<< 1 x $10^{-3}$ ppm $°C^{-1}$). Comparing **I** and **II**, the change from two meta-$CF_3$ to one para-$CF_3$ on the phenyl ring resulted in a 6-fold increase to the thermal responsiveness. At any given temperature the dispersion of chemical shifts predicts that the acetyl-$CF_3$ groups have the largest spread of chemical shifts populations (Table S3 in reference 27), suggesting inherent responsiveness with certain functional groups.

**Table 3.1.** Temperature Response of Theoretical Sensors

| # | Structure | ΔΔδ(T) ppm°C$^{-1}$ | # | Structure | ΔΔδ(T) ppm°C$^{-1}$ |
|---|---|---|---|---|---|
| I | 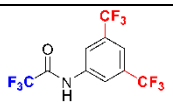 | $5.2 \times 10^{-6}$ | VII | 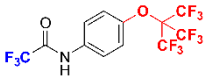 | $8.1 \times 10^{-4}$ |
| II | 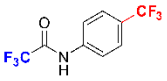 | $3.0 \times 10^{-5}$ | VIII | 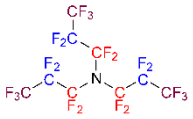 | $9.4 \times 10^{-4}$ |
| III | 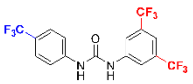 | $2.0 \times 10^{-4}$ | IX | 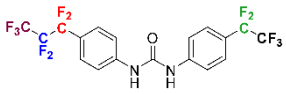 | $1.8 \times 10^{-3}$ |
| IV | 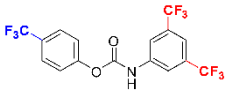 | $2.2 \times 10^{-4}$ | X | 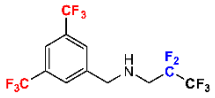 | $2.1 \times 10^{-3}$ |
| V | 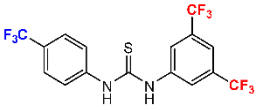 | $2.3 \times 10^{-4}$ | XI | 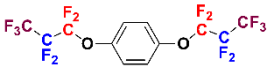 | $2.9 \times 10^{-3}$ |
| VI | 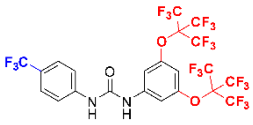 | $5.4 \times 10^{-4}$ | XII | 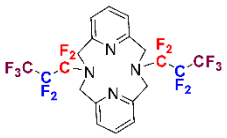 | $11 \times 10^{-3}$ |

For both **I** and **II**, the acetyl-$CF_3$ was the most responsive fluorine group (Table S4 in reference 27). A 38-fold increase in ΔΔδ(T) occurred (relative to **I**) when converting to

(thio)urea- and carbamate-based compounds (**III**-**V**). Compounds **III**-**V** also show slight changes in temperature responses when different heteroatoms are incorporated at the core of the urea-based structure. Furthermore, the effects of the amide bond rotation appeared to be minimal since a slight increase in thermal response was seen between **III** and **IV** when the urea nitrogen was changed to an oxygen atom in the carbamate. Alternatively, compound **VI** had over a 2-fold increase from **III**-**V**, suggesting that appending a fluorinated group through an ether would be beneficial. Interestingly, **VII** still had a 1.5-fold enhancement despite going from urea to acetamide. Having less $CF_3$ groups and/or a substituent in the para-position enhanced the theoretical temperature response with **VII,** as seen with **I** to **II**. Of note, with phenyl $CF_3$ groups, the fluorine atoms are symmetrically correlated such that their degenerate conformations, which are identical in energy and geometry but not labeling, may not be captured (Figure S2 in reference 27). With only specific ordering of fluorine atoms captured, the predicted thermal sensitivities are artificially increased. Averaging the chemical shift of these equivalent fluorine accounts for this symmetry.

Among the initial computational results (**I**-**VII**), we only considered trifluoromethyl groups. On these analyses, it was apparent these substituents on the phenyl ring were insufficient to enhance thermal responsiveness. Greater improvement was seen when fluorinated alky tails were incorporated into the chemical structures (**VIII**-**XII**). **VIII** was analyzed to benchmark effects of a perfluoropropyl-alkyl tail. Compounds **IX**-**XII** approached our theoretical threshold with $\Delta\Delta\delta(T)$ ranging from 1.8-2.9 x $10^{-3}$ ppm $°C^{-1}$ thermal responses. Incorporation of two different fluorinated alkyl chains on the phenyl rings of **IX** led to a 3-fold increase in responsiveness relative to **VI**, the second most responsive urea. On **X**, we combined the phenyl $CF_3$ with a fluorinated alky tail. The most responsive pairing was between the phenyl $CF_3$ and the alkyl $CF_2$ groups, suggesting that a fluorine group on a rigid structure (e.g., phenyl ring) in combination with a fluorinated alkyl tail anchored to the rigid structure would greatly increase responsiveness. Of interest, the benzylic $CF_3$ had the same degenerate correlated

conformers, as seen in **V**, but the alkyl $CF_3$ appeared to have three distinct groups of conformers (Figure S3 in reference 27).

While compound **X** showed promising results by mixing functional groups on rings and fluorinated alkyl tails, compounds **XI** and **XII** suggest that good enhancement can be achieved by simply anchoring the fluorinated alkyl tails onto a conformationally rigid structure. Compounds **XI** and **XII** were generated by appending the fluorinated tail of **VIII** onto a hydroquinone or diazapyridinophane core, respectively. Compound **XII** had the strongest thermal responsiveness with $\Delta\Delta\delta(T) = 11 \times 10^{-3}$ ppm $°C^{-1}$. Therefore, given an underestimation of the theoretical $\Delta\Delta\delta(T)$, these computational analyses supported appending a fluorinated alkyl tail on a larger conformationally rigid, core structure to enhance the experimental responsiveness.

### 3.3.4 Hybrid Compounds with Fluorine Groups on a Rigid Structure and Fluorinated Alkyl Tails are Necessary to Enhance Effects of the Fluorinated Alkyl Tail Alone

As experimental validation for the pattern of responsiveness found in the computational library, several compounds were synthesized to confirm a gradient of insensitivity to substantial enhancement in temperature responsiveness, and the theoretical thermal response of these new compounds were also computed (Table ). The computational values for the thermal response correlate with the experimental values, except for compound 4, which is an outlier. Compounds **1** and **2** were synthesized with the expectation that the barrier to rotation of the thiourea would hinder the rotation of the R groups around the two nitrogens (Figure S4a-b in reference 27). As expected both of the compounds performed poorly with a $\Delta\Delta\delta(T)$ of $0.40 \times 10^{-3}$ ppm $°C^{-1}$ and $2.5 \times 10^{-3}$ ppm $°C^{-1}$, respectively (Figure S4c-d in reference 27). Based on As experimental validation for the pattern of responsiveness found in the computational library, several compounds were synthesized to confirm a gradient of insensitivity to substantial enhancement in temperature responsiveness, and the theoretical thermal response of these new compounds were also computed (Table 3.2). The computational values for the thermal response correlate with the experimental values, except for compound 4, which is an

outlier. Compounds **1** and **2** were synthesized with the expectation that the barrier to rotation of the thiourea would hinder the rotation of the R groups around the two nitrogens (Figure S4a-b in reference 27). As expected both of the compounds performed poorly with a $\Delta\Delta\delta(T)$ of 0.40 x $10^{-3}$ ppm $°C^{-1}$ and 2.5 x $10^{-3}$ ppm $°C^{-1}$, respectively (Figure S4c-d in reference 27). Based on these results we moved forward to measure the effects of a fluorinated alkyl tail attached to a rigid structure.

A simple fluorinated tail was needed to test the hypothesis derived from the computational library. Therefore, 2,2,3,3,3-pentafluoropropylamine was selected due to its commercial availability, two distinct fluorine groups ($CF_2$ and $CF_3$), and a methylene between the fluorine and the nitrogen to allow for better reactivity for synthesis.

**Table 3.2.** Thermal Response of Synthesized Compounds

| # | Structure | **$\Delta\Delta\delta(T)$, $\times10^{-3}$ ppm $°C^{-1}$ (Experiment)** | **$\Delta\Delta\delta(T)$, x$10^{-3}$ppm$°C^{-1}$(Theory)** |
|---|---|---|---|
| 1 | 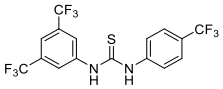 | 0.4 | 0.23 |
| 2 | 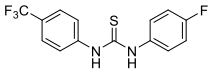 | 2.5 | 0.30 |
| 3 | 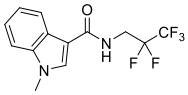 | 10.1 | 0.92 |
| 4 | 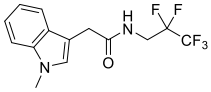 | 10.4 | 0.24 |
| 5 | 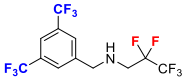 | 12.5 | 2.06 |
| 6 | 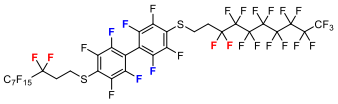 | 19.5 | 5.92 |
| 7 | 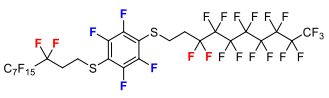 | 18.9 | 7.21 |

With the pentafluoroproplyamine as a precursor, compounds **3** and **4** (Figure S5a, Figure S6a in reference 27) were synthesized via acylation reactions to append a fluorinated tail onto a rigid structure. Encouragingly, **3** and **4** had a responsiveness at the PRF threshold with $\Delta\Delta\delta(T) = 10.3 \times 10^{-3}$ and $10.4 \times 10^{-3}$ ppm $°C^{-1}$ respectively (Figure S5b, Figure S6b in reference 27) which is also comparable to PFTBA measured under these conditions ($11 \times 10^{-3}$ ppm $°C^{-1}$) . The response from **3** and **4** support the hypothesis that the fluorinated alkyl tail on a hindered structure would have a strong temperature response. In addition, the $CF_2$ group was the most responsive to temperature changes. The $CF_2$ on **3** had an individual responsiveness (i.e., $\Delta\delta(T)$) of $8.4 \times 10^{-3}$ ppm $°C^{-1}$; for $CF_2$ on **4** $\Delta\delta(T) = 8.8 \times 10^{-3}$ ppm $°C^{-1}$ (Figure S5c, Figure S6c in reference 27). Interestingly, the resonances of the $CF_3$ groups on **3** and **4** changed as a function of temperature in the opposite direction relative to the $CF_2$ group, with lower magnitudes of $-1.7 \times 10^{-3}$ and $-1.6 \times 10^{-3}$ ppm $°C^{-1}$ respectively, where the negative term was given to upfield movement on the NMR scale.

Compounds **3** and **4** were also made to test if the space between the fluorinated alkyl tail and the rigid structure significantly contributed to the thermal response. While both compounds were able to overcome the PRF threshold, the distance from the rigid body by incorporation of a methylene (**4**) or ethylene (not shown) did not significantly change the $\Delta\Delta\delta(T)$ between compounds (Table S5 in reference 27). Surprisingly, further investigation revealed $\Delta\Delta\delta(T) = 10.5 \times 10^{-3}$ ppm $°C^{-1}$ for the precursor 2,2,3,3,3-pentafluoroproplyamine, indicating that the overall responsiveness was already around its limit, and appending the fluorinated tail onto a rigid structure did not enhance the endogenous temperature response of the precursor (Table S6 in reference 27). Therefore, we hypothesized that a hybrid compound that incorporates fluorine groups on a rigid core with the anchored alkyl tail could experimentally overcome the 1.5-fold enhancement relative to the PRF threshold.

Since the theoretical data in Table 3.1 suggested that compound **X** was a promising hybrid compound, compound **5** was synthesized with the incorporation of benzylic $CF_3$ groups as the fluorine group on the rigid core, while also maintaining the response of the

$CF_2$ on the fluorinated tail (Figure S7a in reference 27). Consistent with our design hypothesis, **5** improved $\Delta\Delta\delta(T)$ to 12.5 x $10^{-3}$ ppm $°C^{-1}$, making **5** ~ 1.3-fold more responsive than the PRF threshold (Figure S7b in reference 27). Interestingly, the dispersion was able to identify $CF_2$ as the most responsive group, and even suggested the correct pairing for maximal temperature response (Figures S8 and S12 in reference 27). Individually, the movement of benzylic $CF_3$ and alkyl $CF_2$ resonances were similar in magnitude but opposing in direction to temperature changes, as seen with **3** and **4**. Overall, $\Delta\delta(T)$ was -5.9 x $10^{-3}$ and +6.7 x $10^{-3}$ ppm $°C^{-1}$ for the benzylic $CF_3$ and alkyl $CF_2$ groups respectively (Figure S7c in reference 27). Given the opposing behavior of these functional groups in response to temperature changes, we sought to model this relationship, where temperature sensitivity is enhanced due to varying upfield/downfield frequency changes rather than having an insensitive-sensitive fluorine group paring. Based on these relationships, we were able to formulate a new screening method to match fluorine groups to enhance overall thermal sensitivity.

### 3.3.5 Screening Method to Match Different Fluorine Groups Together to Make Novel Sensors

The mathematical relationship between $\Delta\Delta\delta(T)$ and the individual movements of fluorine groups is linear (Supplemental Information "Linear Model for Screening"). As chemical shifts of two fluorine groups move as a function of temperature, at any given temperature, the magnitude between groups is equal to the difference in frequency, i.e., $\Delta\Delta\delta$. Thus the responsiveness, $\Delta\Delta\delta(T)$, is equal to the magnitude between the slopes of the two functional groups (Figure 3.a-b). Based on the relationship determined in our linear model, the more positive (downfield) and negative (upfield) two resonances become, as a function of temperature, the more the magnitude of $\Delta\Delta\delta(T)$ will increase. Experimental data were compiled onto a scale to highlight the relationship between the movements of different fluorine groups (Figure 3.c). Assuming that most fluorine groups, as seen experimentally, are not inherently responsive beyond 10 x $10^{-3}$ ppm $°C^{-1}$, the PRF threshold was used as the boundary for the majority of fluorine groups' responsiveness to

temperature. The propylamine tail (red) shows the $CF_2$ group is beyond the threshold while the $CF_3$ group is between no response and the midpoint.

Essentially, the closer $CF_3$ Δδ(T) (i.e. $m_a$ or $m_b$) is to $CF_2$ group, reduces the magnitude of ΔΔδ(T) for the molecule. Similarly, the effect can be seen with the tail of PFTBA (grey) and in the opposing direction (negative) with compound **2** (green), where Δδ(T) of the fluorine groups are both similar in magnitude and direction. Thus, while most Δδ(T) are within the ± 10 x $10^{-3}$ ppm °$C^{-1}$ boundary, the PRF threshold can be readily overcome by finding a pair with Δδ(T) ≤ -5 x $10^{-3}$ and Δδ(T) ≥ +5 x $10^{-3}$ ppm °$C^{-1}$. Furthermore, if the dispersion can correctly identify the most and least responsive fluorine groups, as seen with **5**, this screening model becomes a tool that can be used with theoretical computation. The modularity from analysis of fluorinated motifs versus fluorinated molecules, is envisioned to drastically reduce the chemical space necessary to identify suitable temperature sensors.

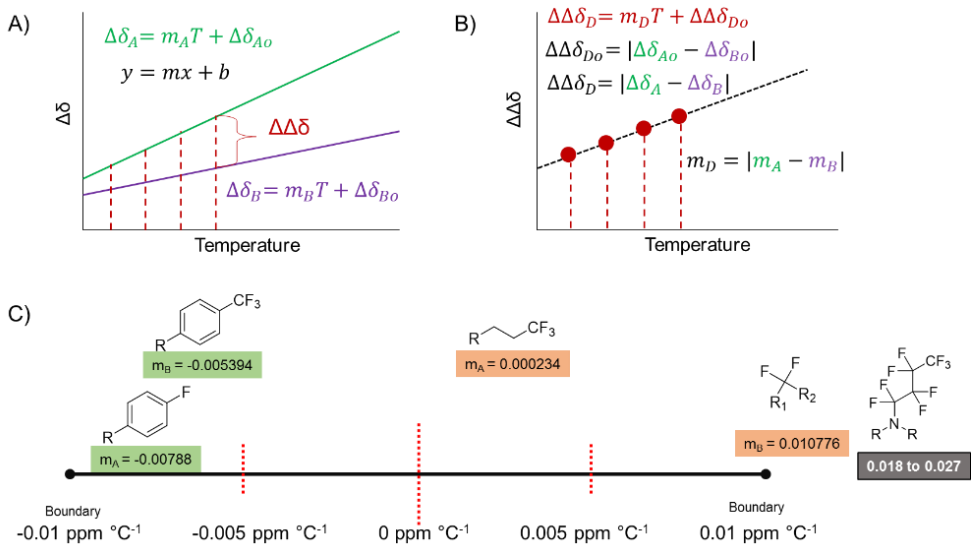


**Figure 3.3.** Computational screening method of functional groups to develop novel fluorinated sensors. (A) Theoretical response of two different fluorine resonances ($\Delta\delta_a$ and $\Delta\delta_b$) as a function of temperature in a linear model. At a given temperature, the difference between $\Delta\delta_a$ and $\Delta\delta_b$ is equal to the ΔΔδ. (B) Theoretical graph of how ΔΔδ(T) is based on the absolute

difference between the slopes of the two functional groups ($\Delta\delta_a$ and $\Delta\delta_b$) as a function of temperature ($\Delta\Delta\delta(T) = m_d$). (C) Scale and boundary of experimental fluorine group responsiveness. The ideal case is to identify two functional groups in the more common regions of responsiveness (e.g., $\pm 7 \times 10^{-3}$ ppm °C$^{-1}$) with opposing directions in response to temperature. The absolute magnitude of difference between those two responsive groups is the overall responsiveness of the temperature probe and should be ≥ 1.5 times the PRF signal. The values under each molecule are from experimental measurements. Color coded numbers are different functional groups on the same molecule. Each fluorine group on PFTBA (right side) has an individual response from 18 to 27 × $10^{-3}$ ppm °C$^{-1}$.

### 3.3.6 Fluorinated Alkyl Tail, Rigid Core Aryl Fluorine, and a Thioether Significantly Enhance Thermal Responsiveness over the PRF Threshold

We sought to test the screening results suggesting the combination of two different fluorinated motifs to generate novel temperature sensors by leveraging synthesis and computational analysis of a new hybrid compound. In general, the phenomenon where one resonance moves downfield while the other moves upfield is likely related to molecular electronics, as well as conformational changes. Previously, analysis with compounds **III-V** and experimental data with precursors for our temperature sensors (Table S6 in reference 27) showed that heteroatoms also impact the thermal response. These differences could be due to a difference in inductive or electron withdrawing effects, hydrogen bonding (if allowed), and/or strain on conformational transition states due to lone pair electronic and valence geometries.

Given the response of the aryl fluorines in our screening model, a perfluorobiphenyl-based test compound was chosen for computational analysis (Figure S9a in reference 27). Experimental temperature responses revealed that the majority of the fluorines on both decafluorobiphenyl and perfluoro-4,4'-biphenol are within the desired negative region for temperature response, i.e., -5 to -10 x $10^{-1}$ ppm ° $C^{-1}$ (Figure S9b-c in reference 27). Additionally, the aryl fluorines, meta- and ortho- to the 4,4'-position, changed their responsiveness when the 4,4'-fluorine were changed to 4,4'-diols, demonstrating a significant effect from the heteroatom in the 4,4' position. Three perfluorobiphenyl

derivatives were computationally analyzed to simultaneously screen for a potentially improved temperature sensor, and investigate the heteroatom effect on responsiveness between nitrogen, oxygen, and sulfur (Figure S10 in reference 27). The analysis revealed that sulfur had the best response among the three derivatives tested. The computation also supported the idea that the resonances of the biphenyl fluorines will not move similarly to the fluorine on the alkyl tail, possibly leading to responses in different directions. No strong correlation was found between the relative orientation of the fluorine atoms to sulfur and their chemical shifts. However, the dispersion indicated that the first $CF_2$ would be the most responsive fluorine group and would pair with an aryl-fluorine (Table S7 in reference 27).

Given the results from the computational study, compound **6** (Figure 3.4 a) was synthesized with a heptadecafluorodecane-1-thiol (due to commercial availability); for the heptadeacluofodecane-1-thiol precursor, $\Delta\Delta\delta(T) = 13.2 \times 10^{-3}$ ppm °$C^{-1}$ (Table S4 in reference 27). Compound **6** had a significant increase in $\Delta\Delta\delta(T)$ of $19.5 \times 10^{-3} \pm 0.2 \times 10^{-3}$ ppm °$C^{-1}$ (n = 3), corresponding to ~2-fold increase in temperature responsiveness relative to the PRF, 1.8-fold increase from PTFBA in $CDCl_3$, and a 1.6-fold increase from **5** (Figure 3.4 b-d). Additionally, **6** is made by substituting the alkyl tail onto the biphenyl ring in the 4 and 4' positions. This substitution pattern maintains an axis of symmetry leading to a doubling of the magnetically equivalent fluorine atoms for better signal-to-noise ratios. The majority of the resonances had $\Delta\delta(T)$ in the hypothetically optimal region ($\pm 5$ to $\pm 10 \times 10^{-3}$ ppm °$C^{-1}$) indicating that almost all combinations could overcome the PRF threshold. The maximum response (green triangles) contained the aryl fluorines, meta to the thioethers (-136 ppm), with $\Delta\delta(T) = -7 \times 10^{-3}$ ppm °$C^{-1}$, and the first $CF_2$ groups on the alkyl tail (-113 ppm), adjacent to the $CH_2$, with $\Delta\delta(T) = +12 \times 10^{-3}$ ppm °$C^{-1}$ (Figure 3.4 e). These results support the hypotheses of the screening method, where: A) the majority of the resonances were within the boundary; B) pairs of resonance that were past $\pm 5 \times 10^{-3}$ ppm °$C^{-1}$ were able to easily overcome the PRF threshold; C) the combination of aryl fluorine with fluorinated alkyl tail significantly improved the overall temperature response. In addition, the data

suggest that for these partially fluorinated alkyl tails, the $CF_2$ adjacent to $CH_2$ will have the largest shift in resonance during changes in temperature as consistent with the dispersion. While the combination of a thioether, fluorinated alkyl tail, and aryl fluorines significantly improved the responsiveness of our lead compound, we did not know if the presence of the biphenyl rings also had a significant impact on the temperature response. Therefore, compound **7** was synthesized, in similar fashion to **6,** with a hexafluorobenzene for the rigid structure (Figure S11a in reference 27).

The most responsive pair of chemical shifts for compound **7** ($1^{st}$ $CF_2$ and aryl fluorine) had a comparable $\Delta\Delta\delta(T)$ of $18.9 \times 10^{-3} \pm 0.4 \times 10^{-3}$ ppm $°C^{-1}$ (n = 2); there was no statistically significant difference between the thermal response of **6** and **7** (Figure S4b-c in reference 27). While there is no significant difference, compound **6** does have a higher responsiveness indicating that the presence of the biphenyl rings has a minor effect on the thermal response. The biphenyl ring, compared to a benzene, should have more conformations and therefore more discrete orientations for the substituents to occupy. A more thorough investigation into the rigid body will be needed to understand how fused rings, linked rings, and different size rings can affect the temperature response of these organofluorine temperature sensors.

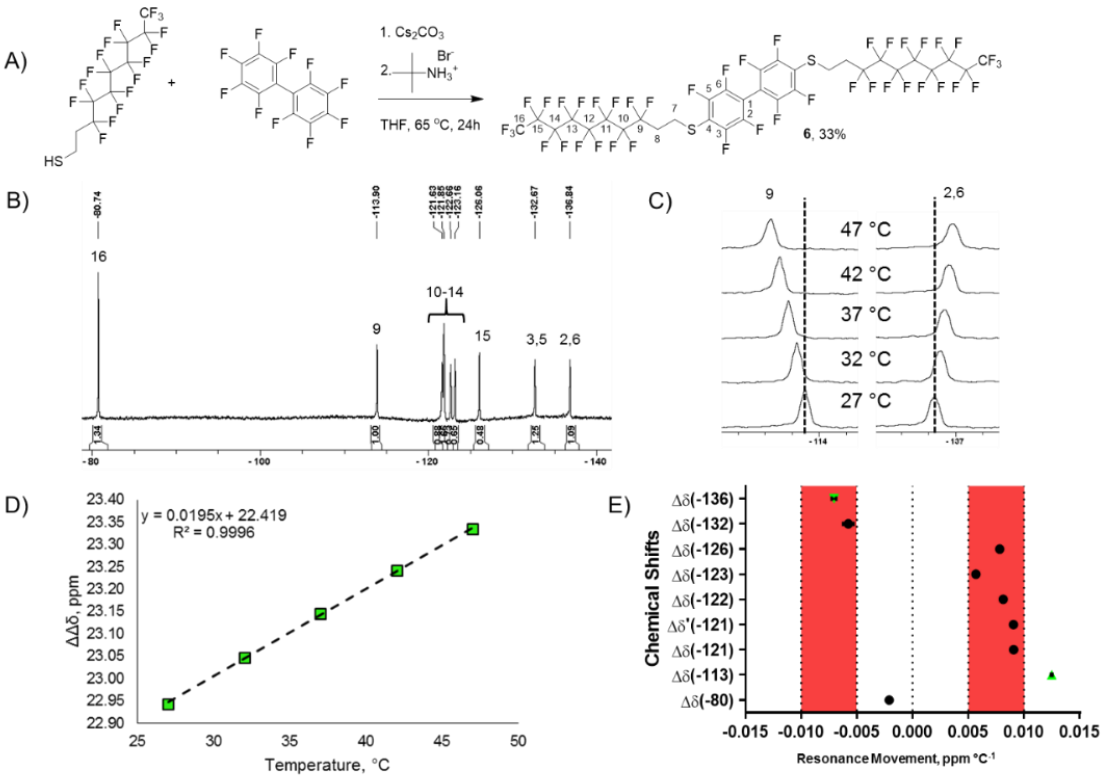


**Figure 3.4.** Structure and temperature response of **6**. (A) Synthesis and structure of **6**. (B) $^{19}$F NMR spectrum of **6** in $CDCl_3$. Assignments were derived from analogous structures in literature.[33,38,39] (C) $^{19}$F spectra of most temperature responsive chemical shifts (ppm). (D) Temperature response curve of **6** with $\Delta\Delta\delta(T) = 19.5 \times 10^{-3} \pm 0.2 \times 10^{-3}$ ppm °C$^{-1}$ (n = 3, mean ± SEM). Compound **6** has a ~ 2-fold increase in responsiveness compared to the PRF. (E) Movement of individual resonances over 20 °C; several of the shifts are in the optimal region (± 5 to ± 10 × $10^{-3}$ ppm °C$^{-1}$) indicating most of the resonance combinations are above 10 × $10^{-3}$ ppm °C. The most responsive combinations are indicated as green triangles (down for negative movement, and up for positive movement). Error bars are negligible from 3 replicate measurements.

The long-term goal of this work is to incorporate the temperature-sensitive fluorocarbons into ultraporous mesostructured silica nanoparticles (UMNs).[27,88] Compound **6** was a white solid after purification. Solid PFCs have yet to be loaded into UMNs; however, diffuse loading and further sequestering solid particles inside of the nanoparticles are plausible.[98–100] Additionally, derivative designs, by shortening the fluorinated tail, or

using different rigid structures may lead to a fluorocarbon liquid. The guidelines from this design scheme can be applied to make novel sensors that can append to the nanoparticles either covalently or electrostatically. Alternatively, the rational basis for design could be expanded to discover what parameters are useful in tuning synthetic routes to make fluorinated molecules with predictable and convenient states of matter. If these sensors are analogous to PFTBA, then chloroform may have slightly enhanced the thermal response of our compounds. Further detailed investigations in solvent effects and physical state of our compounds need careful consideration for future biomedical applications.

## 3.4 Conclusions

This work described the rational design of temperature-responsive fluorinated molecules to act as temperature sensors using NMR. To address the large chemical space challenge, the synthetic possibilities were reduced and focused by incorporation of experimentally analyzed sensors and computationally driven hypotheses of the physiochemical properties that are crucial to the development of these fluorine-based temperature sensors. The best temperature sensor, **6**, was discovered after supporting several hypotheses. The theory behind a "good" sensor is based on a molecule containing at least: two chemically different fluorine groups on the same molecule; fluorine groups that are not proximally close to each other in space; a freely moving fluorine group vs a fluorine group near a rigid chemical structure; opposing responsiveness in fluorine groups that lead to an individual response $\geq \pm 5 \times 10^{-3}$ ppm $°C^{-1}$. Further investigation on the effects on heteroatoms are warranted and may improve the response of the sensors further. Additionally, investigation into different rigid chemical structures may improve thermal responsiveness.

While measurements were done in $CDCl_3$, a nearly 2-fold increase in responsiveness to temperature based on the state-of-the-art MRI probes makes **6** a new candidate for MRI temperature mapping and subsequent *in vivo* studies, either incorporated into UMNs or a different biological vehicle (e.g., liposomes, emulsions). The capability of taking more

accurate and sensitive temperature measurements will lead to better understanding of chemical biological interactions, improved monitoring of heating systems, and more reliable diagnostics for evaluation of medical interventions.

# Chapter 4

**Synopsis**

The solid state and fluxional behaviors in solution of complexes $L^2$AlOBn and $L^7$AlOBn (Bn = benzyl) supported by an analog of salen incorporating indolide arms connected via their 2- and 7-positions were defined by experiment and theory. The complexes catalyze the stereoselective conversion of *rac*-lactide (*rac*-LA) to isotactically enriched polylactide. A key aspect of the stereocontrol was examined through study of the initiation reactions via NMR spectroscopy, X-ray crystal structures of the ring-opened products, and theory. The results include the first unambiguous structural definition of stereocontrol in ring-opening of LA by a metal–alkoxide complex and the finding that definition of the stereochemistry of initiation by the studied system is governed thermodynamically rather than kinetically. Theoretical study of the propagation showed a reversal of the rate-determining step caused by catalyst-chain end interactions, but the polymerization remained stereoselective, albeit through a different mechanism.

## 4.1 Introduction

An important goal of contemporary research is to develop catalysts capable of polymerizing bioderived monomers with high selectivity, good molecular weight (MW) control, fast and/or convenient rates, and sufficient robustness to operate under potentially useful and/or industrially relevant conditions.[101–104] The stereoselective ring-opening transesterification polymerization (ROTEP) of racemic lactide (*rac*-LA) to yield polylactide (PLA) has been particularly well-studied [105] because of the utility of PLA in a wide range of applications and the importance of PLA tacticity in determining its properties.[106] Isotactic strands of Poly D-Lactic acid (PDLA) and Poly L-Lactic acid (PLLA) form stable crystalline structures (see figure 4.1) with high $T_m$, which are important for high-temperature applications.[107]

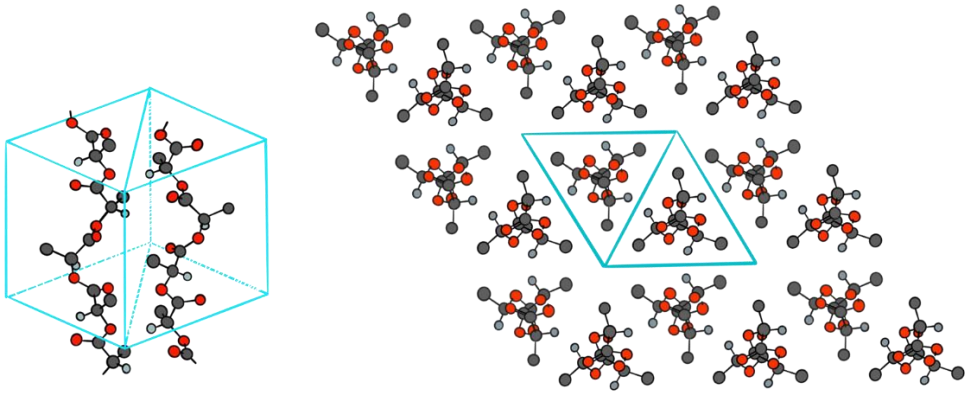

**Figure 4.1.** Structure of isotactic stereocomplex formed between PLLA and PDLA. Figure adapted from ref 106.

Among the plethora of catalysts examined for this purpose, (salen)AlOR complexes (Figure 4.2) have garnered considerable attention due to their high MW control, rates convenient for NMR spectroscopic monitoring, and ease of synthesis of ligand derivatives, with several having engendered high stereoselectivity in polymerizations of *rac*-LA.[108–123] While this previous work has provided considerable insight, detailed

molecular-level mechanistic understanding is limited, and further work is needed to address such issues as the impact of supporting ligand structural features on polymerization behavior, the specific molecular basis for observed stereocontrol using both chiral and achiral supporting ligands, and the precise structures of key intermediates. Such understanding is of potential utility for future catalyst design.

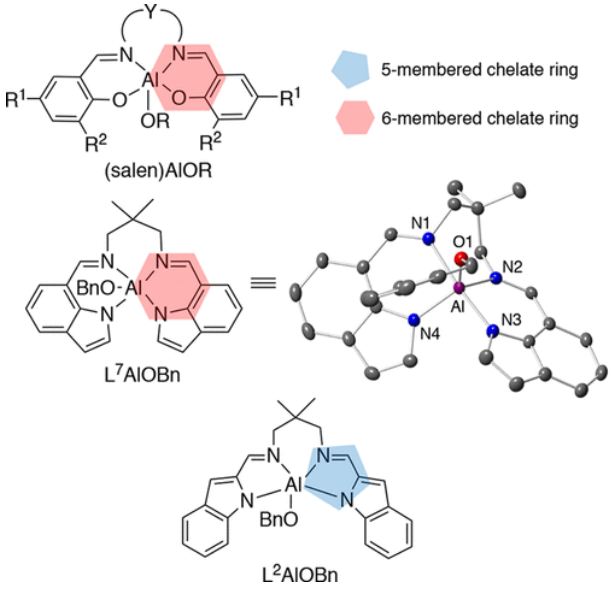


**Figure 4.2.** Complexes used as ROTEP catalysts. X-ray crystal structure reported in ref 123 (Λ isomer shown).

Recently, we reported predictions by theory of cyclic ester polymerization efficiency for a series of aluminum catalysts, including the complex $L^7$AlOBn supported by a novel analog of salen incorporating indolide arms connected at their 7-position (Figure 4.2). [124] Subsequent synthesis of $L^7$AlOBn and studies of the kinetics of ROTEP of ε-caprolactone by the complex confirmed the prediction, validating the theoretical approach toward catalyst design. In that work, the X-ray crystal structure of the complex revealed a chiral structure with the ligand twisted such that the indolide rings are inequivalent. NMR spectroscopy showed the rings to be equivalent, however, suggesting operation of a fluxional process in solution. In view of these structural attributes and analogies to efficacious (salen)AlOR systems (for example, (TBSsalen)AlOR, with Y =

$CH_2CMe_2CH_2$, $R^1$ = H, $R^2$ = $tBuMe_2Si$), [120] we hypothesized that $L^7$AlOBn might exert stereocontrol in ROTEP of *rac*-LA.

One of the challenges in the rational design of catalysts for stereoselective ROTEP of *rac*-LA is the various mechanistic degrees of freedom that might lead to very different relative arrangements of the intermediates and transition states of the substrate with respect to the catalyst[14,15]. Such a diversity of viable ROTEP mechanisms makes *a priori* prediction of the outcome of specific changes in the catalyst structure on stereoselectivity difficult, because changes that might lead to a favorable outcome in one mechanistic path might have unwanted effects on other paths. The systems investigated in this study were found to have many low-lying transition states. As such, we attempted to do a thorough search of all the viable pathways, to gain a better understanding of this system. The findings of this study, however, are potentially applicable to all (salen)AlOR and possibly other catalysts for ROTEP of Lactide, as well as other cyclic esters, as these systems can have structural features in common, that may lead to a similarly diverse array of successful pathways for the reaction to occur.

In the first part of this study, we describe evaluation of the fluxionality of $L^7$AlOBn in solution by variable temperature (VT) NMR spectroscopy, theory, and studies of the ROTEP of *rac*-LA by the complex. Also, we compare its structural features and reactivity to an analogous complex $L^2$AlOBn in which the indolide rings are connected at the 2- rather than the 7-position to yield 5- instead of 6-membered chelate rings (Figure 4.1). [125] As this work was being completed, the synthesis and use of $L^2$AlOiPr in stereoselective polymerizations of LA, as well as the identification of a ring-opened LA complex, were reported, but the rationale for selectivity in ROTEP was not studied.[126] In our work, through synergistic theoretical and experimental approaches, the effects of the supporting ligand differences on the ROTEP behavior of $L^2$AlOBn and $L^7$AlOBn were evaluated, with a specific emphasis on understanding the basis of the observed stereocontrol in the first ring-opening step (initiation) of *rac*-LA. Among our findings are precise structural determinations by X-ray crystallography of the initial products of ring-opening of *rac*-LA by metal-alkoxide complexes, revealing the stereochemistry of

initiation. In addition, we evaluated said initiation by two-dimensional NMR spectroscopy and theory, leading to new insights into the basis for stereoselectivity and a key finding of thermodynamic rather than kinetic governance of stereocontrol. These studies, placed in perspective through comparisons to (salen)AlOR systems and, more broadly, to many other catalysts, [105,108] provide deep mechanistic understanding of ROTEP reactions of importance for sustainable polymer synthesis.

In the next part of the study, we turned our focus on the propagation steps, in the $L^7$AlOBn catalyst, as it was found to be the more enantioselective catalyst of the two, to understand the extent to which the chain-end mechanism (CEM) affects the ROTEP stereoselectivity.

## 4.2 Structural variables

There are four major variables that determine the enantioselectivity of this reaction. Catalyst chirality, the chirality of the incoming monomer (L or D-Lactide.), the chirality of the chain-end monomer, the pro-chirality of the initial nucleophilic attack (*re* or *si* face of the incoming Lactide unit), and the coordination mode of the substrate to the catalyst (whether the Alkoxy oxygen is coordinated in the axial or equatorial position in the initial nucleophilic attack). The prochirality refers to the face upon which the first nucleophilic attack occurs. Thus, with the consideration of all the symmetries involved, there are a total of 16 pathways to consider. These mechanistic degrees of freedom exist for many ROTEP catalysts, and great care must be taken to not rule out any of them, especially if there are no a priori reasons to do so.

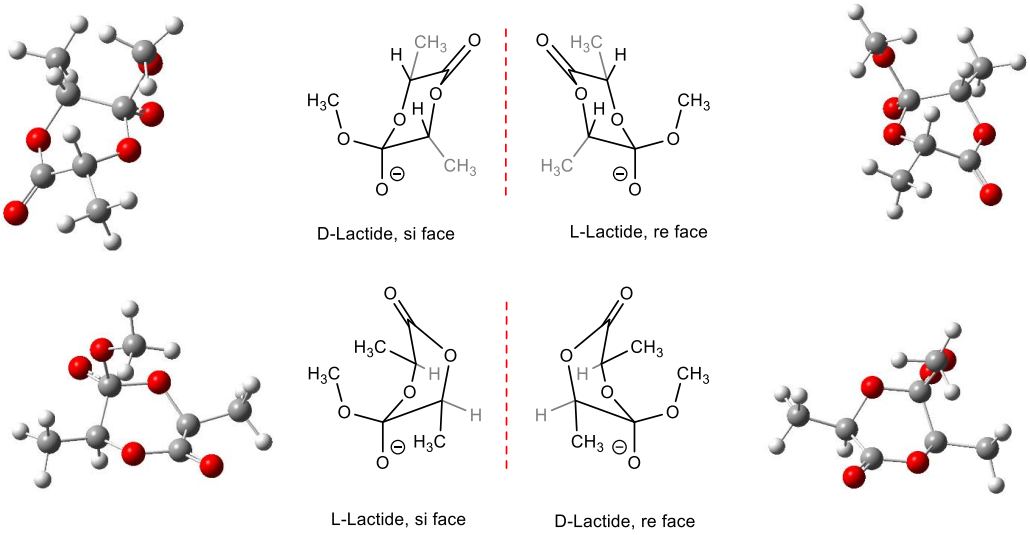


**Figure 4.3**. Possible structures of tetrahedral intermediates formed by alkoxide insertion of L and D-Lactide

In the absence of the catalyst, the L and D-Lactide can react with the nucleophilic alkoxide to form four distinct tetrahedral intermediates. These intermediates, once formed, cannot interconvert without covalent bond dissociation. The tetrahedral intermediate itself can bind to the catalyst in different coordination modes that can, in principle, interconvert between one another. The coordination modes where the Lactyl and carbonyl Oxygen atoms are coordinated to the catalyst are the ones that can lead to the opening of the Lactide ring (TS2), and the ones where the alkoxy and carbonyl Oxygen atoms are bound to the catalyst are the ones that follow the initial nucleophilic attack (TS1).

Because the different coordination modes can interconvert with barriers that are lower than TS1 or TS2, for the purpose of predicting the kinetics of the reaction, all pathways that differ only in coordination mode (***axial*** vs. ***equatorial***) must be considered together see figure 4.4). However, to understand the structural factors and that determine the selectivity of the reaction, it's required to analyze these pathways separately.

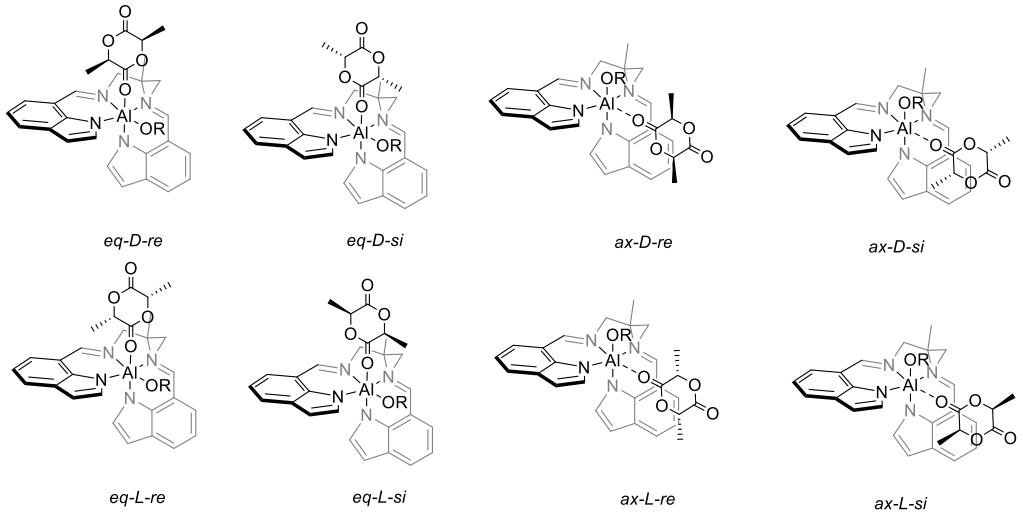


**Figure 4.4**. Possible coordination modes of the tetrahedral intermediate

## 4.2 Initiation Study

### 4.2.1 Experimental Study

#### 4.2.1.1 Synthesis and Characterization of Complexes

The complex $L^7$AlOBn was prepared as described previously [124] and the synthesis of $L^2$AlOBn was performed similarly (Scheme 4.1).

**Scheme 4.1.** Syntheses of $L^2$AlEt and $L^2$AlOBn

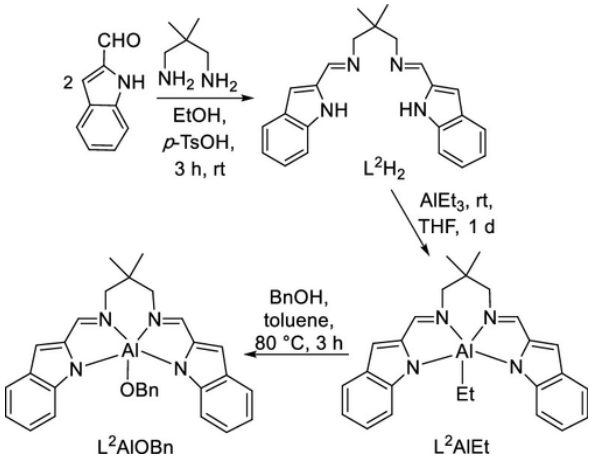


Each of the complexes crystallizes as a mixture of enantiomers; for the complexes of $(L^2)^{2-}$ and $(L^7)^{2-}$, the ligand in each stereoisomer is twisted so that the indolide rings are

inequivalent, with the enantiomers differentiated by the indolide ring orientation (labeled as Δ or Λ as indicated in scheme 4.1).

[126] Thus, condensation of indole-2-carboxaldehyde and 2,2-dimethyl-1,3-propanediamine yielded $L^2H_2$ (56%, Figure S1 in reference 28), which upon metalation with $AlEt_3$ afforded $L^2AlEt$ (98%); the characterization data for this complex matched that reported elsewhere.[126] Subsequent reaction with BnOH yielded $L^2AlOBn$ (80%). Both $L^2AlOBn$ and $L^7AlOBn$ were characterized by CHN analysis and NMR spectroscopy, as well as X-ray crystallography, here for the former (Figures 4.5, S2, and S3 in reference 28). The structure features distorted trigonal bipyramidal geometry, with a $\tau_5$ value [127] of 0.62 (theory: 0.68) similar to that reported for $L^2AlOiPr$ (0.65). [126] By comparison, the values for $L^7AlOBn$ [124] and (TBSsalen)AlOBn [120] are 0.87 and 0.83, respectively, indicating geometries closer to ideal trigonal bipyramidal for these complexes.

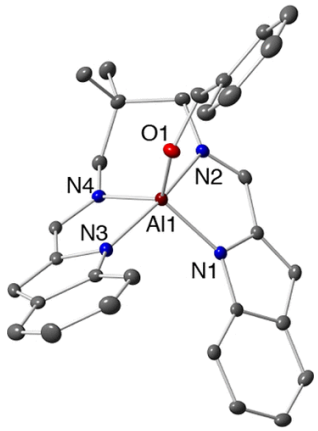


**Figure 4.5.** Representation of the X-ray crystal structure of $L^2AlOBn$, showing one enantiomer (Δ) of the two present in the unit cell as 50% ellipsoids with H atoms omitted for clarity. Selected bond distances (Å) and angles (degrees): Al1–O1, 1.722(3); Al1–N1, 1.939(0); Al1–N2, 2.003(9); Al1–N3, 2.069(8); Al1–N4, 1.918(5); N2–Al1–N3, 81.915(0); N2–Al1–N4, 113.075(1); N2–Al–O1, 126.132(1); N4–Al1–O1, 110.979(8); N4–Al1–N3, 81.751(9); N1–Al1–O1, 96.337(2); N3–Al1–O1, 96.506(9); N4–Al1–N1, 101.061(2); N2–Al1–N1, 81.750(5); N3–Al1–N1, 163.179(9).

**Scheme 4.2.** Enantiomers of Complexes $L^7$AlOR and $L^2$AlOR (R = Bn), with Labeling of Chirality Indicated

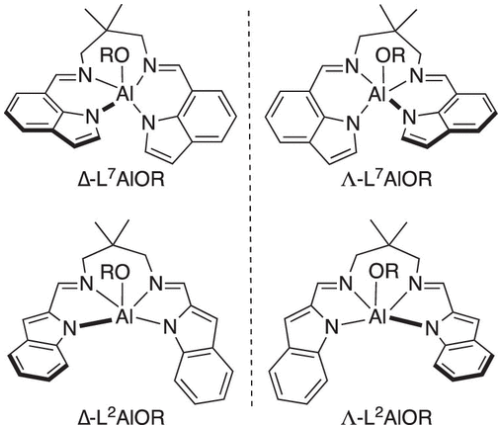


The inequivalence of the indolide rings in the X-ray structures of $L^2$AlOBn and $L^7$AlOBn is not reflected in their $^1$H NMR spectra at 300 K, as only one set of peaks for the indolide and imine hydrogen atoms is observed (Figure 4.6 and S3 in reference 28). This observation suggests a fluxional process that interconverts the indolide ring environments and is sufficiently rapid on the NMR time scale to result in averaging of the associated peaks. This hypothesis was confirmed through VT-NMR experiments for both complexes (Figure 4.6, S11 and S13 in reference 28). Illustrative peaks for the hydrogen atoms on the imine and the 6-position of the indolide rings for $L^7$ and 7-position for $L^2$ undergo reversible decoalescence to yield a peak pattern indicative of inequivalent indolide rings upon lowering the temperature. Spectral fitting and Eyring analyses (Figures S15 and S16 and Table S1 in reference 28) yielded $\Delta G^{\ddagger}_{298\,K}$ = 10.2 kcal mol$^{-1}$ and 10.7 kcal mol$^{-1}$ for the processes for $L^7$AlOBn and $L^2$AlOBn, respectively. As similar fluxionality had been proposed for (salen)AlOR complexes (Figure 4.2), [120] we prepared (TBSsalen)AlOBn according to the literature procedure [120] and through VT-NMR studies determined $\Delta G^{\ddagger}_{298\,K}$, which was similar (9.0 kcal mol$^{-1}$).

Hypothesizing that the fluxionality observed in solution derived from interconversion of the Δ and Λ enantiomers of the complexes (Figure 4.6), we performed DFT calculations to interrogate the process. After a thorough conformational search to find all the low-

lying conformers of $L^2$AlOBn and $L^7$AlOBn, the barrier for chirality inversion for the complexes was then found through optimizing the transition state structures. The barriers found for the complexes were similar ($L^7$AlOBn = 9.9 kcal $mol^{-1}$; $L^2$AlOBn = 11.6 kcal $mol^{-1}$) and agreed closely with those found experimentally (10.2 and 10.7 kcal $mol^{-1}$, respectively). For $L^7$AlOBn, the lowest energy conformer has a twist-boat-like conformation in the six-membered metallacycle formed by the Al atom and the ligand backbone, whereas in the transition state, the metallacycle has a more symmetric chair-like conformation.

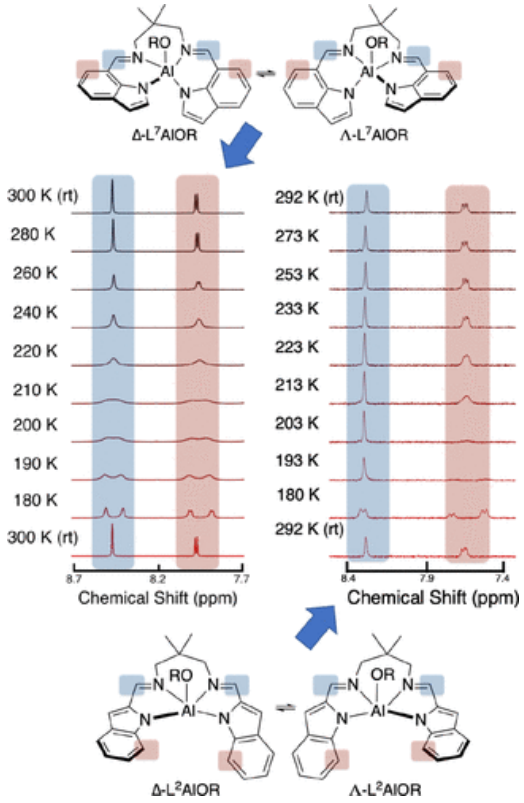


**Figure 4.6.** Selected VT-NMR ($^1$H) data for $L^7$AlOBn (left) and $L^2$AlOBn (right) with proposed assignments. The bottom spectra were collected after returning to rt to show reversibility. Full spectra are shown in Figures S11 and S13 in reference 28.

As a result, the fluxional process happens in two steps, involving conformational change of the metallacycle followed by movement of the rings into the more symmetric transition state (Figure 4.7). For $L^2$AlOBn, the metallacycle is already in a chair-like

conformation, so the chirality flipping happens in one step. Finally, we note parenthetically that the catalyst fluxionality for these systems resembles that proposed for Ti complexes that catalyze syndiospecific propene polymerization. [128,129]

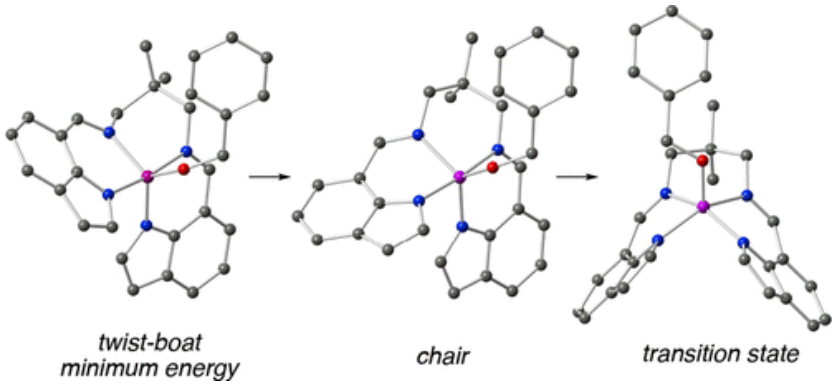


**Figure 4.7.** Calculated structures for the fluxional process that interconverts Δ and Λ enantiomers of $L^7$AlOBn, depicting the lowest energy structure for the Δ enantiomer, the next highest energy (+ 2.3 kcal $mol^{-1}$) structure for the chair conformation of the metallacycle, and the "symmetric" transition state structure.

### 4.2.1.2 Polymerization Behavior

We examined the catalytic polymerization of *rac*-LA by $L^7$AlOBn and $L^2$AlOBn under a variety of conditions, ranging from 35 °C in $CD_2Cl_2$ (300:1 monomer:catalyst ratio, except in the case of toluene) to neat reactions in the melt (135–180 °C). As indicated in Table 4.1, the reactions proceeded at rates that depended on the conditions used to yield PLA characterized by low $Đ$ values (measured by size exclusion chromatography using light scattering detection) and $P_m$ values (measured via analysis of homonuclear decoupled $^1$H NMR data, examples in Figures S17–S19 and Table S2 in reference 28). These latter values varied from 0.53 (low isotacticity, entries 9 and 14) to 0.80 (high isotacticity, entries 1 and 2), depending on the supporting ligand and the conditions. The results for polymerizations by $L^2$AlOBn are similar to those reported recently. [126] Differential scanning calorimetry data revealed $T_m$ features in only three

cases (entries 1–3, Table 4.1, examples shown in Figures S20–S23 in reference 28), indicating attainment of isotactic segment lengths sufficient for crystallization in these instances. Previously reported data for (TBSsalen)AlOR [120] are shown for comparison (entries 15, 17, 19, Table 4.1), along with data for the same complex that we prepared and tested independently (entries 16, 18, 20, Table 4.1) that are in good agreement. In general, the level of stereocontrol exhibited by (TBSsalen)AlOR was higher than for $L^7$AlOBn and $L^2$AlOBn. The stereoselectivity exhibited by the complex of ($L^7$) is slightly higher than that supported by ($L^2$), which exhibits faster rates than the former. As expected, comparison of the kinetics of polymerizations of L-LA and rac-LA by both L7 AlOBn and L2 AlOBn showed a higher rate for the single enantiomer (i.e., L-LA; Figure S4 in reference 28).

**Table 4.1.** Data for Polymerizations of *rac*-LA by the Indicated Complexes

| | complex | temp. (°C) | LA:cat | time | convn[a] (%) | $M_n$ (kDa)[b] | $Đ$[b] | $P_m$[c] | $T_m$ (°C)[d] |
|---|---|---|---|---|---|---|---|---|---|
| 1 | $L^7$AlOBn | 35 ($CD_2Cl_2$) | 300 | 14 d | 99 | 85 | 1.06 | 0.80 | 163 |
| 2 | | 55 (THF-$d_8$) | 300 | 4 d | 99 | 36 | 1.03 | 0.80 | 155 |
| 3 | | 70 (tol-$d_8$) | 100 | 3 d | 98 | 24 | 1.20 | 0.74 | 150 |
| 4 | | 135 | 300 | 30 min | 96 | 40 | 1.11 | 0.64 | e |
| 5 | | 150 | 300 | 25 min | 78 | 85 | 1.22 | 0.63 | e |
| 6 | | 165 | 300 | 20 min | 91 | 29 | 1.16 | 0.66 | e |
| 7 | | 180 | 300 | 15 min | 93 | 54 | 1.44 | 0.68 | e |
| 8 | $L^2$AlOBn | 35 ($CD_2Cl_2$) | 300 | 6 d | 95 | 35 | 1.08 | 0.67 | e |
| 9 | | 55 (THF-$d_8$) | 300 | 2 d | 99 | 42 | 1.17 | 0.53 | e |
| 10 | | 70 (tol-$d_8$) | 100 | 3 d | 98 | 24 | 1.31 | 0.67 | e |
| 11 | | 135 | 300 | 30 min | 93 | 34 | 1.74 | 0.58 | e |
| 12 | | 150 | 300 | 25 min | 94 | 60 | 1.85 | 0.62 | e |
| 13 | | 165 | 300 | 20 min | 79 | 115 | 1.31 | 0.55 | *e* |
| 14 | | 180 | 300 | 15 min | 99 | 64 | 1.23 | 0.53 | e |
| 15 | (TBSsalen)AlOR[g] | 70 (tol-$d_8$) | 100 | 14 h | 96 | 22[f] | 1.07[f] | 0.98 | 209 |
| 16 | | | | | *96* | 25 | 1.07 | 0.92 | 207 |

| complex | temp. (°C) | LA:cat | time | convn[a] (%) | $M_n$ (kDa)[b] | $Đ$[b] | $P_m$[c] | $T_m$ (°C)[d] |
|---|---|---|---|---|---|---|---|---|
| 17 | 130 | 300 | 30 min | 73 | 44[f] | 1.08[f] | 0.92 | 189 |
| 18 | | | | *79* | 53 | 1.15 | 0.89 | 187 |
| 19 | 180 | 300 | 20 min | 91 | 60[f] | 1.13[+] | 0.84 | 176 |
| 20 | | | | *90* | 59 | 1.34 | 0.85 | 179 |

[a] Determined by $^1$H NMR spectroscopy. [b] Except as noted, these values were determined by SEC using light scattering detection with THF eluent. Theoretical values are 44 kDa for 300 equiv of LA and 15 kDa for 100 equiv of LA. [c] Determined by homonuclear decoupled $^1$H NMR spectroscopy (see SI). [d] Determined by DSC. [e] No feature corresponding to a $T_m$ value was observed. [f] Values determined by SEC using a refranctive index detector and polystyrene standards with $CHCl_3$ eluent. [g] Previously reported values (ref 109 with values we independently determined below in italics).

#### 4.2.1.3 Experimental Insights into Stereocontrol in Initiation

In order to begin to understand the basis for stereocontrol for *rac*-LA polymerization by L$^7$AlOBn and L$^2$AlOBn, we examined stoichiometric reactions of *rac*-, L(*S,S*)-, and D(*R,R*)-LA with the complexes, as well as with (TBSsalen)AlOBn for comparison. In the experiments, a solution of LA (1 equiv) in $CD_2Cl_2$ or $CDCl_3$ was added to a solution of the complex in the same solvent (6.5 mM) at room temperature and a $^1$H NMR spectrum was immediately measured. The spectra showed complete consumption of starting materials and the appearance of predominantly one species with new peaks that we assign to the single ring-opened products L$^2$- or L$^7$Al(oLAOBn) (where oLAOBn refers to the ring-opened LA terminated by -OBn; Figures 4.8, S5–S8 in reference 28) or (TBSsalen)Al(oLAOBn) (Figures S9 and S10 in reference 28), as reported previously. [120] Importantly, the spectra for the products of the reactions with *rac*-, L(*S,S*)-, and D(*R,R*)-LA are nearly identical. The peak patterns are consistent with selective formation of either a 1:1 mixture of two symmetric complexes (i.e., indolide or phenolate rings are equivalent for each, which would only be possible if peaks due to diastereomeric species were averaged as a result of fluxionality) or a single asymmetric complex (with inequivalent rings). Thus, for example, the spectra of L$^7$Al(oLAOBn)

exhibit two peaks (8.37 and 8.45 ppm) integrating equally for the imine protons; these peaks are almost overlapping for the case of $L^2$Al(oLAOBn).

To interpret the results from NMR spectroscopy, we present all the possible structures for the products of ring-opening of D(*R*,*R*)- and L(*S*,*S*)-LA by the two interconverting stereoisomers of $L^7$AlOBn in Scheme 4.3. Thus, each stereoisomer Δ- or Λ-$L^7$AlOBn can react with either L(*S*,*S*)-LA or D(*R*,*R*)-LA. The result is four possible stereoisomers, classified as two diastereomeric pairs of enantiomers: Δ-L(*S*,*S*)/Λ-D(*R*,*R*) and Δ-D(*R*,*R*)/Λ-L(*S*,*S*). These are drawn with the opened LA chain binding in bidentate fashion via alkoxide and carbonyl O atoms, which is what we observed via X-ray crystallography (*vide infra*). Each pair of enantiomers (i.e., each diastereomeric set) would be expected to give rise to a spectrum featuring inequivalent indolide rings and one set of peaks associated with the opened LA chain.

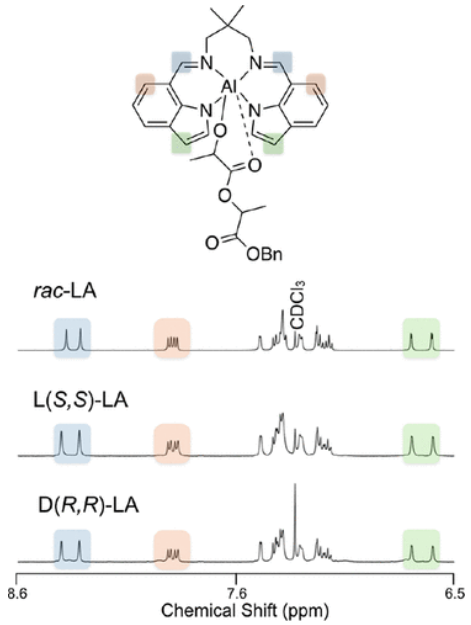


**Figure 4.8.** Selected portion of the $^1$H NMR spectra of the products of the reactions of (top) *rac*-LA, (middle) L(*S*,*S*)-LA, or (bottom) D(*R*,*R*)-LA with $L^7$AlOBn, with the indicated assignments. Full spectra as well as data for the same reactions of $L^2$AlOBn are provided as Figures S5–S8 in reference 28.

The observed spectrum for the reaction with *rac*-LA (e.g., the pairs of peaks of equal intensity shown in Figure 4.8) is consistent with highly stereoselective formation of *one* of the diastereomeric sets (i.e., one pair of enantiomers). The observation of the same spectrum in reactions of pure L(*S*,*S*)- or D(*R*,*R*)-LA is explained by selective formation of one diastereomer (i.e., for the reaction with L(*S*,*S*)-LA, either Δ-L(*S*,*S*) or Λ-L(*S*,*S*)). The NMR data are not sufficient to distinguish which set of enantiomers (for the reaction with *rac*-LA) or which particular diastereomer (for the reactions with pure L(*S*,*S*)- or D(*R*,*R*)-LA) is formed. The alternative explanation that the peaks observed are due to a rapidly interconverting mixture of *both* diastereomers would predict line broadening or decoalescence of these peaks upon lowering the temperature, but this was not observed (to −88 °C, Figures S12 and S14 in reference 28). Finally, we note that similar considerations apply to the (TBSsalen)Al system.

**Scheme 4.3.** Possible Products $L^7$Al(oLAOBn) Resulting from the Reaction of the Interconverting Stereoisomers $L^7$AlOBn (in box) with L(*S*,*S*)- and D(*R*,*R*)-LA, Labeled According to the Configuration at Al (Δ vs. Λ) and LA (D(*R*,*R*) vs. L(*S*,*S*))[a]

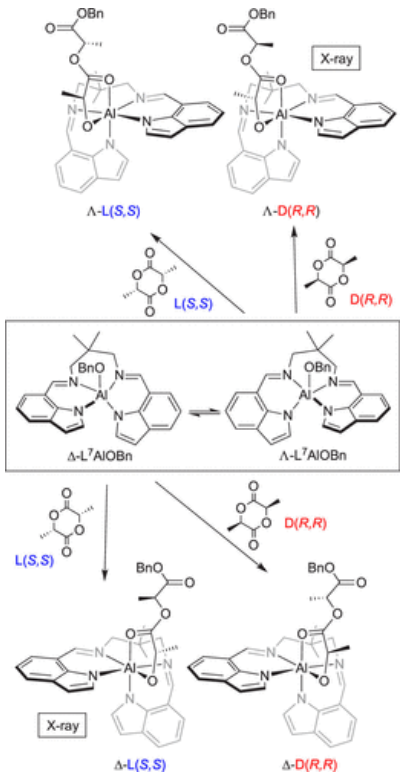

[a]The isomers labeled "X-ray" are the ones identified by X-ray crystallography.

By layering pentane on $CD_2Cl_2$ solutions of the products $L^2$- or $L^7$Al(oLAOBn) formed upon reaction of $L^2$AlOBn and $L^7$AlOBn with *rac*-LA and storing at −30 °C, we obtained crystals suitable for X-ray diffraction (Figure 4.9). In both cases, the ring-opened products crystallized as a pair of enantiomers comprising a *single* diastereomer, consistent with our interpretation of the $^1$H NMR spectra of the product solutions. These enantiomers were identified as the complexes labeled Δ-L(*S*,*S*) and Λ-D(*R*,*R*) in Scheme 4.3, with only the former enantiomer for each case shown in Figure 4.9. In both structures (a and b), the Al–O1 (alkoxide) distance (1.804(2) Å and 1.807(3) Å, respectively) is shorter than all other metal–ligand bonds (range 2.094(7)–1.932(3) Å). The Al geometries are octahedral, with the ring-opened LA bound in bidentate fashion featuring Al–O2 distances of 2.094(7) Å and 2.1784(17) Å for (a) and (b), respectively. These X-ray structures represent rare examples of high quality structural determinations for ring-opened LA bound to a metal complex. [130,131] Such species had been previously identified by spectroscopy[114–117,132] and modeled in structures of methyl lactate complexes.[120,133] Redissolution of the crystals used for the X-ray structure determinations yielded $^1$H NMR spectra identical to those obtained for the initial product solutions. These results are consistent with the NMR spectral features arising from the Δ-L(*S*,*S*) and Λ-D(*R*,*R*) enantiomers (the single diastereomer) observed by X-ray crystallography. Nonetheless, it is also possible that the diastereomer observed by NMR spectroscopy participates in an equilibrium with a small (essentially unobservable) amount of the other diastereomer (*vide infra*), and that this minor diastereomer preferentially crystallizes (and reverts to the major diastereomer upon redissolution). While we view this alternative possibility as unlikely (preferential crystallization of an equilibrating minor diastereomer for *both* $(L^2)^{2-}$ and $(L^7)^{2-}$ systems), it cannot be ruled out by the available experimental data.

The above considerations raise the question: Is the initiation reaction selectivity based on kinetic or thermodynamic control? That is, does the initiation stereoselectivity result from differences in the barriers for ring-opening (as postulated previously on the basis of

theory for other catalysts)[134] or from differences in the stabilities of the products that are rapidly equilibrating? Such equilibration might involve rapid intermolecular exchange of alkoxide ligands (e.g., between Δ-L(*S*,*S*) and Δ-D(*R*,*R*) isomers), decoordination of the carbonyl group and racemization at Al as observed for the fluxionality of LAlOBn (e.g., between Δ-L(*S*,*S*) and Λ-L(*S*,*S*) isomers), or both (Figure 4.10).

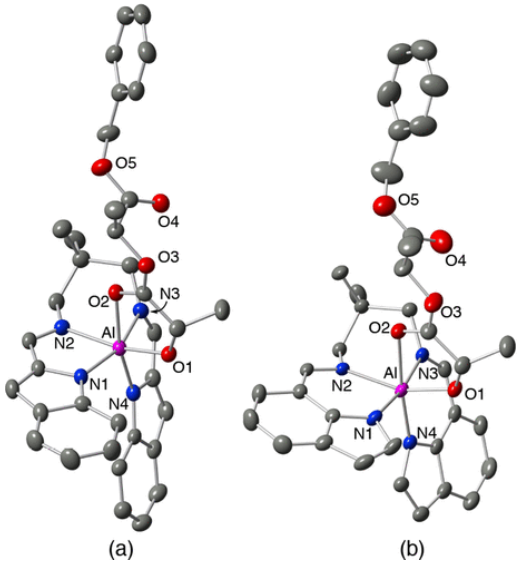


**Figure 4.9.** Representations of the X-ray crystal structures of the ring-opened products (a) $L^2$Al(oLAOBn) and (b) $L^7$Al(oLAOBn), resulting from the reactions of $L^2$AlOBn and $L^7$AlOBn, respectively, with 1 equiv of *rac*-LA. Only a single enantiomer for each structure is shown (Δ-l(*S*,*S*); the other Λ-D(*R*,*R*) enantiomer is also present in the unit cell), with all atoms presented as 50% ellipsoids and hydrogen atoms omitted for clarity. Selected bond distances (Å) and angles (deg): (a) Al1–O1, 1.804(2); Al1–N1, 1.932(3); Al1–N2, 2.058(5); Al1–N3, 2.054(1); Al1–N4, 1.945(0); N3–Al1–N1, 160.070(6); N3–Al1–O1, 99.876(5); N3–Al1–O2, 88.536(1); N3–Al1–N2, 79.984(0); N3–Al1–N4, 80.830(1); N2–Al1–N4, 100.140(0); O2–Al1–O1, 81.204(6); N2–Al1–O2, 84.416(7); N4–Al1–O1, 94.002(8); N4–Al1–O2, 167.451(7); N1–Al1–N4, 102.280(5), N1–Al1–N2, 80.091(8); N1–Al1–O2, 89.986(1); N1–Al1–O1, 99.531(4); (b) Al1–O1, 1.807(3); Al1–N1, 1.9475(18); Al1–N2, 2.0647(16); Al1–N3, 2.0779(18); Al1–N4, 1.9344(17); N3–Al–N1, 171.24(7); N3–Al1–O1, 90.80(8); N3–Al1–O2, 89.33(13); N3–Al1–N2, 82.69(6); N3–Al1–N4, 89.49(7); N2–Al1–N4, 103.71(7); O2–Al1–

O1, 79.47(11); N2–Al1–O2, 81.07(9); N4–Al1–O1, 95.56(9); N4–Al1–O2, 174.88(12); N1–Al1–N4, 94.99(7); N1–Al1–N2, 88.93(7); N1–Al1–O2, 86.84(14); N1–Al1–O1, 96.24(9).

To test for these possibilities, we performed a set of experiments using NMR exchange spectroscopy (EXSY).[135] The experiments involved acquisition of data on solutions of (a) $L^7$Al(oLAOBn) and $L^2$Al(oLAOBn) prepared from reactions of the respective benzyloxide complexes with *rac*-LA, (b) $L^7$Al(oLAOBn) prepared from reaction of $L^7$AlOBn with L(*S*,*S*)-LA, (c) a 1:1 mixture of $L^7$Al(oLAOBn) and $L^2$Al(oLAOBn) prepared by mixing solutions resulting from reaction of the respective benzyloxide complexes with *rac*-LA, and (d) a 1:1 mixture of $L^7$Al(oLAOBn) and (TBSsalen)AlOBn prepared by mixing solutions resulting from reaction of the respective benzyloxide complexes with *rac*-LA.

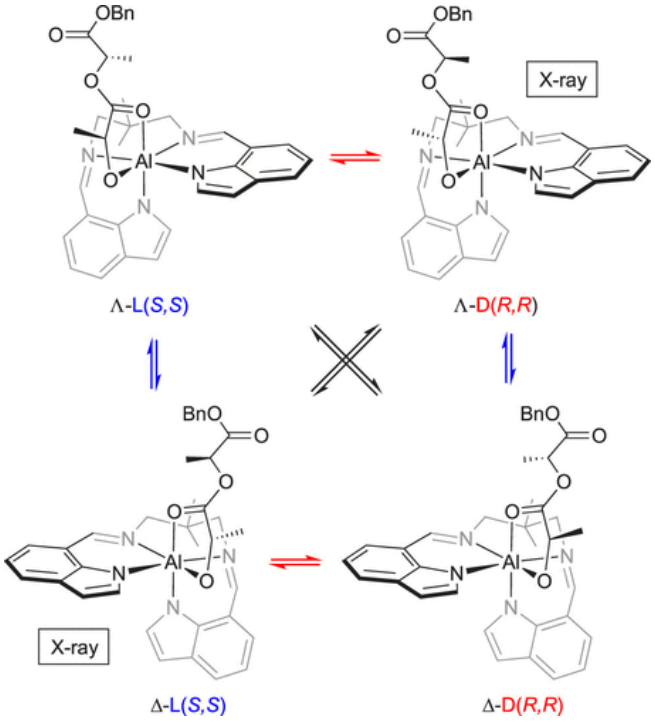

**Figure 4.10.** Illustration of possible interconversions of stereoisomers $L^7Al$(oLAOBn). The red arrows indicate processes involving intermolecular exchange of LA enantiomers, blue arrows correspond to racemization at Al (e.g., via carbonyl decoordination, isomerization, and recoordination), and black arrows correspond to both.

The results and detailed interpretations are described in the Supporting Information (Figures S28–S34 in reference 28); here, we present the primary conclusions drawn. From part a, we identified minor peaks in the NMR spectra that we assign to small amounts of the minor diastereomer, and clear evidence of exchange between the ring-opened alkoxide chains indicating interconversion between the major and minor diastereomers. By integration, the ratio ($K_{eq}$) of the equilibrating major:minor isomers for $L^7Al$(oLAOBn) is ~ 9:1, corresponding to $\Delta G°_{298} = -1.3$ kcal mol$^{-1}$. Using EXSYcalc,[136] rate constants of 4.1 s$^{-1}$ and 0.44 s$^{-1}$ were obtained, which correspond to $K_{eq} \sim 9$, in good agreement with the integration ratio. Similarly, for $L^2Al$(oLAOBn), $K_{eq}$ by integration is ~ 9.5 and $\Delta G°_{298} = -1.3$ kcal mol$^{-1}$, with rate constants 2.2 s$^{-1}$ and 0.25 s$^{-1}$, giving $K_{eq} \sim 8.8$. From part b, wherein only one enantiomer of LA was used, the data indicated that racemization at Al occurred. From parts c and d, exchange between peaks of the mixed complexes indicated the occurrence of intermolecular swapping of alkoxide chains. Taken together, the EXSY data are consistent with rapid equilibria in solution among all species (illustrated in Figure 4.10 for the case of $L^7Al$(oLAOBn)), favoring one diastereoisomeric pair ($K_{eq} = 9$), via all possible pathways (intermolecular alkoxide exchange and racemization at Al). Importantly, the data support thermodynamic control of stereoselectivity in the initiation, such that the product ratio is controlled by the relative stability of the products that rapidly equilibrate.

### 4.2.2 Theory

#### 4.2.2.1 Computational Methods

All stationary points were optimized at the M06-L[83] density functional theory (DFT) level using the 6-31+G(d,p)[47] basis set. Harmonic vibrational frequencies were computed at this level to verify the nature of all stationary points, and for use in molecular vibrational partition functions using the quasi-harmonic-oscillator approximation18 (where all frequencies below 50 $cm^{-1}$ are replaced by values of 50 $cm^{-1}$)[48]. Finally, single point DFT calculations at the SMD[51]/M06-2X[46]/6- 311+G(d,p) level of theory were carried out for all optimized structures to obtain improved electronic energies to which thermal contributions to free energy were added from the M06-L/6- 31+G(d,p) step. For the implicit solvation model, methylbutanoate was chosen as the solvent, as it most closely resembles Lactide melt conditions. The energetic results were also verified using other DFT methods. All DFT calculations were performed with the Gaussian 16 suite of electronic structure programs[86].

#### 4.2.2.2 Energetic results using different functionals

To make sure that the energetic results are independent of the choice of the level of theory, single point calculations using different functionals were carried out. Tables 4.2-4.4 show these results for Δ-$L^7$AlOMe, Δ-$L^7$AlOBn, and Δ-$L^2$AlOMe, respectively. There's significant variation between functionals in the computed barriers and reaction free energies. Specifically, M06-2X seems to predict lower free energy barriers as well as lower overall reaction free energies. However, the predicted *order* for the barriers of different pathways and different product enantiomers (which is what's relevant to the experimental results) remains the same.

**Table 4.2-** The barriers of each pathway for Δ-$L^7$AlOMe, with the lowest pathways shown in boldface.

| | M06-2X-D3[137] | B3LYP[138]-D3BJ[137] | PBE0[139]-D3 | wB97XD[140] |
|---|---|---|---|---|
| ax-D-si | 14.7 | 20.9 | 18.6 | 19.3 |

| | | | | |
|---|---|---|---|---|
| ax-D-re | **8.9** | **14.6** | **11.7** | **12.6** |
| ax-L-re | 11.0 | 16.8 | 14.3 | 15.3 |
| ax-L-si | 11.3 | 17.8 | 14.9 | 16.0 |
| eq-D-si | 20.2 | 24.9 | 22.8 | 23.8 |
| eq-D-re | **8.5** | **14.6** | **11.3** | **12.8** |
| eq-L-re | 11.8 | 17.6 | 15.2 | 16.1 |
| eq-L-si | 14.7 | 18.2 | 17.8 | 17.1 |
| L-Product | **-15.9** | **-9.1** | **-10.1** | **-10.2** |
| D-Product | -14.8 | -8.2 | -9.6 | -9.4 |

**Table 4.3-** The barriers of each pathway for the Δ-L$^7$AlOBn, with the lowest pathways shown in boldface.

| | M06-2X-D3 | B3LYP-D3BJ | PBE0-D3 | wB97XD |
|---|---|---|---|---|
| ax-D-si | 17.5 | 23.7 | 21.5 | 22.5 |
| ax-D-re | **11.9** | **17.0** | **14.1** | **15.8** |
| ax-L-re | 13.8 | 19.4 | 17.2 | 18.3 |
| ax-L-si | 12.7 | 18.8 | 16.4 | 17.5 |

**Table 4.4-** The barriers of each pathway for the Δ-L$^2$AlOMe, with the lowest pathways shown in boldface.

| | M06-2X-D3 | B3LYP-D3BJ | PBE0-D3 | wB97XD |
|---|---|---|---|---|
| ax-D-si | 21.1 | 25.0 | 24.0 | 24.1 |
| ax-D-re | **8.4** | **14.7** | **11.5** | **12.9** |
| ax-L-si | 9.6 | 15.7 | 12.9 | 14.2 |
| ax-L-re | 12.6 | 17.6 | 14.8 | 16.0 |
| eq-D-si | 51.5 | 49.7 | 50.1 | 50.8 |
| eq-D-re | **10.7** | **16.3** | **13.4** | **14.8** |

| | | | | |
|---|---|---|---|---|
| eq-L-re | 12.5 | 18.2 | 15.6 | 16.9 |
| eq-L-si | 49.4 | 48.2 | 48.0 | 49.2 |
| L-Product | -10.4 | -5.6 | -7.9 | -6.8 |
| D-Product | -9.9 | -5.3 | -7.4 | -6.5 |

To better understand factors contributing to stereocontrol in the initiation process that we were able to characterize experimentally, the free energy profiles for the initiation steps associated with both $L^2$AlOR and $L^7$AlOR were computationally determined for both L(*S*,*S*)- and D(*R*,*R*)-LA . Both $L^7$AlOMe and $L^7$AlOBn were examined in order to assess the significance of variation of the alkoxide. Since the results were similar, only the methoxy initiator was considered for all other catalysts in order to reduce computational cost.

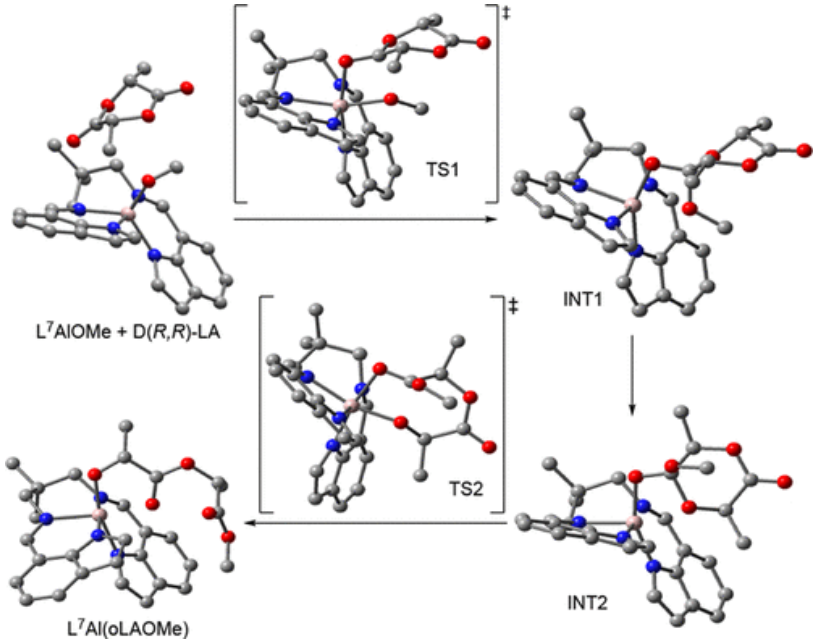


**Figure 4.11.** Illustration of the calculated initiation pathway for a selected catalyst (Δ-$L^7$AlOMe), substrate (D(*R*,*R*)-LA), and approach trajectory.

#### 4.2.2.3 Results

The results of energetic calculations for all reaction pathways involving Δ-$L^7$AlOMe, -$L^7$AlOBn, and -$L^2$AlOMe are shown in Table 4.5; data for (TBSsalen)AlOMe are shown

in Table 4.7. Where shown, product energies are listed for two pathways; all other pathways lead to one of those products. Finally, overall barriers for initiation are shown in the last column. Comparing the results in these tables, it is apparent that for both methoxy and benzyloxy as an initiator, reaction of the Δ isomer of the complexes with D(*R*,*R*)-LA is calculated to be kinetically favored for all complexes. There are differences in whether the *ax-re* or *eq-re* pathways are preferred, depending on the nature of the ligands (see Supporting Information). Importantly, these findings for the kinetic preferences are in disagreement with the stereochemistry observed in the X-ray crystal structures of $L^2$Al(oLAOBn) and $L^7$Al(oLAOBn) (Figure 4.9). In contrast, the Δ-L(*S*,*S*) isomer observed by X-ray crystallography is calculated to be thermodynamically more favorable for both $L^7$AlOMe and, to a lesser extent, $L^2$AlOMe. While the computed energy differences are small, suggesting that product mixtures might be expected under thermodynamic conditions, the agreement with the $\Delta G°_{298} = -1.3$ kcal mol$^{-1}$ for the postulated equilibria between the diastereomers determined from integration of NMR spectra is reasonable considering the inherent accuracy of the calculations (ca. ± 1 kcal mol$^{-1}$). Thus, the computations corroborate the conclusions drawn experimentally, that the stereoselectivity observed is determined by the relative thermodynamic stability of the products, and that the preferred stereoisomer is that which was characterized structurally by X-ray crystallography.

**Table 4.5.** Free Energies (kcal mol$^{-1}$) for Stationary Points along the Various Reaction Pathways for Initiation of LA by Δ-$L^7$AlOMe, Δ-$L^7$AlOBn, and Δ-$L^2$AlOMe[a]

| | path | TS1 | INT1 | INT2 | TS2 | prod | tot.[b] |
|---|---|---|---|---|---|---|---|
| **$L^7$AlOMe** | *ax*-d-*si* | 9.8 | 2.7 | 3.7 | 14.7 | –14.8 | 14.7 |
| | *ax*-d-*re* | 8.8 | –0.5 | 3.0 | 8.4 | | **8.9** |
| | *ax*-l-*re* | 9.0 | 1.5 | 4.8 | 11.0 | –15.9 | 11.0 |
| | *ax*-l-*si* | 8.7 | 0.5 | 3.6 | 11.3 | | 11.3 |
| | *eq*-d-*si* | 11.6 | 4.8 | 3.8 | 20.2 | | 20.2 |
| | *eq*-d-*re* | 8.5 | 1.7 | 2.3 | 7.8 | | **8.5** |
| | *eq*-l-*re* | 9.7 | 3.3 | 5.5 | 11.8 | | 11.8 |
| | *eq*-l-*si* | 10.8 | 2.1 | 4.3 | 14.7 | | 14.7 |
| **$L^7$AlOBn** | *ax*-d-*si* | 9.4 | 3.6 | 5.3 | 17.5 | | 17.5 |

| | | | | | | | |
|---|---|---|---|---|---|---|---|
| | *ax*-d-*re* | 11.9 | 3.7 | 4.9 | 10.7 | | **11.9** |
| | *ax*-l-*re* | 9.4 | 3.4 | 6.2 | 13.8 | | 13.8 |
| | *ax*-l-*si* | 10.3 | 3.1 | 3.8 | 12.7 | | 12.7 |
| | *eq*-d-*si* | 19.0 | 12.2 | 11.6 | 28.9 | | 28.9 |
| | *eq*-d-*re* | 17.4 | 10.6 | 10.2 | 15.7 | | 17.4 |
| | *eq*-l-*re* | 16.4 | 12.0 | 13.5 | 19.3 | | 19.3 |
| | *eq*-l-*si* | 19.3 | 13.4 | 13.6 | 23.9 | | *23.9* |
| **$L^2$AlOMe** | *ax*-d-*si* | 9.5 | 4.8 | 4.8 | 21.1 | –9.9 | 21.1 |
| | *ax*-d-*re* | 7.3 | 0.8 | 4.7 | 8.4 | | **8.4** |
| | *ax*-l-*re* | 8.0 | 2.4 | 5.2 | 9.6 | –10.4 | 9.6 |
| | *ax*-l-*si* | 10.0 | 2.4 | 9.7 | 12.6 | | 12.6 |
| | *eq*-d-*si* | 14.9 | 6.9 | 6.4 | 51.5 | | 51.5 |
| | *eq*-d-*re* | 9.4 | 2.0 | 3.8 | 10.7 | | 10.7 |
| | *eq*-l-*re* | 10.4 | 4.0 | 6.2 | 12.5 | | 12.5 |

[a] Gibbs free energies (kcal $mol^{-1}$, 298.15 K) computed at SMD/M06–2*X*/6-311+G(d,p)//M06-L/6-31+G(d,p) level for stationary points. Lowest total energies for catalyst indicated in bold. [b] Tot. = overall energy barrier.

Again, however, because the calculated energy differences between the products are small, we cannot unambiguously rule out the possibility that the minor isomer is the one that crystallizes.

Putting these findings in context, previous DFT investigations of the origins of stereoselectivity in LA polymerizations by metal-alkoxide catalysts have focused on differences in kinetic barriers for ring-opening of LA stereoisomers.[134,141–144] Both kinetic and thermodynamic preferences were identified by theory for the addition of a second monomer to the initially formed ring-opened species in syndiotactic polymerization of *rac*-β-butyrolactone by yttrium catalysts supported by salan-type ligands.[142] Small energetic differences arising from subtle secondary interactions (typically with the growing chain end in propagation steps) were identified in the previous DFT studies.[145] While general rules for predicting stereoselectivity are lacking, the finding herein that thermodynamic control of stereoselectivity in ROTEP initiation suggests that similar ideas should be considered in evaluating stereocontrol in propagation reactions.

#### 4.2.2.4 Structural Influences on Selectivity for the equatorial coordination mode

To understand the origins of the pathway energetic orderings described in the paper, we consider two kinds of differentiating interactions: interactions internal to the "tetrahedral intermediate" (i.e., the product of the initial nucleophilic attack, absent any consideration of the catalyst), and interactions between the bound, reacting substrates and the catalyst itself.

In the absence of a catalyst, we need consider only the attack of an alkoxy nucleophile on the re and si faces of a given lactide enantiomer (Figure 4.12). The tetrahedral intermediate derived from attack on the *si* face of D-lactide, which is the enantiomer of that derived from attack on the re face of L-lactide, is computed to be 3.1 kcal $mol^{-1}$ higher in energy than the intermediate derived from attack on the opposite face of the carbonyl. This difference in energy is attributable to the twist-boat conformation preferred by the lactide ring; attack on the *si* face leaves the methoxy group on the same side of the ring as the flagpole hydrogen atoms while attack on the re face places this group on the opposite side, which has much less steric congestion. The preference for D-*re* over D-*si* is well reflected in the energetic orderings of the TS1 and INT1 structures for both catalysts in Figure 4.13, while in the case of L-*si* vs L-*re*, some variation is seen, presumably owing to interactions with the catalyst itself.

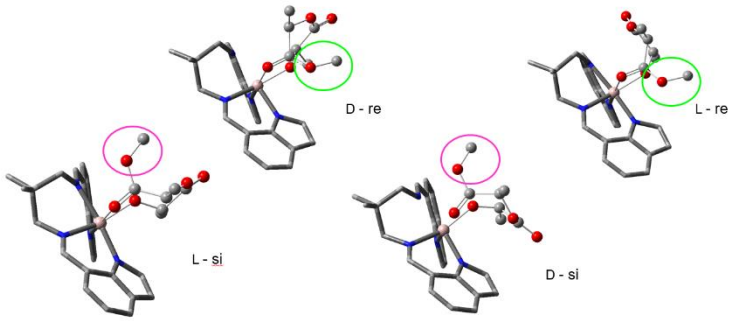


**Figure 4.12.** TS2 structures for all pathways with the Δ-$L^7$AlOMe catalyst. The structural analogy independent of lactide along the si vs the re pathways is highlighted by circling the methoxy groups.

Turning next to interactions between the catalysts and the reacting substrates, there are similarities in TS2 structures for all re-face pathways as well as for all *si*-face pathways, as illustrated in Figure 4.13 for the case of the Δ-L$^7$AlOMe catalyst. Close examination of the TS2 structures along the *si* pathways (Figure 4.13) finds close contacts between the indole rings on the catalyst and the opening lactide, leading to higher energies through steric repulsion and internal substrate structural deformation. These contacts are more significant in the L$^2$AlOMe catalyst, and indeed so much so that in the case of D-lactide TS2 is found at very high energy.

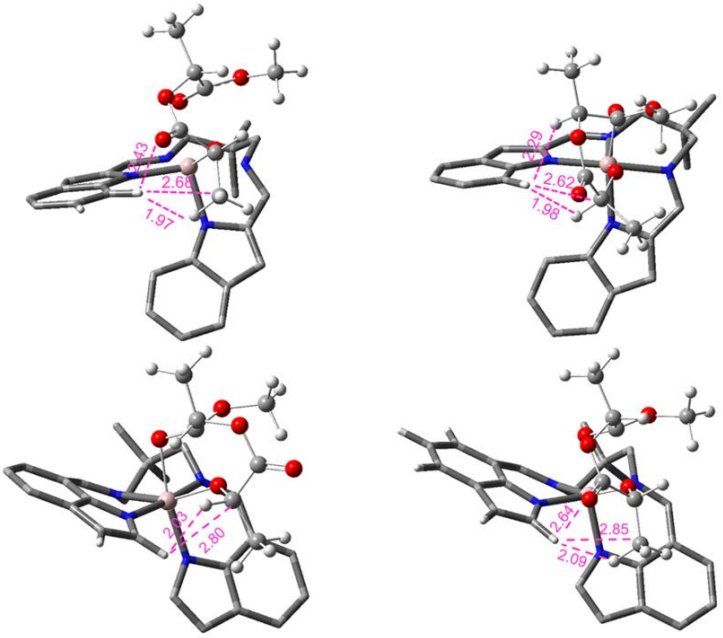


**Figure 4.13.** Structures of TS2 along *si* face reaction pathways for the Δ-L$^7$AlOMe (top) and Δ-L$^2$AlOMe (bottom) catalysts.

The influence of this contact is also reflected in the bond angles around the Aluminum center. The N(1)-Al-O(1) and N(2)-Al-O(1) angles (See figure 4.14), as well as their differences and sums) are listed in table 4.6. More positive differences between indicate a repulsive interaction between the Lactide unit and the indolide ligands. And indeed, more positive values for this difference are observed for the si pathways. These bond angles are useful as a measure since they can be used across different pathways and catalysts.

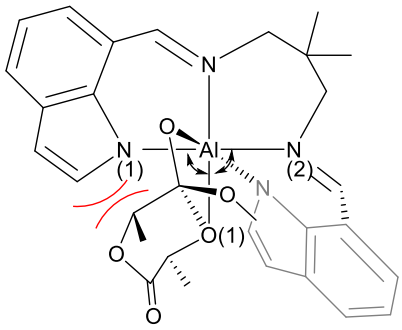


**Figure 4.14.** The N(1)-Al-O(1) and N(2)-Al-O(1) angles shown for TS2 (L-si pathway) in the $L^7$AlOMe catalyst as an example.

**Table 4.6.** The values of N(1)-Al-O(1) and N(2)-Al-O(1) bond angles in TS2 of all pathways for $L^7$AlOMe and $L^2$AlOMe

| Catalyst | | D-*si* | D-*re* | L-*re* | L-*si* |
|---|---|---|---|---|---|
| $L^7$AlOMe | N(1)-Al-O(1) | 103.2 | 89.3 | 87.8 | 100.3 |
| | N(2)-Al-O(1) | 85.3 | 95.1 | 96.9 | 86.3 |
| | Difference | **17.9** | **-5.8** | **-9.1** | **14.0** |
| | Sum | 188.5 | 184.5 | 184.6 | 186.7 |
| $L^2$AlOMe | N(1)-Al-O(1) | 111.7 | 96.3 | 93.9 | 105.5 |
| | N(2)-Al-O(1) | 86.5 | 97.9 | 101.4 | 91.2 |
| | Difference | **25.3** | **-1.6** | **-7.5** | **14.4** |
| | Sum | 198.2 | 194.1 | 195.3 | 196.7 |

The different propensities of the $L^2$AlOMe and $L^7$AlOMe catalysts to select for D- vs L-lactide may be understood from consideration of the various interactions alluded to above. In the absence of catalyst, paths following D-*re* and L-*si* pathways begin preferred. However, the Δ catalysts selectively differentiate structures along the re and si pathways. As shown in Figure 4.15, when that differentiation is modest, the catalyst can effectively select for D over L. However, if this differentiation becomes the dominant consideration, then the intrinsic stability of the D-*re* structure over the L-*re* early along the pathway exerts minimal influence, and selectivity for D over L is reduced. The former case better describes $L^7$AlOMe, while the latter case better describes $L^2$AlOMe.

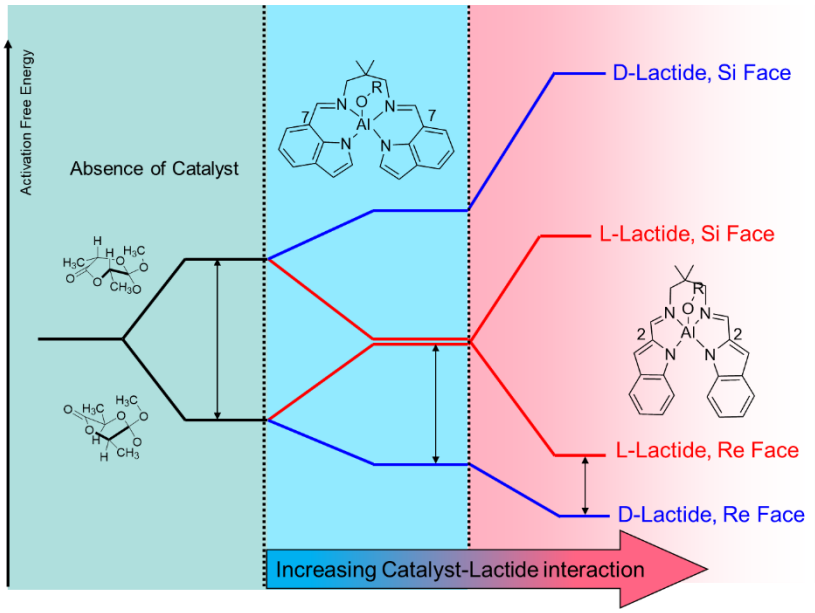


**Figure 4.15.** Schematic representation of the influence of catalyst-lactide interactions vs internal substrate interactions on the overall activation free energy for lactide initiation by Δ aluminum indolide catalysts.

### 4.2.2.5 Structural Influences on Selectivity for the axial coordination mode

In the axial coordination pathways, INT1 is higher in energy than the equatorial coordination mode in all cases. This can be attributed to the steric interaction of the methoxy group with the backbone of the catalyst (see figure 4.16). The same structural features that lead to the higher energies of INT1 can raise the transition state for the initial nucleophilic attack as well. This destabilization can be expected to increase if the methoxy group is replaced with the polymer chain (see section 4.3.4.1).

For intermediate 2, in all cases except for D-*re*, the energy is higher for the axial pathway. It's worth mentioning that in INT2, for the cases of *si*-face pathways, the intermediate is coordinated in a mono-dentate form, (similar to what was observed in the $L^2$AlOMe in equatorial coordination mode, See figure 4.18). This can be attributed to the interaction of the Lactide with the backbone, as opposed to interaction of Lactide with the indole ring as is the case for the equatorial face.

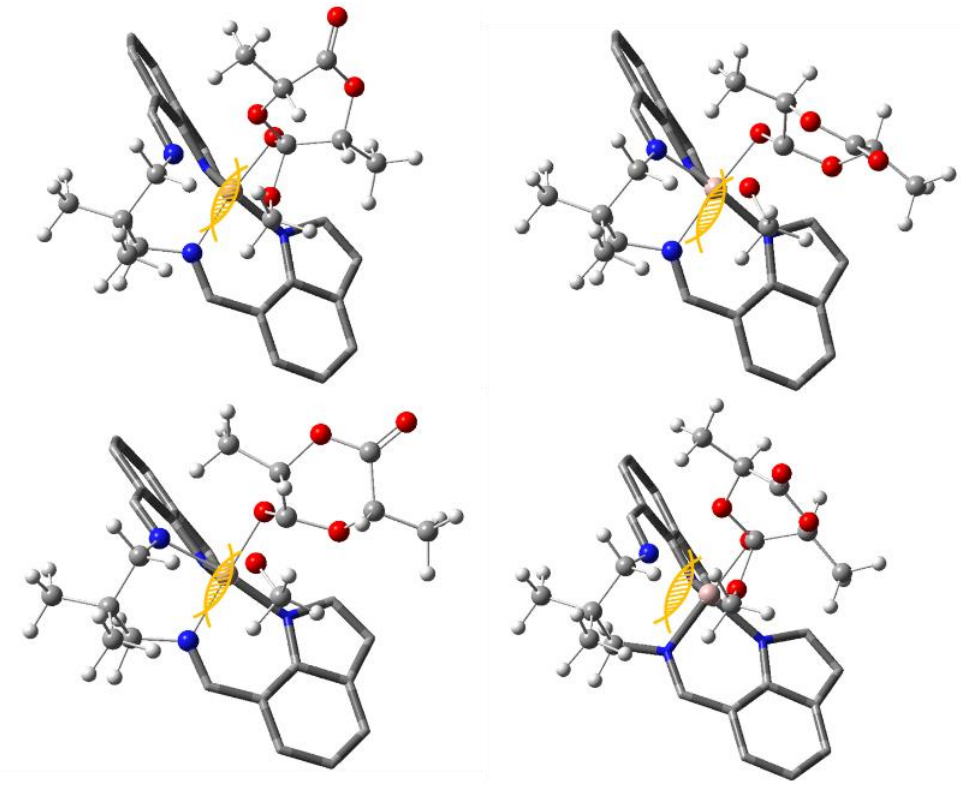

**Figure 4.16.** Steric interaction between methoxy group and the backbone in INT1 for the axial coordination pathways.

Interestingly, the In this case, the steric interaction in the high *si*-face pathways are between the Lactide and the aliphatic portion of the catalyst backbone, as opposed to the Indole rings in the front of the catalyst (see figure 4.17).

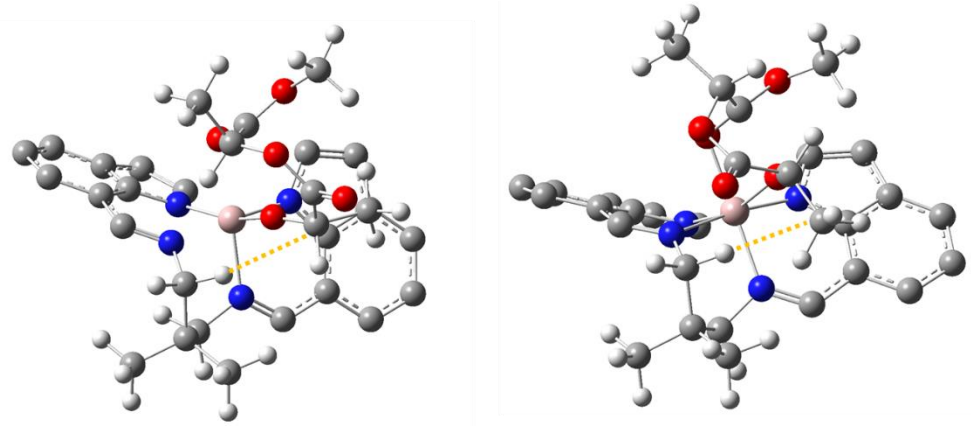

**Figure 4.17.** – Structure of transition state 2 for D-*si* and L-*si* pathways for axial coordination mode.

Although the focus was mostly on the $L^7$AlOMe in this section, similar trends explain the energetic ordering of different equatorial coordination pathways for $L^2$AlOMe. However, these trends are more extreme in the latter, with the si pathways being around 50 kcal.mol$^{-1}$ high in energy. In the case of $L^2$AlOMe, the poor coordination of INT2 leads to a non-coordinated transition state, which greatly increases the barrier, making it an effectively non-catalyzed bond-breaking. This is also reflected in the low imaginary frequency of TS2 in these pathways (44.3 cm$^{-1}$ for D-*si*, and 80.8 for L-*si*), as the reverse reaction is effectively barrierless.

It's also important to note that the ax-D-*re* pathway has a barrier even lower than eq-D-*re*. This highlights the importance of considering various coordination modes for all pathways in the computational study of ROTEP, as shown in other studies.

#### 4.2.2.6 Energetic data for the TBS(salen)AlOMe catalyst

Table 4.8 shows the barriers of different pathways for Lactide ring-opening for the (salen)AlOMe catalyst. The order for some of the intermediate energy pathways differs from the indolide catalysts, but the selectivity remains the same.

**Table 4.7.** Energetic data for the initiation of lactide by (salen)AlOMe catalyst.

| | TS1 | INT1 | INT2 | TS2 | Overall Barrier |
|---|---|---|---|---|---|
| ax-D-si | 10.9 | 3.5 | 7.3 | 16.1 | 16.1 |
| ax-D-re | 10.0 | 1.3 | 4.5 | 13.6 | 13.6 |
| ax-L-re | 9.6 | 3.1 | 5.9 | 11.6 | 11.6 |
| ax-L-si | 12.5 | 1.8 | 2.5 | 7.8 | 12.5 |
| eq-D-si | 11.3 | 11.1 | 5.5 | | |
| eq-D-re | 8.3 | 4.8 | 5.0 | 8.2 | **8.3** |
| eq-L-re | 10.5 | 6.7 | 10.0 | 15.0 | 15.0 |
| eq-L-si | 12.7 | 5.1 | 7.9 | 14.5 | 14.5 |

### 4.2.2.7 Monodentate coordination of the tetrahedral intermediate in *si* pathways in $L^2$AlOMe

In the case of the 2-indole catalyst, due to the repulsion between the indole rings on the catalyst and the Lactide in si-face pathways, intermediate 2 becomes unstable. As a result, the monodentate coordination of the tetrahedral intermediate (shown in figure 4.18) is more stable.

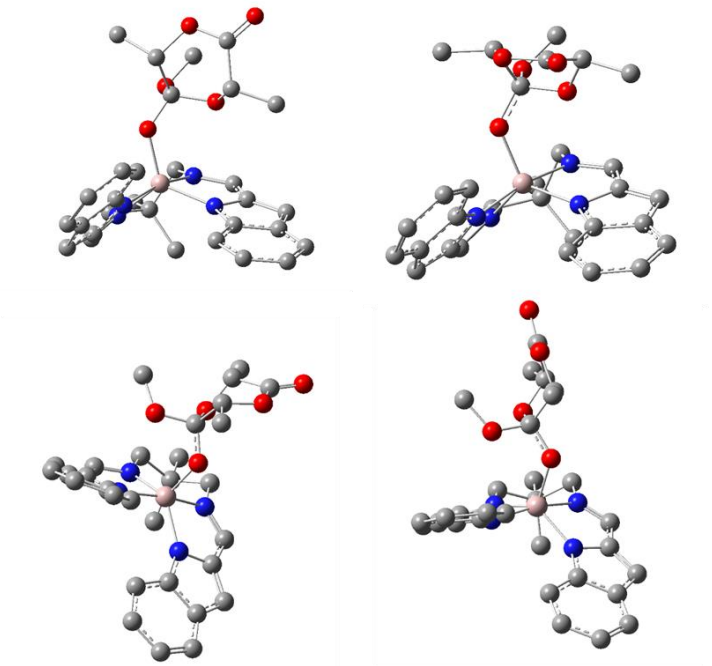

**Figure 4.18.** Structures of monodentate intermediate for 2-indole catalyst, for D-si (right) and L-si (left) for axial (top) and equatorial (bottom) pathways.

In the case of the D-*si* pathway, no minimum corresponding to intermediate 2 was found at the M06-L/6-31+G(d,p) level of theory, suggesting that if such a minimum exists, it's in a very shallow well on the potential energy surface. In both L-*si* and D-*si* pathways, the monodentate coordination mode has less than 1.0 kcal.mol$^{-1}$ energy difference with intermediate 1.

### 4.2.2.8 Detailed Free Energy Profile for the Fluxionality of Indolide Catalysts

Fig. 4.19 shows the reaction free energy profile for the fluxionality of $L^7$AlOBn. Note that even though the reactants and products are enantiomers of one another, because the

transition state is not fully symmetric, the path forward and backward for chirality inversion is identical.

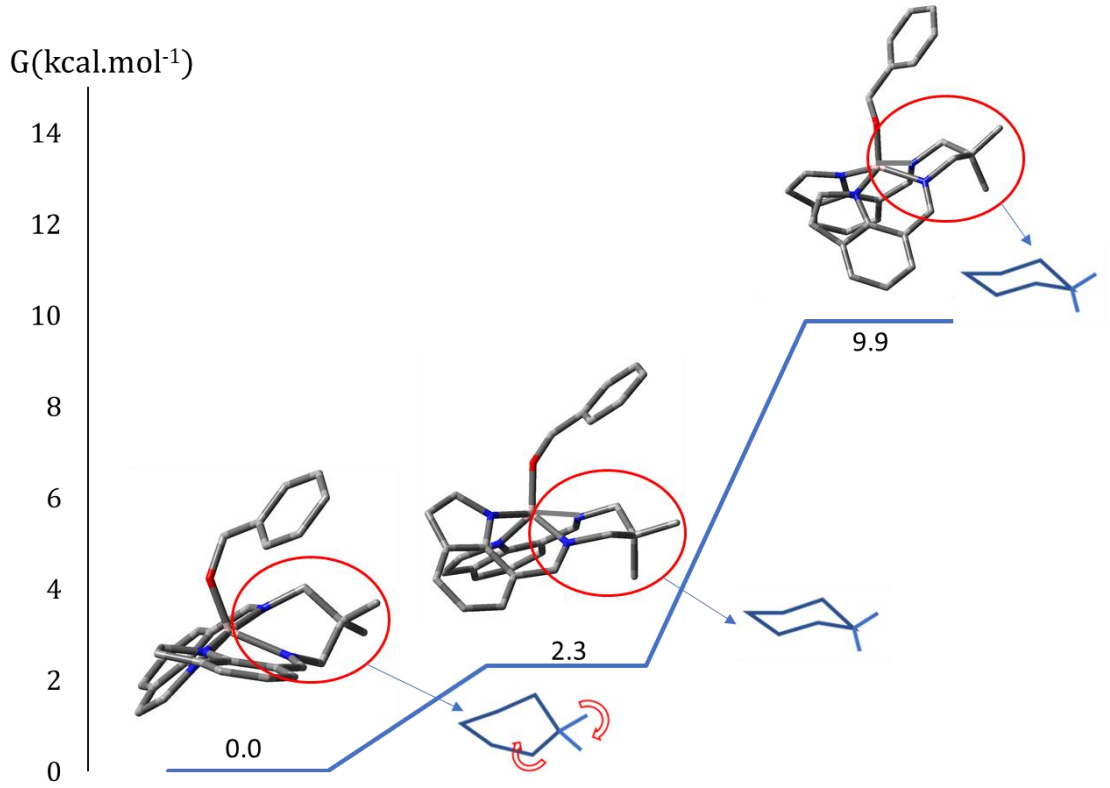


**Figure 4.19.** Mechanism of chirality inversion in catalyst $L^7$AlOBn. As shown here, the mechanism involves a change in the conformation of the metallacycle from a twist-boat to chair conformation.

For site-controlled enantioselectivity to be a viable mechanism, the ring opening of Lactide must occur at a higher rate than the inversion of catalyst chirality. The barriers found for chirality inversion are indeed higher, but comparable to ring-opening rates. But these values are for the catalyst and the initiator itself. A better way to see if the catalyst maintains its chirality during the course of the reaction is to find the barrier for chirality inversion for the catalyst with a ring-opened monomer coordinated to it. The barrier for this was found to be significantly higher for the 7-connected catalyst, at 15.6 kcal $mol^{-1}$, suggesting that site-controlled enantioselectivity is a plausible mechanism. Looking at

figure 4.20, the reason for this high barrier seems to be a favorable interaction between the ring-opened lactide and Indole rings that is absent in the transition state.

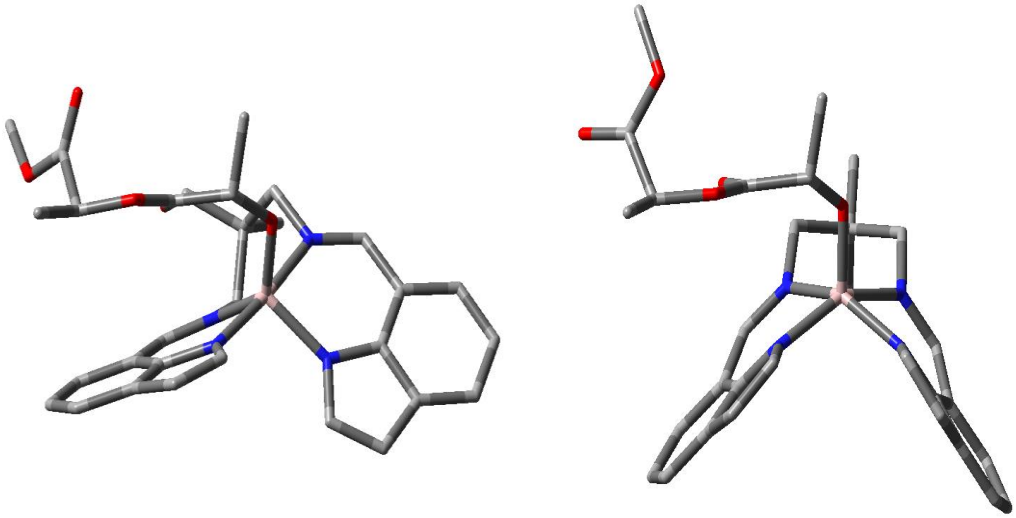

**Figure 4.20.** structure of the 7-indole catalyst with the ring-Opened Lactide coordinated, and the transition state for its chirality inversion

### 4.2.3 Conclusions

We have synthesized and characterized the solution and solid state structures of the complexes $L^2$AlOBn and $L^7$AlOBn, including the delineation of the nature of the fluxional process that interconverts the enantiomeric forms of the complexes through VT-NMR spectroscopy and computations. The complexes polymerize *rac*-LA stereoselectively. As a first step toward developing a molecular-level understanding of the mechanistic basis for the observed stereoselectivity, we studied the initiation reaction. Treatment of the complexes with 1 equiv of *rac*-LA yielded the ring-opened products $L^2$Al(oLAOBn) and $L^7$Al(oLAOBn), and on the basis of NMR spectroscopy, the major product for each reaction was identified as a single diastereomer (pair of enantiomers). Crystals isolated from the product solutions were characterized by X-ray diffraction, revealing unambiguously for the first time the detailed molecular structure and stereochemistry of a product of initiation of cyclic ester polymerization by a metal–

alkoxide complex. Studies of the product solutions by EXSY NMR showed that the products exist as stereoisomers that rapidly interconvert via both intermolecular alkoxide exchange and racemization at the Al center. Examination of the initiation reactions by theory delineated the mechanistic details, in particular the reaction energetics as a function of stereochemistry. We conclude, with appropriate caveats because of the small energetic differences found by theory, that the stereoselectivity observed in the initiation reaction is likely not the result of kinetic preferences (which predict preferential formation of the stereoisomer *not* observed by X-ray crystallography). Instead, thermodynamic control of selectivity is supported by the experimental NMR data indicative of equilibration of diastereomers in solution and by the prediction by theory that the stereoisomer observed by X-ray crystallography is the most stable (keeping in mind the possibility, albeit in our view unlikely, that the crystals isolated could be the minor isomer).

In addition to providing specific information on particular systems, the mechanistic results reported herein significantly augment our general understanding of stereocontrol of ROTEP initiation by metal-alkoxide complexes and suggest the importance of thermodynamic control in determining the favored product stereoisomer. We speculate that similar considerations apply to understanding subsequent monomer enchainment, the stereochemistry of which may similarly rely on product stability rather than kinetic barriers typically emphasized in theoretical studies.

## 4.3 Propagation Study

### 4.3.1 Computational Methods

The mechanism considered for the propagation was the same as initiation mechanism, starting with the binding of the Lactide monomer and the nucleophilic attack from the alkoxy group through TS1, forming the tetrahedral intermediate species that is stabilized by the catalyst, followed by the opening of the Lactide ring through TS2 (see Figure 2). The only difference is the alkoxy group, which is the chain end, instead of the initiator.

For all relevant stationary points across the potential energy surface, Monte Carlo searches for low-energy conformations of the system were carried out using the OPLS3 force field.[82] The purpose of this initial search was to find a range of conformers with reasonable structures as starting points for further optimization. These conformers were then further optimized at the M06-L[83] density functional theory (DFT) level using the 6-31G(d,p)[47] basis set. Harmonic vibrational frequencies were computed at this level to verify the nature of all stationary points, and for use in molecular vibrational partition functions using the quasi-harmonic-oscillator approximation18 (where all frequencies below 50 $cm^{-1}$ are replaced by values of 50 $cm^{-1}$)[48]. Finally, single point DFT calculations at the SMD[51]/M06-2X[46]/6- 311+G(d,p) level of theory were carried out for all unique optimized structures to obtain improved electronic energies to which thermal contributions to free energy were added from the M06-L/6- 31+G(d,p) step. Additionally, the entropic contribution to the free energy of all stationary points arising from the conformational degrees of freedom were also computed and added as a correction. For the implicit solvation model, methylbutanoate was chosen as the solvent, as it most closely resembles Lactide melt conditions. The energetic results were also verified using other DFT methods. All DFT calculations were performed with the Gaussian 16 suite of electronic structure programs[86], , and the initial Monte Carlo search was done in MacroModel.[87]

For transition state structures, the process was modified to search only for structures that would be likely to optimize to a viable transition state. The bond distances for both transition states were fixed before the initial Monte Carlo search at 1.90 Angstroms, which is about the average value of this bond distance across all the transition states, for both steps studied in our previous study on the initiation mechanism. Then, a constrained DFT optimization, with the bond distance fixed at the same value, was carried out. Finally, the structures in which the pattern of the coordination of the oxygen atoms to the Aluminum center matched that of the expected transition state (Lactyl and carbonyl Oxygen atoms for TS2, and Alkoxy and Carbonyl Oxygen atoms for TS1), were chosen for further transition state optimization.

The chain-end monomers were truncated as shown in Scheme 4.4 to reduce computational cost. Most of the rest of the chain is unlikely to affect the selectivity due to its distance from the Aluminum center.

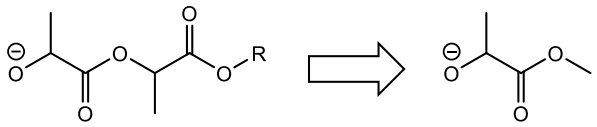

**Scheme 4.4**. Truncated chain end monomer

### 4.3.2 Discussion

*Results*. Table 4.9 shows the free energy of activation for TS1 and TS2 for the different pathways.

Unlike in the initiation, in the propagation stage, the activation energy for the insertion (TS1) is higher than the ring-opening in most cases. This is expected, because the chain-end alkoxy groups contain secondary carbons that are both larger and less flexible in terms of rotation around the CO bond, which makes steric clash more difficult to avoid.

**Table 4.8.** Activation free energies for TS1 and TS2 (all in kcal.mol$^{-1}$)

| Pathway | TS1 | TS2 |
|---|---|---|
| DD-re | **14.96** | 9.75 |
| DD-si | 9.13 | **18.46** |
| DL-re | **14.53** | 11.20 |
| DL-si | **17.53** | 10.70 |
| LD-re | **14.15** | 6.12 |
| LD-si | 14.08 | **14.81** |
| LL-re | **12.29** | 11.02 |
| LL-si | **14.84** | 13.25 |

The exceptions to this trend (LD-si and DD-si) have higher values for TS2 than TS1 for reasons relating to site-control mechanism and catalyst-substrate interactions analogous to the initiation mechanism, explored in our previous study. In fact, for TS2, the same order of reactivity was observed across all alkoxy groups, regardless of size (see Table

4.10). The steps with the lowest energy activation free energy for each pathway are shown in boldface, and the highest energy ones are underlined.

**Table 4.9.** Free energy of activation for the ring opening step (TS2) for different alkoxy groups (all values in kcal.mol$^{-1}$)

| | D-Lactide | L-Lactide | OMe | OBn |
|---|---|---|---|---|
| D-re | **9.7** | **6.1** | **8.5** | **11.9** |
| D-si | <u>18.5</u> | <u>14.8</u> | <u>9.8</u> | <u>17.5</u> |
| L-re | 11.2 | 11.0 | 9.0 | 13.8 |
| L-si | 10.7 | 13.3 | 8.7 | 12.7 |

Unlike in TS2, in the case of TS1, the ordering of the activation free energy for different pathways varies for different alkoxy groups, as shown in Table 4.11. This is to be expected, as the value of this activation free energy is heavily dependent on the nature of the alkoxy groups.

**Table 4.10.** Free energy of activation for the insertion step (TS1) for different alkoxy groups (all values in kcal.mol$^{-1}$)

| | D-Lactide | L-Lactide | OMe | OBn |
|---|---|---|---|---|
| D-re | 15.0 | 14.2 | **8.5** | <u>11.9</u> |
| D-si | **9.1** | **14.1** | <u>9.8</u> | **9.4** |
| L-re | 14.5 | 12.3 | 9.0 | **9.4** |
| L-si | <u>17.5</u> | <u>14.8</u> | 8.7 | 10.3 |

Despite the opposing directions of enantioselectivity in TS1 and TS2, the overall enantioselectivity is predicted to be high, favoring L-Lactide. Assuming kinetic control (and ignoring side-reactions and exchange), the expected $P_m$ value is 0.93 (see SI).

*Structural Factors*. To gain a better understanding of the structural factors responsible for the variations in activation energies in the insertion step, the pathways were broken down further to include the coordination mode (axial vs. equatorial). 4.12 contains the activation free energies for all the aforementioned pathways, and for L and D-Lactide chain end alkoxy groups.

**Table 4.11**. Free energy of activation for the insertion step (TS1) for different alkoxy groups (all values in kcal.mol$^{-1}$)

| TS1 | D | L |
|---|---|---|
| eq-D-re | 15.9 | 15.1 |
| ax-D-re | 15.5 | 14.7 |
| eq-D-si | 9.1 | 14.4 |
| ax-D-si | **16.0** | **15.1** |
| eq-L-re | 14.6 | 13.2 |
| ax-L-re | 16.4 | 13.3 |
| eq-L-si | **18.4** | 14.9 |
| ax-L-si | 18.1 | **17.4** |

Some general trends observed in table 4.12 are worth noting. D-re and L-si pathways are on average higher than their D-si and L-re counterparts. As seen in figure 3, the structure of the tetrahedral intermediate for these two pathways are enantiomers, and as such, the intramolecular interactions within the tetrahedral intermediate are similar.

As seen in Figure 4.20, in these structures, the Lactide unit is "bent" towards the alkoxy unit, this causes steric clash between the chain-end Lactide.

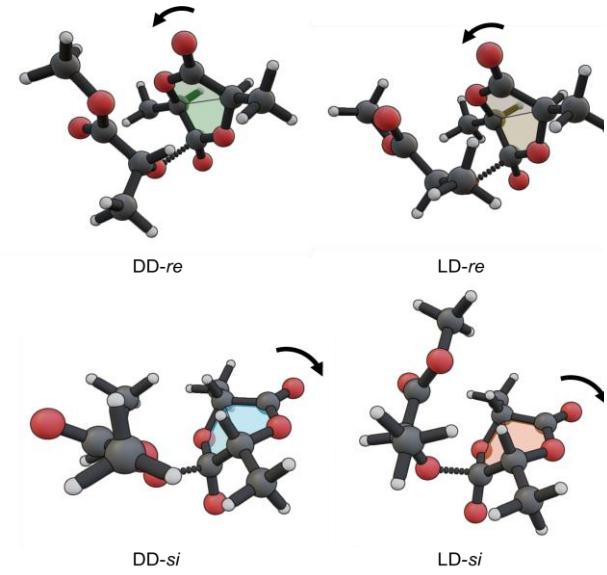


(a)

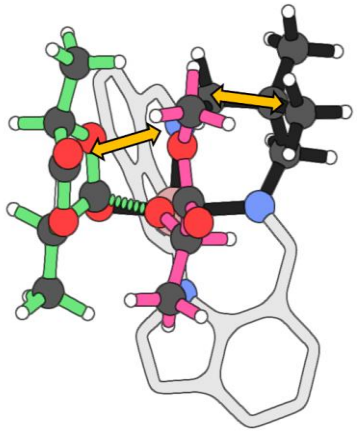

(b)

**Figure 4.21.** (a) Structures of the tetrahedral intermediates in the lowest energy conformers of the ring opening transition state, and the orientation of the unbound Lactide carbonyl, as well as the rest of the Lactide unit, towards the chain end. The structures shown are for D-Lactide. The structures for L-Lactide are enantiomers of these structures. (b) the TS structure for the ax-LL-si pathway, with the Lactide shown in green, the chain-end in pink, and the catalyst backbone in black. The chain-end monomer is squeezed between the backbone and the Lactide.

Another notable trend is the difference between the activation free energies in the axial and equatorial positions. These two different coordination modes correspond to completely different steric environments (see Figure 4.21). While the Lactide ligand can come into contact with the catalyst, the effect of this contact is subtle, as evidenced by the relatively small variation in the value of TS1 for the initiation, where the alkoxy group is small (see Table 4.11). As such, most of the interactions between the catalyst and chain-end come in the form of steric clash between the chain-end monomer and the catalyst. In the equatorial coordination modes, the chain end is pointing away from the catalyst, and as such it can avoid steric clash. In the axial coordination mode, there's a possibility of steric clash between the chain-end and catalyst backbone, and whether or not there's a large energy difference between the axial and equatorial coordination modes depends on whether or not there exists a chain-end conformer that can avoid this steric clash. Where there is a significant difference, the activation free energy for the axial coordination mode is larger than the equatorial mode.

In the case of ax-L-si, the structure of the tetrahedral intermediate restricts the movements of the chain end, making steric clash with the catalyst backbone difficult to avoid, effectively "squeezing" the backbone between the Lactide and the catalyst (see Figure 4.21). A similar interaction between the chain-end monomer and the indole rings is responsible for the high energy of the eq-LL-si pathway.

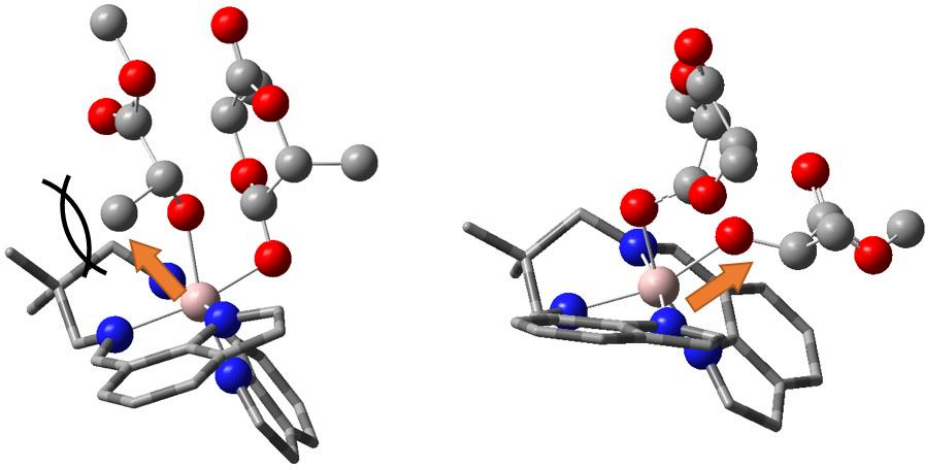

**Figure 4.22.** The different interactions of the chain end monomer in TS2 in the axial and equatorial coordination modes.

The exact energetic ordering of these various pathways is a function of the combination of the aforementioned variables, as well as others (including the chirality of the chain-end monomer). While the study of the details of all the many interactions leading to the observed order of activation energies is insightful, there are no singular structural factors that can explain the overall selectivity of the catalyst on their own. In many cases, the differences between the activation free energies of these pathways are small, despite significant structural differences and steric environments. As such, it's difficult to attribute the resulting stereoselectivity to any single structural factor.

### 4.3.3 Conclusions

In systems with multiple mechanistic pathways, successful rational design of enantioselective catalysts may require more than the consideration the chirality of the catalyst and the substrate. The existence of other mechanistic degrees of freedom make it so that the outcome of modifying the catalyst structure is not readily apparent, as a change that might promote enantioselectivity in one pathway might lead to a decrease in other pathways. One possible way to circumvent this challenge is making modifications

that eliminate some of these mechanistic variables. While there is no intrinsic advantage in promoting, say, a specific coordination mode, doing so simplifies the system and its mechanistic possibilities by removing a degree of freedom.

For Lactide polymerization in systems analogous to the one studied here, this may be achieved by having additional Lewis-acid or cationic moieties bound to the catalyst that interact with the non-reacting end of the incoming Lactide monomer, or the chain-end monomer in ways that promote certain coordination modes and prochiralities.

### 4.3.4 Other Structural Trends

#### 4.3.4.1 Notes on the coordination mode of the tetrahedral intermediate

Similar to the case of the $L^2$AlOMe catalyst discussed in section 4.2.2.7, in the case of $L^7$AlOR (where R is the chain-end monomer), the tetrahedral intermediate has a strong preference for monodentate coordination, despite the fact that in the initiation mechanism, the bidentate coordination modes were found to be more favored. Moreover, all tetrahedral intermediates were higher in energy than the separated reactants, indicating that the insertion step is thermodynamically unfavorable in the propagation steps. Interestingly, the coordination mode corresponding to INT1 (see 4.22) is not favored in any of the intermediates. This is another consequence of the steric effects of the chain-end monomer, leading to unfavorable coordination.

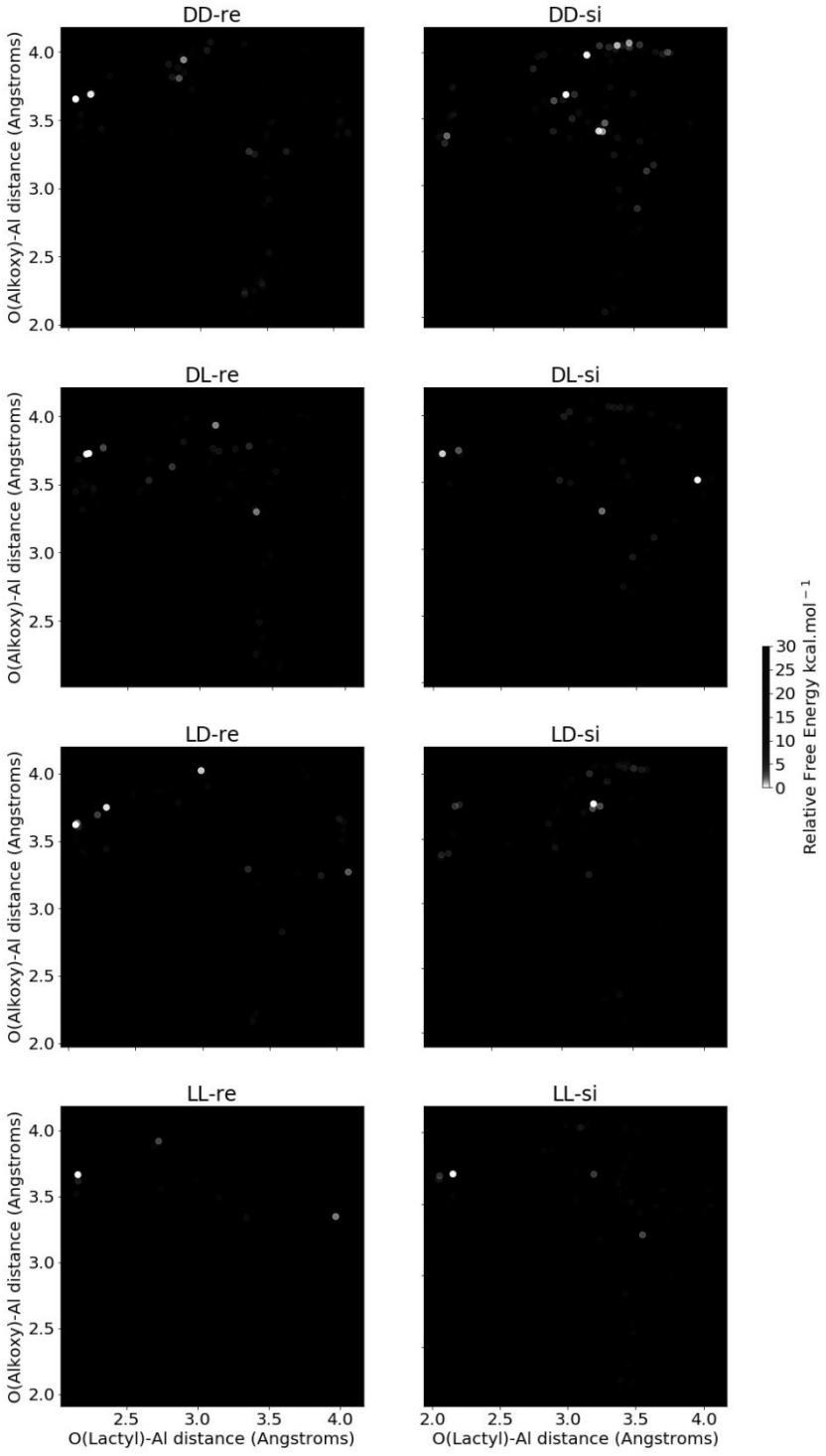


**Figure 4.23.** Relative free energies of the conformers of each possible tetrahedral intermediate as a function of the Al-O(Alkoxy) and Al-O(Lactyl) bond distances. In each of the plots, the

bottom-right corner corresponds to INT1, the top-left corner to INT2, and the top right corner represents the monodentate coordination mode.

#### 4.3.4.2 Computing the tacticity using rate constants

Assuming kinetic control, and ignoring side reactions, the tacticity ($P_m$) value of polymers is a function of the rate constants for the formation of monomers of different tacticity. While there exist approximations for the value of $P_m$ assuming chain-end or site-control mechanisms, in this system, both play a significant role, in a way that is not easily separable. An expression of the value for tacticity that does not assume SCM or CEM.

For a monomer of finite length, the probability of the formation of any specific sequence can be computed as the product of the probability of reactive events leading to its formation. For example, for the sequence D-L-L-L-D-D, the probability can be computed as a function of the probabilities of the reactive events as shown in equation 1.

$$P = p_D p_{DL} p_{LL} p_{LL} p_{LD} p_{DD} \quad (4.1)$$

There are 6 types of reactive events and associated probabilities that need to be considered. $P_D$ and $P_L$ are the probabilities that the monomer reacting in the initiation is D or L-Lactide. While, as discussed in our previous study, these probabilities differ, the effect of this difference diminishes with the addition of subsequent monomers. The other probabilities for LD, DL, LL, and DD are the probabilities of for the propagation reactions. These probabilities are related to one another according to the following equations 2-4.

$$P_{LD} + P_{LL} = 1 \quad (4.2)$$
$$P_{DL} + P_{DD} = 1 \quad (4.3)$$
$$P_D + P_L = 1 \quad (4.4)$$

Assuming that $P_D$ and $P_L$ are equal and set to one half, the final value of $P_m$ can be expressed by two independent probability values, $P_{DD}$ and $P_{LL}$, which we'll call x and y respectively.

Since there are N-1 adjacent dyads for a polymer of length N, the chance of choosing any specific dyad at random is 1/(N-1). The value of $P_m$ can be expressed as shown in equation 4.5.

$$P_m(N) = \frac{1}{N-1}\left(\sum_{i=1}^{N-1}\sum_{j} P_{ij}\right) \quad (4.5)$$

Where $P_{ij}$ is the probability of the occurrence of a sequence j where the dyad i has a *meso* stereochemistry. Each probability $P_{ij}$ is a polynomial function of x and y. by finding the general expression for an oligomer of length N and finding the limit for large values of N. Since $P_m$ is a polynomial expression in terms of x and y, we focused on finding the coefficient matrix for the polynomial. For an oligomer of finite length, this polynomial can be found by considering all the possible arrangements of monomers. Using the python Sympy library, the coefficient matrix was found for oligomers from the range 2 to 19 monomer units. An expression was found that matched all these matrices exactly, by examining the relationships between the integer coefficients of the matrices using the Online Encyclopedia of Integer Sequences (OEIS), shown in equation 4.6.

$$P_m = \frac{y(1-x)+x(1-y)}{(1-x)+(1-y)} = \frac{P_{DD}P_{DL}+P_{LD}P_{LL}}{P_{LD}+P_{DL}} \quad (4.6)$$

Since we expect the value of N to converge for larger values of N, we expect the sum expression to be first order with respect to N, at least for higher values of N.

This was confirmed by finding the value of $P_m$ for values of N up to 50. For larger values, due to the large coefficients in the polynomial, there were numerical instabilities. By finding a linear fit for the value of $2P_m(N-1)$, we were able to find the value of $P_m$ at N -> infinity for different values of x and y between 0 and 1, at intervals of 0.1. Using a rational function fit for $P_m(x,y)$, the expression in equation 7 was found to match exactly.

$$P_m = \frac{y(1-x)+x(1-y)}{(1-x)+(1-y)} = \frac{P_{DD}P_{DL}+P_{LD}P_{LL}}{P_{LD}+P_{DL}} \quad (7)$$

By computing the values of x and y in terms of the rate constant according to equations 4.8 and 4.9, the value of $P_m$ was computed to be 0.93.

$$x = P_{DD} = \frac{exp\left(-\frac{\Delta G^{\ddagger}_{DD}}{RT}\right)}{exp\left(-\frac{\Delta G^{\ddagger}_{DD}}{RT}\right)+exp\left(-\frac{\Delta G^{\ddagger}_{DL}}{RT}\right)} \quad (4.7)$$

$$y = P_{LL} = \frac{exp\left(-\frac{\Delta G^{\ddagger}_{LL}}{RT}\right)}{exp\left(-\frac{\Delta G^{\ddagger}_{LL}}{RT}\right) + exp\left(-\frac{\Delta G^{\ddagger}_{LD}}{RT}\right)} \quad (4.8)$$

# Bibliography


(1) Hospital, A.; Goñi, J. R.; Orozco, M.; Gelpi, J. L. Molecular Dynamics Simulations: Advances and Applications. *Adv. Appl. Bioinforma. Chem.* **2015**, *8*, 37–47.

(2) Senftle, T. P.; Hong, S.; Islam, M. M.; Kylasa, S. B.; Zheng, Y.; Shin, Y. K.; Junkermeier, C.; Engel-Herbert, R.; Janik, M. J.; Aktulga, H. M.; Verstraelen, T.; Grama, A.; van Duin, A. C. T. The ReaxFF Reactive Force-Field: Development, Applications and Future Directions. *Npj Comput. Mater.* **2016**, *2* (1), 1–14.

(3) Gao, J. Hybrid Quantum and Molecular Mechanical Simulations: An Alternative Avenue to Solvent Effects in Organic Chemistry. *Acc. Chem. Res.* **1996**, *29* (6), 298–305.

(4) Bowen, J.; Allinger, N. Molecular Mechanics: The Art and Science of Parameterization. In *Rev Comput Chem*; 2007; Vol. 3, pp 81–97.

(5) Szabo, A.; Ostlund, N., S. *Modern Quantum Chemistry: Introduction to Advanced Electronic Structure Theory*; Dover Publications, 1989.

(6) Cramer, C. J. *Essentials of Computational Chemistry: Theories and Models*; John Wiley & Sons, 2013.

(7) Kohn, W.; Sham, L. J. Self-Consistent Equations Including Exchange and Correlation Effects. *Phys. Rev.* **1965**, *140* (4A), A1133–A1138.

(8) Jones, R. O. Density Functional Theory: Its Origins, Rise to Prominence, and Future. *Rev. Mod. Phys.* **2015**, *87* (3), 897–923.

(9) Hasnip, P. J.; Refson, K.; Probert, M. I. J.; Yates, J. R.; Clark, S. J.; Pickard, C. J. Density Functional Theory in the Solid State. *Philos. Trans. R. Soc. Math. Phys. Eng. Sci.* **2014**, *372* (2011), 20130270.

(10) Gräfenstein, J.; Cremer, D. Can Density Functional Theory Describe Multi-Reference Systems? Investigation of Carbenes and Organic Biradicals. *Phys. Chem. Chem. Phys.* **2000**, *2* (10), 2091–2103.

(11) Brown, L. M. Paul A.M. Dirac's The Principles of Quantum Mechanics. *Phys. Perspect.* **2006**, *8*, 381–407.

(12) Schrödinger, E. An Undulatory Theory of the Mechanics of Atoms and Molecules. *Phys. Rev.* **1926**, *28* (6), 1049–1070.

(13) Born, M.; Oppenheimer, R. Zur Quantentheorie Der Molekeln. *Ann. Phys.* **1927**, *389* (20), 457–484.

(14) Sakurai, J. J.; Napolitano, J. *Modern Quantum Mechanics.*; Addison-Wesley, 2011.

(15) Slater, J. C. The Theory of Complex Spectra. *Phys. Rev.* **1929**, *34* (10), 1293–1322.

(16) Hohenberg, P.; Kohn, W. Inhomogeneous Electron Gas. *Phys. Rev.* **1964**, *136* (3B), B864–B871.
(17) Tsuneda, T. *Density Functional Theory in Quantum Chemistry*; Springer Japan: Tokyo, 2014.
(18) Perdew, J. P.; Schmidt, K. Jacob's Ladder of Density Functional Approximations for the Exchange-Correlation Energy. *AIP Conf. Proc.* **2001**, *577* (1), 1–20.
(19) Becke, A. D. Density-Functional Exchange-Energy Approximation with Correct Asymptotic Behavior. *Phys. Rev. A* **1988**, *38* (6), 3098–3100.
(20) Perdew, J. P.; Chevary, J. A.; Vosko, S. H.; Jackson, K. A.; Pederson, M. R.; Singh, D. J.; Fiolhais, C. Atoms, Molecules, Solids, and Surfaces: Applications of the Generalized Gradient Approximation for Exchange and Correlation. *Phys. Rev. B* **1992**, *46* (11), 6671–6687.
(21) Feynman, R. P. Forces in Molecules. *Phys. Rev.* **1939**, *56* (4), 340–343.
(22) Hellmann, H. *Einführung in die Quantenchemie*; J.W. Edwards: Ann Arbor, Mich, 1944.
(23) Saunders, M.; Houk, K. N.; Wu, Y. D.; Still, W. C.; Lipton, M.; Chang, G.; Guida, W. C. Conformations of Cycloheptadecane. A Comparison of Methods for Conformational Searching. *J. Am. Chem. Soc.* **1990**, *112* (4), 1419–1427.
(24) Kolossváry, I.; Keserü, G. M. Hessian-Free Low-Mode Conformational Search for Large-Scale Protein Loop Optimization: Application to c-Jun N-Terminal Kinase JNK3. *J. Comput. Chem.* **2001**, *22* (1), 21–30.
(25) Kolossváry, I.; Guida, W. C. Low-Mode Conformational Search Elucidated: Application to C39H80 and Flexible Docking of 9-Deazaguanine Inhibitors into PNP. *J. Comput. Chem.* **1999**, *20* (15), 1671–1684.
(26) Chiniforoush, S.; Cramer, C. J. Quantum Chemical Characterization of Factors Affecting the Neutral and Radical-Cation Newman–Kwart Reactions. *J. Org. Chem.* **2019**, *84* (4), 2148–2157.
(27) Lee, A. L.; Pandey, A. K.; Chiniforoush, S.; Mandal, M.; Li, J.; Cramer, C. J.; Haynes, C. L.; Pomerantz, W. C. K. Development of a Highly Responsive Organofluorine Temperature Sensor for 19F Magnetic Resonance Applications. *Anal. Chem.* **2022**, *94* (9), 3782–3790.
(28) Luke, A. M.; Peterson, A.; Chiniforoush, S.; Mandal, M.; Popowski, Y.; Sajjad, H.; Bouchey, C. J.; Shopov, D. Y.; Graziano, B. J.; Yao, L. J.; Cramer, C. J.; Reineke, T. M.; Tolman, W. B. Mechanism of Initiation Stereocontrol in Polymerization of Rac-Lactide by Aluminum Complexes Supported by Indolide–Imine Ligands. *Macromolecules* **2020**, *53* (5), 1809–1818.
(29) Lloyd-Jones, G. C.; Moseley, J. D.; Renny, J. S. Mechanism and Application of the Newman-Kwart O→S Rearrangement of O-Aryl Thiocarbamates. *Synthesis* **2008**, *2008* (05), 661–689.
(30) Hori, M.; Iwamura, T.; Imai, E.; Shimizu, H.; Kataoka, T.; Nozaki, M.; Niwa, M.; Fujimura, H. Synthesis and Analgetic Activity of Sulfur-Containing Morphinans and Related Compounds. *Chem. Pharm. Bull. (Tokyo)* **1989**, *37* (5), 1245–1248.
(31) Gallardo-Godoy, A.; Fierro, A.; McLean, T. H.; Castillo, M.; Cassels, B. K.; Reyes-Parada, M.; Nichols, D. E. Sulfur-Substituted α-Alkyl Phenethylamines as

Selective and Reversible MAO-A Inhibitors: Biological Activities, CoMFA Analysis, and Active Site Modeling. *J. Med. Chem.* **2005**, *48* (7), 2407–2419.
(32) Christiansen, L. B.; Wenckens, M.; Bury, P. S.; Gissel, B.; Hansen, B. S.; Thorpe, S. M.; Jacobsen, P.; Kanstrup, A.; Jørgensen, A. S.; Nærum, L.; Wassermann, K. Synthesis and Biological Evaluation of Novel Thio-Substituted Chromanes as High-Affinity Partial Agonists for the Estrogen Receptor. *Bioorg. Med. Chem. Lett.* **2002**, *12* (1), 17–19.
(33) Winum, J.-Y.; Baghdiguian, S.; Commes, T.; Leydet, A.; Montero, J.-L. Synthesis of New Targretin® Analogues That Induce Apoptosis in Leukemia HL-60 Cells. *Bioorg. Med. Chem. Lett.* **2002**, *12* (24), 3529–3532.
(34) Gilman, Henry.; Fullhart, Lawrence. Some Substituted β-Hydroxyethyl Sulfides. *J. Am. Chem. Soc.* **1949**, *71* (4), 1478–1481.
(35) Haas, A.; Lieb, M.; Zhang, Y. Electrophilic Reactions of Trihalogenomethanesulfenyl Acetates and Trifluoroacetates. *J. Fluor. Chem.* **1985**, *29* (3), 297–310.
(36) Shaw, J. E. Preparation of Thiophenols from Unactivated Aryl Chlorides and Sodium Alkanethiolates in N-Methyl-2-Pyrrolidone. *J. Org. Chem.* **1991**, *56* (11), 3728–3729.
(37) Fernández-Rodríguez, M. A.; Shen, Q.; Hartwig, J. F. Highly Efficient and Functional-Group-Tolerant Catalysts for the Palladium-Catalyzed Coupling of Aryl Chlorides with Thiols. *Chem. Weinh. Bergstr. Ger.* **2006**, *12* (30), 7782–7796.
(38) Harvey, J. N.; Jover, J.; Lloyd-Jones, G. C.; Moseley, J. D.; Murray, P.; Renny, J. S. The Newman–Kwart Rearrangement of O-Aryl Thiocarbamates: Substantial Reduction in Reaction Temperatures through Palladium Catalysis. *Angew. Chem.* **2009**, *121* (41), 7748–7751.
(39) Alajarin, M.; Marin-Luna, M.; Ortin, M.-M.; Sanchez-Andrada, P.; Vidal, A. Benzylic Newman–Kwart Rearrangement of O-Azidobenzyl Thiocarbamates Triggered by Phosphines: Pseudopericyclic [1,3] Shifts via Uncoupled Concerted Mechanisms. *Tetrahedron* **2009**, *65* (12), 2579–2590.
(40) Gais, H.-J.; Böhme, A. Palladium(0)-Catalyzed Enantioselective O,S-Rearrangement of Racemic O-Allylic Thiocarbamates: A New Entry to Enantioenriched Allylic Sulfur Compounds. *J. Org. Chem.* **2002**, *67* (4), 1153–1161.
(41) Jacobsen, H.; Donahue, J. P. Expanding the Scope of the Newman–Kwart Rearrangement — A Computational Assessment. *Can. J. Chem.* **2006**, *84* (11), 1567–1574.
(42) Sørensen, A.; Rasmussen, B.; Agarwal, S.; Schau-Magnussen, M.; Sølling, T. I.; Pittelkow, M. Conversion of Phenols into Selenophenols: Seleno Newman–Kwart Rearrangement. *Angew. Chem. Int. Ed.* **2013**, *52* (47), 12346–12349.
(43) Perkowski, A. J.; Cruz, C. L.; Nicewicz, D. A. Ambient-Temperature Newman–Kwart Rearrangement Mediated by Organic Photoredox Catalysis. *J. Am. Chem. Soc.* **2015**, *137* (50), 15684–15687.
(44) Pedersen, S. K.; Ulfkjær, A.; Newman, M. N.; Yogarasa, S.; Petersen, A. U.; Sølling, T. I.; Pittelkow, M. Inverting the Selectivity of the Newman–Kwart

Rearrangement via One Electron Oxidation at Room Temperature. *J. Org. Chem.* **2018**, *83* (19), 12000–12006.
(45) Cismesia, M. A.; Yoon, T. P. Characterizing Chain Processes in Visible Light Photoredox Catalysis. *Chem. Sci.* **2015**, *6* (10), 5426–5434.
(46) Zhao, Y.; Truhlar, D. G. The M06 Suite of Density Functionals for Main Group Thermochemistry, Thermochemical Kinetics, Noncovalent Interactions, Excited States, and Transition Elements: Two New Functionals and Systematic Testing of Four M06-Class Functionals and 12 Other Functionals. *Theor. Chem. Acc.* **2008**, *120* (1), 215–241.
(47) Wiberg, K. B. Ab Initio Molecular Orbital Theory by W. J. Hehre, L. Radom, P. v. R. Schleyer, and J. A. Pople, John Wiley, New York, 548pp. Price: $79.95 (1986). *J. Comput. Chem.* **1986**, *7* (3), 379–379.
(48) Ribeiro, R. F.; Marenich, A. V.; Cramer, C. J.; Truhlar, D. G. Use of Solution-Phase Vibrational Frequencies in Continuum Models for the Free Energy of Solvation. *J. Phys. Chem. B* **2011**, *115* (49), 14556–14562.
(49) Weigend, F. Accurate Coulomb-Fitting Basis Sets for H to Rn. *Phys. Chem. Chem. Phys.* **2006**, *8* (9), 1057–1065.
(50) Weigend, F.; Ahlrichs, R. Balanced Basis Sets of Split Valence, Triple Zeta Valence and Quadruple Zeta Valence Quality for H to Rn: Design and Assessment of Accuracy. *Phys. Chem. Chem. Phys.* **2005**, *7* (18), 3297–3305.
(51) Marenich, A. V.; Cramer, C. J.; Truhlar, D. G. Universal Solvation Model Based on Solute Electron Density and on a Continuum Model of the Solvent Defined by the Bulk Dielectric Constant and Atomic Surface Tensions. *J. Phys. Chem. B* **2009**, *113* (18), 6378–6396.
(52) Marenich, A. V.; Jerome, S. V.; Cramer, C. J.; Truhlar, D. G. Charge Model 5: An Extension of Hirshfeld Population Analysis for the Accurate Description of Molecular Interactions in Gaseous and Condensed Phases. *J. Chem. Theory Comput.* **2012**, *8* (2), 527–541.
(53) Hirshfeld, F. L. Bonded-Atom Fragments for Describing Molecular Charge Densities. *Theor. Chim. Acta* **1977**, *44* (2), 129–138.
(54) Zhao, Y.; Truhlar, D. G. Density Functionals with Broad Applicability in Chemistry. *Acc. Chem. Res.* **2008**, *41* (2), 157–167.
(55) Korth, M.; Grimme, S. "Mindless" DFT Benchmarking. *J. Chem. Theory Comput.* **2009**, *5* (4), 993–1003.
(56) Zhao, Y.; Truhlar, D. G. Density Functional Theory for Reaction Energies: Test of Meta and Hybrid Meta Functionals, Range-Separated Functionals, and Other High-Performance Functionals. *J. Chem. Theory Comput.* **2011**, *7* (3), 669–676.
(57) Mardirossian, N.; Head-Gordon, M. How Accurate Are the Minnesota Density Functionals for Noncovalent Interactions, Isomerization Energies, Thermochemistry, and Barrier Heights Involving Molecules Composed of Main-Group Elements? *J. Chem. Theory Comput.* **2016**, *12* (9), 4303–4325.
(58) Neese, F. The ORCA Program System. *WIREs Comput. Mol. Sci.* **2012**, *2* (1), 73–78.

(59) Sparta, M.; Neese, F. Chemical Applications Carried out by Local Pair Natural Orbital Based Coupled-Cluster Methods. *Chem. Soc. Rev.* **2014**, *43* (14), 5032–5041.
(60) Frisch, M. J.; Trucks, G. W.; Schlegel, H. B.; Scuseria, G. E.; Robb, M. A.; Cheeseman, J. R.; Scalmani, G.; Barone, V.; Petersson, G. A.; Nakatsuji, H.; Li, X.; Caricato, M.; Marenich, A. V.; Bloino, J.; Janesko, B. G.; Gomperts, R.; Mennucci, B.; Hratchian, H. P.; Ortiz, J. V.; Izmaylov, A. F.; Sonnenberg, J. L.; Williams; Ding, F.; Lipparini, F.; Egidi, F.; Goings, J.; Peng, B.; Petrone, A.; Henderson, T.; Ranasinghe, D.; Zakrzewski, V. G.; Gao, J.; Rega, N.; Zheng, G.; Liang, W.; Hada, M.; Ehara, M.; Toyota, K.; Fukuda, R.; Hasegawa, J.; Ishida, M.; Nakajima, T.; Honda, Y.; Kitao, O.; Nakai, H.; Vreven, T.; Throssell, K.; Montgomery Jr., J. A.; Peralta, J. E.; Ogliaro, F.; Bearpark, M. J.; Heyd, J. J.; Brothers, E. N.; Kudin, K. N.; Staroverov, V. N.; Keith, T. A.; Kobayashi, R.; Normand, J.; Raghavachari, K.; Rendell, A. P.; Burant, J. C.; Iyengar, S. S.; Tomasi, J.; Cossi, M.; Millam, J. M.; Klene, M.; Adamo, C.; Cammi, R.; Ochterski, J. W.; Martin, R. L.; Morokuma, K.; Farkas, O.; Foresman, J. B.; Fox, D. J. Gaussian 09 Rev. A.02, 2016.
(61) Prabhakar, S.; Kar, P.; Mirza, S. P.; Lakshmi, V. V. S.; Nagaiah, K.; Vairamani, M. Mass Spectral Study of O- and S-Aryl Dimethylthiocarbamates under Electron Impact Conditions: Newman-Kwart Rearrangement in the Gas Phase. *Rapid Commun. Mass Spectrom.* **2001**, *15* (22), 2127–2134.
(62) Chiniforoush, S.; Cramer, C. J. Quantum Chemical Characterization of Factors Affecting the Neutral and Radical-Cation Newman-Kwart Reactions. ChemRxiv December 17, 2018.
(63) Ring, E. F. J.; Mcevoy, H.; Jung, A.; Zuber, J.; Machin, G. New Standards for Devices Used for the Measurement of Human Body Temperature. *J. Med. Eng. Technol.* **2010**, *34* (4), 249–253.
(64) Kalamida, D.; Karagounis, I. V.; Mitrakas, A.; Kalamida, S.; Giatromanolaki, A.; Koukourakis, M. I. Fever-Range Hyperthermia vs. Hypothermia Effect on Cancer Cell Viability, Proliferation and HSP90 Expression. *PLOS ONE* **2015**, *10* (1), e0116021.
(65) Richards, S. A. *Temperature Regulation*; Springer US: Boston, MA, 1973.
(66) Sund-Levander, M.; Forsberg, C.; Wahren, L. K. Normal Oral, Rectal, Tympanic and Axillary Body Temperature in Adult Men and Women: A Systematic Literature Review. *Scand. J. Caring Sci.* **2002**, *16* (2), 122–128.
(67) *Bacterial Pathogenesis*; DeLeo, F. R., Otto, M., Eds.; Humana Press: Totowa, NJ, 2008.
(68) Diepart, C.; Verrax, J.; Calderon, P. B.; Feron, O.; Jordan, B. F.; Gallez, B. Comparison of Methods for Measuring Oxygen Consumption in Tumor Cells in Vitro. *Anal. Biochem.* **2010**, *396* (2), 250–256.
(69) Karaszewski, B.; Carpenter, T. K.; Thomas, R. G.; Armitage, P. A.; Lymer, G. K. S.; Marshall, I.; Dennis, M. S.; Wardlaw, J. M. Relationships Between Brain and Body Temperature, Clinical and Imaging Outcomes after Ischemic Stroke. *J. Cereb. Blood Flow Metab.* **2013**, *33* (7), 1083–1089.

(70) Wang, P. Evaluation of MR Thermometry with Proton Resonance Frequency Method at 7T. *Quant. Imaging Med. Surg.* **2017**, *7* (2), 25966–25266.
(71) Quesson, B.; de Zwart, J. A.; Moonen, C. T. W. Magnetic Resonance Temperature Imaging for Guidance of Thermotherapy. *J. Magn. Reson. Imaging* **2000**, *12* (4), 525–533.
(72) Rieke, V.; Butts Pauly, K. MR Thermometry. *J. Magn. Reson. Imaging* **2008**, *27* (2), 376–390.
(73) Winter, L.; Oberacker, E.; Paul, K.; Ji, Y.; Oezerdem, C.; Ghadjar, P.; Thieme, A.; Budach, V.; Wust, P.; Niendorf, T. Magnetic Resonance Thermometry: Methodology, Pitfalls and Practical Solutions. *Int. J. Hyperthermia* **2016**, *32* (1), 63–75.
(74) Jeon, I.-R.; Park, J. G.; Haney, C. R.; Harris, T. D. Spin Crossover Iron(II) Complexes as PARACEST MRI Thermometers. *Chem. Sci.* **2014**, *5* (6), 2461–2465.
(75) Prinz, C.; Delgado, P. R.; Eigentler, T. W.; Starke, L.; Niendorf, T.; Waiczies, S. Toward 19F Magnetic Resonance Thermometry: Spin–Lattice and Spin–Spin-Relaxation Times and Temperature Dependence of Fluorinated Drugs at 9.4 T. *Magn. Reson. Mater. Phys. Biol. Med.* **2019**, *32* (1), 51–61.
(76) Van Geet, A. L. Calibration of Methanol Nuclear Magnetic Resonance Thermometer at Low Temperature. *Anal. Chem.* **1970**, *42* (6), 679–680.
(77) Van Geet, A. L. Calibration of the Methanol and Glycol Nuclear Magnetic Resonance Thermometers with a Static Thermistor Probe. *Anal. Chem.* **1968**, *40* (14), 2227–2229.
(78) Raiford, D. S.; Fisk, C. L.; Becker, E. D. Calibration of Methanol and Ethylene Glycol Nuclear Magnetic Resonance Thermometers. *Anal. Chem.* **1979**, *51* (12), 2050–2051.
(79) Poorter, J. D.; Wagter, C. D.; Deene, Y. D.; Thomsen, C.; Ståhlberg, F.; Achten, E. Noninvasive MRI Thermometry with the Proton Resonance Frequency (PRF) Method: In Vivo Results in Human Muscle. *Magn. Reson. Med.* **1995**, *33* (1), 74–81.
(80) Gorny, K. R.; Favazza, C. P.; Lu, A.; Felmlee, J. P.; Hangiandreou, N. J.; Browne, J. E.; Stenzel, W. S.; Muggli, J. L.; Anderson, A. G.; Thompson, S. M.; Woodrum, D. A. Practical Implementation of Robust MR-Thermometry during Clinical MR-Guided Microwave Ablations in the Liver at 1.5 T. *Phys. Med.* **2019**, *67*, 91–99.
(81) Yuan, J.; Mei, C.-S.; Panych, L. P.; McDannold, N. J.; Madore, B. Towards Fast and Accurate Temperature Mapping with Proton Resonance Frequency-Based MR Thermometry. *Quant. Imaging Med. Surg.* **2012**, *2* (1), 212–232.
(82) Harder, E.; Damm, W.; Maple, J.; Wu, C.; Reboul, M.; Xiang, J. Y.; Wang, L.; Lupyan, D.; Dahlgren, M. K.; Knight, J. L.; Kaus, J. W.; Cerutti, D. S.; Krilov, G.; Jorgensen, W. L.; Abel, R.; Friesner, R. A. OPLS3: A Force Field Providing Broad Coverage of Drug-like Small Molecules and Proteins. *J. Chem. Theory Comput.* **2016**, *12* (1), 281–296.
(83) Zhao, Y.; Truhlar, D. G. A New Local Density Functional for Main-Group Thermochemistry, Transition Metal Bonding, Thermochemical Kinetics, and Noncovalent Interactions. *J. Chem. Phys.* **2006**, *125* (19), 194101.

(84) Becke, A. D. Density-functional Thermochemistry. III. The Role of Exact Exchange. *J. Chem. Phys.* **1993**, *98* (7), 5648–5652.
(85) Wolinski, K.; Hinton, J. F.; Pulay, P. Efficient Implementation of the Gauge-Independent Atomic Orbital Method for NMR Chemical Shift Calculations. *J. Am. Chem. Soc.* **1990**, *112* (23), 8251–8260.
(86) Frisch, M. J.; Trucks, G. W.; Schlegel, H. B.; Scuseria, G. E.; Robb, M. A.; Cheeseman, J. R.; Scalmani, G.; Barone, V.; Petersson, G. A.; Nakatsuji, H.; Li, X.; Caricato, M.; Marenich, A. V.; Bloino, J.; Janesko, B. G.; Gomperts, R.; Mennucci, B.; Hratchian, H. P.; Ortiz, J. V.; Izmaylov, A. F.; Sonnenberg, J. L.; Williams; Ding, F.; Lipparini, F.; Egidi, F.; Goings, J.; Peng, B.; Petrone, A.; Henderson, T.; Ranasinghe, D.; Zakrzewski, V. G.; Gao, J.; Rega, N.; Zheng, G.; Liang, W.; Hada, M.; Ehara, M.; Toyota, K.; Fukuda, R.; Hasegawa, J.; Ishida, M.; Nakajima, T.; Honda, Y.; Kitao, O.; Nakai, H.; Vreven, T.; Throssell, K.; Montgomery Jr., J. A.; Peralta, J. E.; Ogliaro, F.; Bearpark, M. J.; Heyd, J. J.; Brothers, E. N.; Kudin, K. N.; Staroverov, V. N.; Keith, T. A.; Kobayashi, R.; Normand, J.; Raghavachari, K.; Rendell, A. P.; Burant, J. C.; Iyengar, S. S.; Tomasi, J.; Cossi, M.; Millam, J. M.; Klene, M.; Adamo, C.; Cammi, R.; Ochterski, J. W.; Martin, R. L.; Morokuma, K.; Farkas, O.; Foresman, J. B.; Fox, D. J. Gaussian 16 Rev. C.01, 2016.
(87) Release, S. 4: LigPrep. *Schrödinger LLC N. Y. NY* **2019**.
(88) Lee, A. L.; Gee, C. T.; Weegman, B. P.; Einstein, S. A.; Juelfs, A. R.; Ring, H. L.; Hurley, K. R.; Egger, S. M.; Swindlehurst, G.; Garwood, M.; Pomerantz, W. C. K.; Haynes, C. L. Oxygen Sensing with Perfluorocarbon-Loaded Ultraporous Mesostructured Silica Nanoparticles. *ACS Nano* **2017**, *11* (6), 5623–5632.
(89) Berkowitz, B. A.; Handa, J. T.; Wilson, C. A. Perfluorocarbon Temperature Measurements Using 19F NMR. *NMR Biomed.* **1992**, *5* (2), 65–68.
(90) Hong, A. C.; Young, C. J.; Hurley, M. D.; Wallington, T. J.; Mabury, S. A. Perfluorotributylamine: A Novel Long-Lived Greenhouse Gas. *Geophys. Res. Lett.* **2013**, *40* (22), 6010–6015.
(91) Bläsing, K.; Labbow, R.; Michalik, D.; Reiß, F.; Schulz, A.; Villinger, A.; Walker, S. On Silylated Oxonium and Sulfonium Ions and Their Interaction with Weakly Coordinating Borate Anions. *Chem. – Eur. J.* **2020**, *26* (7), 1640–1652.
(92) Alkorta, I.; Elguero, J. Dissociation Energies and Rotational Barriers About CC Single, Double, and Triple Bonds: A Hybrid HF-DFT Approach (Becke3LYP/6-311++G**). *Struct. Chem.* **1998**, *9* (1), 59–63.
(93) Langner, C.; Meier-Haack, J.; Voit, B.; Komber, H. The Stepped Reaction of Decafluorobiphenyl with Thiophenol Studied by in Situ 19F NMR Spectroscopy. *J. Fluor. Chem.* **2013**, *156*, 314–321.
(94) Maus, M.; Rettig, W. The Excited State Equilibrium between Two Rotational Conformers of a Sterically Restricted Donor−Acceptor Biphenyl As Characterized by Global Fluorescence Decay Analysis. *J. Phys. Chem. A* **2002**, *106* (10), 2104–2111.
(95) Landeros-Rivera, B.; Jancik, V.; Moreno-Esparza, R.; Martínez Otero, D.; Hernández-Trujillo, J. Non-Covalent Interactions in the Biphenyl Crystal: Is the Planar Conformer a Transition State? *Chem. – Eur. J.* **2021**, *27* (46), 11912–11918.

(96) Zandarashvili, L.; Esadze, A.; Iwahara, J. Chapter Two - NMR Studies on the Dynamics of Hydrogen Bonds and Ion Pairs Involving Lysine Side Chains of Proteins. In *Advances in Protein Chemistry and Structural Biology*; Christov, C. Z., Ed.; Biomolecular Spectroscopy: Advances from Integrating Experiments and Theory; Academic Press, 2013; Vol. 93, pp 37–80.
(97) Perrin, C. L. Physical Organic Chemistry. In *Encyclopedia of Physical Science and Technology (Third Edition)*; Meyers, R. A., Ed.; Academic Press: New York, 2003; pp 211–243.
(98) Kamarudin, N. H. N.; Jalil, A. A.; Triwahyono, S.; Artika, V.; Salleh, N. F. M.; Karim, A. H.; Jaafar, N. F.; Sazegar, M. R.; Mukti, R. R.; Hameed, B. H.; Johari, A. Variation of the Crystal Growth of Mesoporous Silica Nanoparticles and the Evaluation to Ibuprofen Loading and Release. *J. Colloid Interface Sci.* **2014**, *421*, 6–13.
(99) Ruffel, L.; Soulié, J.; Coppel, Y.; Roblin, P.; Brouillet, F.; Frances, C.; Tourbin, M. Ibuprofen Loading into Mesoporous Silica Nanoparticles Using Co-Spray Drying: A Multi-Scale Study. *Microporous Mesoporous Mater.* **2020**, *291*, 109689.
(100) Lim, E.-B.; Vy, T. A.; Lee, S.-W. Comparative Release Kinetics of Small Drugs (Ibuprofen and Acetaminophen) from Multifunctional Mesoporous Silica Nanoparticles. *J. Mater. Chem. B* **2020**, *8* (10), 2096–2106.
(101) Schneiderman, D. K.; Hillmyer, M. A. 50th Anniversary Perspective: There Is a Great Future in Sustainable Polymers. *Macromolecules* **2017**, *50* (10), 3733–3749.
(102) Wu, J.; Yu, T.-L.; Chen, C.-T.; Lin, C.-C. Recent Developments in Main Group Metal Complexes Catalyzed/Initiated Polymerization of Lactides and Related Cyclic Esters. *Coord. Chem. Rev.* **2006**, *250* (5), 602–626.
(103) Coates, G. W.; Moore, D. R. Discrete Metal-Based Catalysts for the Copolymerization of CO2 and Epoxides: Discovery, Reactivity, Optimization, and Mechanism. *Angew. Chem. Int. Ed.* **2004**, *43* (48), 6618–6639.
(104) Dechy-Cabaret, O.; Martin-Vaca, B.; Bourissou, D. Controlled Ring-Opening Polymerization of Lactide and Glycolide. *Chem. Rev.* **2004**, *104* (12), 6147–6176.
(105) Stanford, M. J.; Dove, A. P. Stereocontrolled Ring-Opening Polymerisation of Lactide. *Chem. Soc. Rev.* **2010**, *39* (2), 486–494.
(106) Drumright, R. E.; Gruber, P. R.; Henton, D. E. Polylactic Acid Technology. *Adv. Mater.* **2000**, *12* (23), 1841–1846.
(107) Tsuji, H. Poly(Lactide) Stereocomplexes: Formation, Structure, Properties, Degradation, and Applications. *Macromol. Biosci.* **2005**, *5* (7), 569–597.
(108) Le Borgne, A.; Vincens, V.; Jouglard, M.; Spassky, N. Ring-Opening Oligomerization Reactions Using Aluminium Complexes of Schiff's Bases as Initiators. *Makromol. Chem. Macromol. Symp.* **1993**, *73* (1), 37–46.
(109) Spassky, N.; Wisniewski, M.; Pluta, C.; Le Borgne, A. Highly Stereoelective Polymerization of Rac-(D,L)-Lactide with a Chiral Schiff's Base/Aluminium Alkoxide Initiator. *Macromol. Chem. Phys.* **1996**, *197* (9), 2627–2637.
(110) Wisniewski, M.; Borgne, A. L.; Spassky, N. Synthesis and Properties of (D)- and (L)-Lactide Stereocopolymers Using the System Achiral Schiff's Base/Aluminium Methoxide as Initiator. *Macromol. Chem. Phys.* **1997**, *198* (4), 1227–1238.

(111) Radano, C. P.; Baker, G. L.; Smith, M. R. Stereoselective Polymerization of a Racemic Monomer with a Racemic Catalyst: Direct Preparation of the Polylactic Acid Stereocomplex from Racemic Lactide. *J. Am. Chem. Soc.* **2000**, *122* (7), 1552–1553.
(112) Ovitt, T. M.; Coates, G. W. Stereoselective Ring-Opening Polymerization of Rac-Lactide with a Single-Site, Racemic Aluminum Alkoxide Catalyst: Synthesis of Stereoblock Poly(Lactic Acid). *J. Polym. Sci. Part Polym. Chem.* **2000**, *38* (S1), 4686–4692.
(113) Majerska, K.; Duda, A. Stereocontrolled Polymerization of Racemic Lactide with Chiral Initiator: Combining Stereoelection and Chiral Ligand-Exchange Mechanism. *J. Am. Chem. Soc.* **2004**, *126* (4), 1026–1027.
(114) Chisholm, M. H.; Patmore, N. J.; Zhou, Z. Concerning the Relative Importance of Enantiomorphic Site vs. Chain End Control in the Stereoselective Polymerization of Lactides: Reactions of (R,R-Salen)- and (S,S-Salen)–Aluminium Alkoxides LAlOCH2R Complexes (R = CH3 and S-CHMeCl). *Chem. Commun.* **2005**, No. 1, 127–129.
(115) Zhong, Z.; Dijkstra, P. J.; Feijen, J. [(Salen)Al]-Mediated, Controlled and Stereoselective Ring-Opening Polymerization of Lactide in Solution and without Solvent: Synthesis of Highly Isotactic Polylactide Stereocopolymers from Racemic d,l-Lactide. *Angew. Chem. Int. Ed.* **2002**, *41* (23), 4510–4513.
(116) Zhong, Z.; Dijkstra, P. J.; Feijen, J. Controlled and Stereoselective Polymerization of Lactide: Kinetics, Selectivity, and Microstructures. *J. Am. Chem. Soc.* **2003**, *125* (37), 11291–11298.
(117) Chisholm, M. H.; Gallucci, J. C.; Quisenberry, K. T.; Zhou, Z. Complexities in the Ring-Opening Polymerization of Lactide by Chiral Salen Aluminum Initiators. *Inorg. Chem.* **2008**, *47* (7), 2613–2624.
(118) Nomura, N.; Ishii, R.; Akakura, M.; Aoi, K. Stereoselective Ring-Opening Polymerization of Racemic Lactide Using Aluminum-Achiral Ligand Complexes: Exploration of a Chain-End Control Mechanism. *J. Am. Chem. Soc.* **2002**, *124* (21), 5938–5939.
(119) Hormnirun, P.; Marshall, E. L.; Gibson, V. C.; White, A. J. P.; Williams, D. J. Remarkable Stereocontrol in the Polymerization of Racemic Lactide Using Aluminum Initiators Supported by Tetradentate Aminophenoxide Ligands. *J. Am. Chem. Soc.* **2004**, *126* (9), 2688–2689.
(120) Nomura, N.; Ishii, R.; Yamamoto, Y.; Kondo, T. Stereoselective Ring-Opening Polymerization of a Racemic Lactide by Using Achiral Salen– and Homosalen–Aluminum Complexes. *Chem. – Eur. J.* **2007**, *13* (16), 4433–4451.
(121) Hormnirun, P.; Marshall, E. L.; Gibson, V. C.; Pugh, R. I.; White, A. J. P. Study of Ligand Substituent Effects on the Rate and Stereoselectivity of Lactide Polymerization Using Aluminum Salen-Type Initiators. *Proc. Natl. Acad. Sci.* **2006**, *103* (42), 15343–15348.
(122) Tang, Z.; Chen, X.; Pang, X.; Yang, Y.; Zhang, X.; Jing, X. Stereoselective Polymerization of Rac-Lactide Using a Monoethylaluminum Schiff Base Complex. *Biomacromolecules* **2004**, *5* (3), 965–970.

(123) Alaaeddine, A.; Thomas, C. M.; Roisnel, T.; Carpentier, J.-F. Aluminum and Yttrium Complexes of an Unsymmetrical Mixed Fluorous Alkoxy/Phenoxy-Diimino Ligand: Synthesis, Structure, and Ring-Opening Polymerization Catalysis. *Organometallics* **2009**, *28* (5), 1469–1475.
(124) Mandal, M.; Luke, A. M.; Dereli, B.; Elwell, C. E.; Reineke, T. M.; Tolman, W. B.; Cramer, C. J. Computational Prediction and Experimental Verification of ε-Caprolactone Ring-Opening Polymerization Activity by an Aluminum Complex of an Indolide/Schiff-Base Ligand. *ACS Catal.* **2019**, *9* (2), 885–889.
(125) Du, H.; Velders, A. H.; Dijkstra, P. J.; Zhong, Z.; Chen, X.; Feijen, J. Polymerization of Lactide Using Achiral Bis(Pyrrolidene) Schiff Base Aluminum Complexes. *Macromolecules* **2009**, *42* (4), 1058–1066.
(126) Wei, Y.; Song, L.; Jiang, L.; Huang, Z.; Wang, S.; Yuan, Q.; Mu, X.; Zhu, X.; Zhou, S. Aluminum Complexes with Schiff Base Bridged Bis(Indolyl) Ligands: Synthesis, Structure, and Catalytic Activity for Polymerization of Rac-Lactide. *Dalton Trans.* **2019**, *48* (40), 15290–15299.
(127) Addison, A. W.; Rao, T. N.; Reedijk, J.; Rijn, J. van; Verschoor, G. C. Synthesis, Structure, and Spectroscopic Properties of Copper(II) Compounds Containing Nitrogen–Sulphur Donor Ligands; the Crystal and Molecular Structure of Aqua[1,7-Bis(N-Methylbenzimidazol-2′-Yl)-2,6-Dithiaheptane]Copper(II) Perchlorate. *J. Chem. Soc. Dalton Trans.* **1984**, No. 7, 1349–1356.
(128) Tian, J.; Hustad, P. D.; Coates, G. W. A New Catalyst for Highly Syndiospecific Living Olefin Polymerization: Homopolymers and Block Copolymers from Ethylene and Propylene. *J. Am. Chem. Soc.* **2001**, *123* (21), 5134–5135.
(129) Milano, G.; Cavallo, L.; Guerra, G. Site Chirality as a Messenger in Chain-End Stereocontrolled Propene Polymerization. *J. Am. Chem. Soc.* **2002**, *124* (45), 13368–13369.
(130) Dagorne, S.; Le Bideau, F.; Welter, R.; Bellemin-Laponnaz, S.; Maisse-François, A. Well-Defined Cationic Alkyl– and Alkoxide–Aluminum Complexes and Their Reactivity with ε-Caprolactone and Lactides. *Chem. – Eur. J.* **2007**, *13* (11), 3202–3217.
(131) Lewiński, J.; Horeglad, P.; Wójcik, K.; Justyniak, I. Chelation Effect in Polymerization of Cyclic Esters by Metal Alkoxides: Structure Characterization of the Intermediate Formed by Primary Insertion of Lactide into the Al−OR Bond of an Organometallic Initiator. *Organometallics* **2005**, *24* (19), 4588–4593.
(132) Trofimoff, L.; Aida, T.; Inoue, S. Formation of Poly(Lactide) with Controlled Molecular Weight. Polymerization of Lactide by Aluminum Porphyrin. *Chem. Lett.* **1987**, *16* (5), 991–994.
(133) Chamberlain, B. M.; Cheng, M.; Moore, D. R.; Ovitt, T. M.; Lobkovsky, E. B.; Coates, G. W. Polymerization of Lactide with Zinc and Magnesium β-Diiminate Complexes: Stereocontrol and Mechanism. *J. Am. Chem. Soc.* **2001**, *123* (14), 3229–3238.
(134) Jones, G. O. Contributions of Quantum Chemistry to the Development of Ring Opening Polymerizations and Chemical Recycling. *Tetrahedron* **2019**, *75* (14), 2047–2055.

(135) Chapter 8 - Two-Dimensional Spectra and Beyond. In *Current Methods in Inorganic Chemistry*; Bertini, I., Luchinat, C., Parigi, G., Eds.; Solution NMR of Paramagnetic Molecules; Elsevier, 2001; Vol. 2, pp 263–302.
(136) Lu, J.; Ma, D.; Hu, J.; Tang, W.; Zhu, D. Nuclear Magnetic Resonance Spectroscopic Studies of Pyridine Methyl Derivatives Binding to Cytochrome c. *J. Chem. Soc. Dalton Trans.* **1998**, No. 13, 2267–2274.
(137) Grimme, S.; Antony, J.; Ehrlich, S.; Krieg, H. A Consistent and Accurate Ab Initio Parametrization of Density Functional Dispersion Correction (DFT-D) for the 94 Elements H-Pu. *J. Chem. Phys.* **2010**, *132* (15), 154104.
(138) Stephens, P. J.; Devlin, F. J.; Chabalowski, C. F.; Frisch, M. J. Ab Initio Calculation of Vibrational Absorption and Circular Dichroism Spectra Using Density Functional Force Fields. *J. Phys. Chem.* **1994**, *98* (45), 11623–11627.
(139) Adamo, C.; Barone, V. Toward Reliable Density Functional Methods without Adjustable Parameters: The PBE0 Model. *J. Chem. Phys.* **1999**, *110* (13), 6158–6170.
(140) Chai, J.-D.; Head-Gordon, M. Long-Range Corrected Hybrid Density Functionals with Damped Atom–Atom Dispersion Corrections. *Phys. Chem. Chem. Phys.* **2008**, *10* (44), 6615–6620.
(141) Marshall, E. L.; Gibson, V. C.; Rzepa, H. S. A Computational Analysis of the Ring-Opening Polymerization of Rac-Lactide Initiated by Single-Site β-Diketiminate Metal Complexes: Defining the Mechanistic Pathway and the Origin of Stereocontrol. *J. Am. Chem. Soc.* **2005**, *127* (16), 6048–6051.
(142) Fang, J.; Yu, I.; Mehrkhodavandi, P.; Maron, L. Theoretical Investigation of Lactide Ring-Opening Polymerization Induced by a Dinuclear Indium Catalyst. *Organometallics* **2013**, *32* (23), 6950–6956.
(143) Xu, T.-Q.; Yang, G.-W.; Liu, C.; Lu, X.-B. Highly Robust Yttrium Bis(Phenolate) Ether Catalysts for Excellent Isoselective Ring-Opening Polymerization of Racemic Lactide. *Macromolecules* **2017**, *50* (2), 515–522.
(144) Stasiw, D. E.; Luke, A. M.; Rosen, T.; League, A. B.; Mandal, M.; Neisen, B. D.; Cramer, C. J.; Kol, M.; Tolman, W. B. Mechanism of the Polymerization of Rac-Lactide by Fast Zinc Alkoxide Catalysts. *Inorg. Chem.* **2017**, *56* (22), 14366–14372.
(145) Ligny, R.; Hänninen, M. M.; Guillaume, S. M.; Carpentier, J.-F. Steric vs. Electronic Stereocontrol in Syndio- or Iso-Selective ROP of Functional Chiral β-Lactones Mediated by Achiral Yttrium-Bisphenolate Complexes. *Chem. Commun.* **2018**, *54* (58), 8024–8031.